Electronic Supplementary Material (ESI) for Sustainable Energy & Fuels.

Supporting information to:

P-containing coated carbons from phosphonium ionic liquids as catalyst support for fuel cell application

Angelo A. Severin[a*], Daniel Rauber[a,b], Frederik Philippi[a,c], Ivan Radev[d], Manfred Baumgärtner[e], Anne Holtsch[f], Frank Müller[f], Stavroula Pachoula[a], Rolf Hempelmann[b], Christopher W. M. Kay[a,g]

* Corresponding author. *Tel.:* +49 681 302 64310; *E-mail address:* angelo.stephan@uni-saarland.de

a. Department of Chemistry, Saarland University, Campus B2 2, 66123 Saarbrücken, Germany.
b. Transfer-center Sustainable Electrochemistry, Saarland University, Am Markt, Zeile 3, 66125 Saarbrücken, Germany.
c. current Address: Department of Chemistry, Molecular Sciences Research Hub, Imperial College London, White City Campus, London W12 0BZ, United Kingdom.
d. The Hydrogen and Fuel Cell Center ZBT GmbH, Carl-Benz-Straße 201, 47057 Duisburg, Germany.
e. Research Institute for Precious Metals and Metal Chemistry, Katharinenstraße 17, 73525 Schwäbisch Gmünd, Germany.
f. Experimental Physics and Center for Biophysics, Saarland University, Campus E2 9, 66123 Saarbrücken, Germany.
g. London Centre for Nanotechnology, University College London, 17-19 Gordon Street, London WC1H 0AH, UK.

Table of Content

1. Additional background

There are various approaches to synthesize PCCs and three major synthesis ways are already established.[1] The first method starts from a carbon-containing precursor with two possibilities of introducing phosphorus into the final product. One way is physical mixing of the carbon starting material with a suitable phosphorus source followed by pyrolysis, including soft and hard template methods. Phosphoric acid H_3PO_4[2,3] is commonly used but other P-containing chemicals, for instance various acids[4], salts[5], triphenylphosphine[6] or ionic liquids[7] have also been reported. The advantage of this method is a cost-efficient, straightforward way of synthesizing creating P-containing carbons. The major disadvantages are that the phosphorus group formation and resulting morphology are exceedingly difficult to control in direct pyrolysis of the substance compared to using a template method. Another way to synthesize PCCs by introducing P into the carbon is chemical binding of phosphorus into the carbon-containing source, for example by means of poly-condensation[8] reactions or phosphorylation[9,10] with different P-containing chemicals. The advantage of this approach is the control over the reaction with the disadvantage of including complex steps. The second method describes the co-deposition of carbon and phosphorus, *i.e.* from the gas phase, by different approaches.[11,12] These approaches allow specific control over the synthesized P-containing carbon, such as morphology, species formation and resulting P-content. The disadvantage are the excessive costs, the requirement of advanced technologies and the knowledge of the process conditions. The third method to synthesize P-containing carbons is by modification of prefabricated carbons with a suitable phosphorus compound (for instance various phosphorus acids[13] or ionic liquids[14]) by carbonization at elevated temperatures. This method is cost efficient and straightforward while the amount of doping can also be controlled by the choice of the P-source. Coating of the surfaces allows the precise deposition of phosphorus species where it is supposed to be: at the surface and phase boundaries where the reactions take place. The ultimate advantage of this approach is the adaptation of every morphology and beneficial characteristics of prefabricated carbon materials without any of their original properties. A disadvantage is that the types of phosphorus groups created are correlated to the P-source and may thereby be limited. The coating procedure by means of wet impregnation with ionic liquids used here belongs to the third type of approach and is explained below in a more detailed way.

Incorporation of PCCs has already been successful for other electrochemical devices, such as supercapacitors. A simple H_3PO_4 activation of micro porous carbon resulted in extraordinary

performance in electric double layer activity.[15–17] The P-containing micro porous carbon showed an electrical capacitance of 190–220 F g^{-1}, compared to 140 F g^{-1} for the commercial product Norti RB3. This effect was attributed mainly to the P-content and pseudo-capacity due to fast faradic reactions created by phosphorus groups. Additionally, the P-containing materials showed stable performance during 15,000 cycles under voltage of 1.5 V without electrolyte decomposition due to blockage of reaction sites by phosphorus. PCC can also be used in lithium-ion-batteries. Studies have shown that phosphorus enhances the reversible capacity of carbon materials in the batteries by increasing the number of active sites for the intercalation of Li-ions.[18] The authors assumed that phosphorus species might produce bridging structures between crystallites at the edge-plane of graphene layers, increasing the capacity towards Li-ions. The theory of phosphorus promoting Li-intercalation through expanding the expansion of the layer plane at the edge of the carbon structure is also promoted by Tran and co-workers.[19] P-containing hierarchical porous carbon (HPC) provided an efficient electron conductive network, where the results indicated that phosphorus improves the chemical bonding between metal oxides and carbon.[20]

Oxygen reduction reactions (ORR) are crucial in fuel cells and fields of application where PCC can be utilized. P-containing carbon nanotubes were shown to improve the electro-catalytical activity in alkaline medium.[11] The PC-CNT material exhibited a higher electro-catalytical activity and stability than commercial Pt/C catalysts, attributed to both the phosphorus content (0–0.13 at.-%) and the morphology of the carbon material. The current density output of P-containing carbon nanotubes showed no change in long-term operation, while commercial Pt/C catalysts demonstrated a decrease after 10,000 cycles. This suggests superior performance and stability of P-CNT compared to Pt/C catalysts. Further research[21,22] supports the results where PCC exhibited high electro-catalytical activity and stability after 12,000-13,000 cycles with excellent tolerance to cross-over effects of methanol in methanol fuel cells. This increase in ORR activity was attributed to the electron donor properties of phosphorus and the strong electron affinity of P-containing graphite due to the dissociation of acidic P-containing groups.[9] Authors propose that these properties can enhance the adsorption of O_2 at the surface resulting in an overall increase of ORR. ORR occurs in proton exchange membrane fuel cells (PEMFC) at the cathode. PCC are thus suitable catalyst supports for fuel cell application due to the improved electronic properties and stability.

Fuel cells are a promising technology to address pressing questions for a more sustainable energy supply and a slowdown of anthropogenic climate change. There is an increasing demand for sophisticated energy conversion devices for electro-mobility to replace fossil energy sources. Diverse types of fuel cells can be utilized to power CO_2-emission-free cars for the transportation of heavy loads or as non-central energy storage in buildings. With the envisioned H_2-infrastructure and usage of renewable energy sources, fuel cells may contribute to solutions of the many problems our society is currently facing. The major obstacles in terms of long-term durability of PEMFCs are carbon corrosion due to the carbon thermodynamic instability at electrode potentials above 207 mV vs. SHE, hydrogen peroxide evolution and degradation of noble metal catalysts over time due to Ostwald ripening, and agglomeration.[23–

[28] Phosphorus groups and functionalities in carbon supports may serve as barriers that inhibit the diffusion and interaction of noble metal catalyst particles and therefore preventing particle agglomeration and fuel cell aging. Since carbon materials are already used as catalyst supports in low temperature fuel cells, such as the PEMFCs, the utilization of phosphorus-doped carbon materials allows the usage of alternative catalyst supports with improved properties to overcome these obstacles in order to increase the longevity and the performance of fuel cells.

Ionic liquids (IL) are a class of versatile liquid materials with a wide range of applications in electrochemical energy storage and conversion. This includes the application as simple solvent/electrolyte as well as diverse additional uses in the preparation and operation of electrochemical devices.[29–31] In most cases, detailed knowledge of physicochemical characteristics of ionic liquids is of high importance. Pyrolysis of ionic liquids adsorbed on the surface of carbon materials serves as a novel synthetic approach for innovative carbon materials with coatings of heteroatom containing carbons. Previous work confirmed that ionic liquids with their non-polar character can be adsorbed on activated carbon surfaces.[32,33] In general,[34] ionic liquids exhibit a number of properties that make them ideal for homogeneous coating followed by pyrolysis. Due to their low melting points, they remain in liquid state during the coating process at ambient conditions, forming a homogeneous liquid layer on the substrate – in contrary to substances that crystallize from solvents. The uniform distribution on the carbon surface is supported further by the ILs' higher viscosities compared to conventional molecular liquids. This can be due to the less polar character of ionic liquids compared to water that allows better interactions with carbon surfaces resulting in a good wettability of carbon materials by ionic liquids. The most important characteristics of ionic liquids for the coating and pyrolysis process is that the low temperature molten salts show no significant vapour pressure. This low volatility enables pyrolysis at respective decomposition temperatures and may create heteroatom containing carbon materials. This is hardly possible for molecular substances with low weights since such substances evaporate to a considerable extent upon heating. Within the past years, phosphonium-based ionic liquids gained more attention due to their commercial availability.[35] However, the amount of phosphonium ILs that are available on the market is still limited, especially compared to representatives with the imidazolium cation. A wide range of P-containing ionic liquids is synthetically accessible, and every change in anion or cation may lead to completely different properties.[36] Phosphorus based ionic liquids are suitable precursors for the formation of P-containing carbons that are used in photo-chemistry[7] and –catalysis[37] and as electro-catalysts for the oxygen reduction reaction in fuel cells.[38–42]

In this work, mainly novel phosphonium ionic liquids (see Figure S1) were synthesized in a simple one pot reaction of tributylphosphine with a tri-alkyl-phosphate or alkyl phosphonic acid diethyl ester (phosphonate). This economically attractive approach allows the synthesis of a wide variety of organo-phosphorus compounds with oxygen as the only other heteroatom. Therefore, this synthetic procedure serves the preparation of ionic liquids that contain no boron, nitrogen, sulphur or halides, ensuring that only phosphorous is incorporated

in the resulting carbon material. Another advantage of this method is that variables such as phosphorus content and functional groups in the IL precursors can be adjusted with ease.

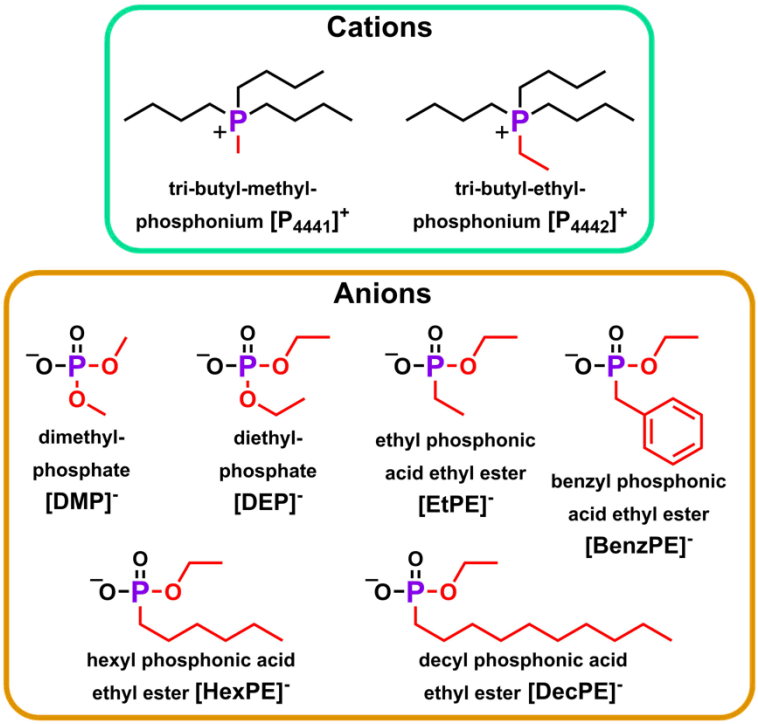

Figure S1. Molecular structures and abbreviations of cations and anions for the synthesized ionic liquids.

2. Supplementary data to PCC-materials

2.1 Characterization

Element mapping with scanning electron microscopy (SEM) was performed on a Zeiss Sigma SEM (Carl Zeiss Microscopy GmbH, Jena, Germany) microscope using energy dispersive X-ray spectroscopy measurements (EDX, X-Max, Oxford Instruments, Whitney, Oxon, UK). Transmission electron microscopy (TEM) was conducted using a JOEL (Tokyo, Japan) JEM-2100 LaB_6 microscope at 200 kV accelerating voltage. TEM-Images with 1024 x 1024 pixels were generated using a Gatan Orius SC1000 CCD camera with 4 s imaging time and binning 2.

X-ray photoelectron spectroscopy (XPS) was performed with an ESCA Mk II spectrometer from Vacuum Generators using a non-monochromatic Al-K_α radiation ($\hbar\omega$ = 1486.6 eV) at a pressure of about 10^{-10} mbar. Survey spectra were recorded at a pass-energy of 50 eV and a step width of 1.0 eV, while for detail spectra the pass-energy and step width were set to 20 eV and 200 meV, respectively. For quantitative analysis of the elemental composition, the photoemission intensities of the detail spectra were scaled with the photoemission cross-sections by Yeh and Lindau[43] after a Shirley background correction[44] was applied.

Powder X-ray diffraction (XRD) was conducted using a D8 Advance (Bruker AXS) diffractometer with Cu-Kα-radiation. Additionally, a beta-filter with variable divergence aperture as well as a Lynxeye-detector in the angle range of 7° to 120° 2θ was used. For the analysis, a Rietveld-refinement was conducted where only the angle range up to 110° 2θ was taken into account.

Pressure dependent powder electron conductivity, apparent density and porosity of commercial carbon materials and P-coated carbons were measured as a function of the pressure using a custom-made powder conductivity test cell (Pulver-Leitfähigkeits-Mess-Zelle, PLMZ) at Hydrogen and Fuel Cell Center (Zentrum für BrennstoffzellenTechnik, ZBT, Duisburg, Germany). The powder sample was placed in the cell between two golden-plated, stainless-steel stamps. Under the lower stamp a mini load cell was positioned which measured the applied pressure of the powder sample. The sample was measured by the four-point probe technique, using two power electrodes and two sense electrodes contacting the two stamps.[45,46] In order to exclude the contact resistances between the powder and the cell, three samples (25, 50 and 75 mg) were tested and two differences (50-25 and 75-25 mg) were calculated and averaged. Each mass of the sample were prepared and measured two times. All discussed specific powder conductivities in S cm^{-1} with respective apparent densities were measured at 100 N cm^{-2}.

Electrochemical investigations were performed using a 0.1963 cm^2 glassy carbon rotating disc electrode (RDE) (HTW Hochtemperatur-Werkstoffe GmbH, Germany) as substrate. For the sample preparation, 2.5 mg of carbon-supported catalysts were dispersed in 150 µL of isopropanol:nafion®117 mixture (49:1) and 150 µL water (ultrapure grade) and then ultra-sonicated for 60 minutes. About 7.5 µL of this ink were transferred onto the glassy carbon electrode and dried in isopropanol-containing atmosphere for 1 hour. Prior to each measurement, the glassy carbon electrode was cleaned with isopropanol, polished with 1.0 µm and 0.3 µm alumina suspension and dried in a closed system containing an isopropanol reservoir to control the drying process.

Steady-state cyclic voltammograms (CV) were recorded with a multi-potentiostat (VMP2, Princeton Applied Research) in a conventional three-electrode cell. A platinum mesh (25 cm^2) and normal hydrogen electrode (NHE, Gaskatel) were employed as counter and reference electrode, respectively. The electrochemical surface area (ECSA) of the catalyst was calculated by integrating the hydrogen desorption region in the CV at 20 mV s^{-1}, assuming that the charge induced by a monolayer of hydrogen atoms on platinum amounts to 210 µC cm^{-2}. The ORR measurements were performed in an oxygen saturated 0.1 M $HClO_4$ electrolyte at rotation range between 100 rpm and 2500 rpm and a cathodic sweep of 5 mV s^{-1}. Mass activities were determined from the current at 0.9 V from rotation at 1600 rpm as commonly used in literature.[47,48]

Full-cell experiments were performed in a 25 cm^2 standard configuration single cell (Baltic FuelCells GmbH, water heated version) with fine flow fields (FFF) bipolar plate design by ZBT. This setup is routinely used for testing fuel cell performance. The polarization curves and electrochemical impedance measurements were performed under H_2/air atmosphere, where

the molar ratio of hydrogen to air (known as stoichiometry coefficient) was 3 and the absolute pressure was 2.5 atm abs. The cell temperature was 80 °C and the relative humidity (RH) for the anode and the cathode was set to 65 %. Platinum phosphorus alloy (PtP) with P-content 1 wt.-% was deposited on cathodes as electrocatalyst by galvanic deposition via pulse plating technique by the Research Institute for Precious Metals and Metal Chemistry[49–52] (Forschungszentrum Edelmetalle Metallchemie, FEM, Schwäbisch Gmünd, Germany). Prepared cathodes were integrated in a membrane electrode assembly (MEA) with an anode, prepared by ZBT, a catalyst HiSPEC® 4000 from Johnson Matthey (180 μg_{Pt} cm^{-2}), and a Nafion® HP membrane. The gravimetrically estimated platinum loading for the cathodes was 100 μg_{Pt} cm^{-2} for 40 wt.-% PtP/carbon. The MEA was hot-pressed at a temperature of 120 °C and a pressure of 20 kg cm^{-2} for 10 minutes. The accelerated degradation test (ADT) consisted of 1000 cycles performed between 0.4 and 1.4 V cell voltage at a scan rate of 1 V s^{-1} and a temperature of 80 °C. During the aging procedure humidified nitrogen (65 % RH) and hydrogen (65 % RH) were supplied to both the cathode and the anode.

2.2 Preparation processing of phosphorus coated carbons

In our first steps towards a new method of synthesizing P-coated carbon materials, several carbon modifications were used as substrates for the coating procedure. The first approaches of pyrolysis were conducted with phosphonium ionic liquids containing either phosphate- or imide-type anions. When phosphate-like anions were used, no changes in the morphology of the carbon substrate could be seen by transmission electron microscopy (TEM) on different carbon substrates. For phosphonium ionic liquids with imide-like anions, for example [P_{2228}][BETI] (tri-ethyl octyl phosphonium bis(perfluoroethylsulfonyl)imide), layer formed was observed in TEM images of various carbon substrates, showing altered morphology. For example, particles and their phase boundaries were sealed with new layers of carbon material (see Figure S2). This change in the original morphology and geometry of the prefabricated carbon is usually not desirable. Therefore, phosphonium ionic liquids with phosphate and phosphonate-derived anions were chosen as the desired type of ionic liquids. The presented method may henceforth be suitable for every kind of carbon material by preserving their promising characteristics without changing the morphology. Furthermore, the chosen class of ionic liquids only introduces phosphorus without potentially additional other heteroatoms. To obtain deeper insight and optimize the parameters for the whole coating procedure, several optimization steps were carried out. In the following paragraphs we only present the best and finally used procedure for our approach without description of the less suitable steps and parameters for the sake of clarity. Besides carbon black CB and carbon nanotubes CNT, graphene nanopowder and carbon particles were evaluated for suitability in the initial stages.

For optimization of the coating procedure itself, different and widely used solvents with varying boiling points and polarities such as isopropyl alcohol, ethanol, acetonitrile, and dichloromethane were evaluated. There was a minor difference between the solvents in terms of resulting materials, hence we chose isopropyl alcohol for its low toxicity and its suitable

boiling point for the wet impregnation method. Investigations revealed that evaporation at 80 °C overnight near its boiling point of 82 °C leads to the best results. In the next step we investigated how much ionic liquid the carbon substrate can adsorb. To this end, a series of coatings with different mass ratios of ionic liquid to carbon substrate were performed. Surprisingly, both CB and CNT could adsorb their own weight in ionic liquid and still be handled as if they were in dry state. When the mass of ionic liquid was significantly larger than that of the carbon substrate, sticky samples were obtained which impedes manual handling. The carbon substrate was dispersed in the ionic liquid and impossible to handle without loss of material, potentially changing the ratio. To compare the different ionic liquids and their amount of phosphorus incorporated into the carbon structure, a ratio of 1 mmol ionic liquid to 0.5 g carbon substrate was chosen. Thus, the same theoretical amount of elemental phosphorus was introduced independent of the ionic liquid, allowing for comparison despite the different molar masses of each IL.

The choice of molar amount of ionic liquid was based on the loading capacity experiments. In the following step of the parameter investigation, different pyrolysis conditions were evaluated. The decomposition temperature of all used ionic liquids lies around 400 °C as described in the ionic liquid section, hence this temperature was chosen as initial temperature for the pyrolysis. In addition to that, materials were treated at a temperature of 1000 °C to investigate phosphorus yield and changes in conductivity and mass activity towards ORR. Analysis of phosphorus content in samples which underwent a second pyrolysis step at 1000 °C showed no significant amounts of phosphorous in the resulting materials. In addition to that, the electronic conductivity of those carbon black samples pyrolyzed at 1000 °C only increased by about 8%, whereas in the final product (pyrolyzed at 400 °C) the conductivity could be increased by 12.6%. This observation leads to the conclusion that for this specific approach, phosphorus groups formed at lower temperatures are more beneficial for electronic conductivity than heat treatment at elevated temperatures without phosphorus groups. Therefore, samples treated at lower temperatures were further investigated. Similar results have not yet been presented in the literature but nonetheless the positive impact of phosphorus groups (on the surface) on electronic conductivity has been reported.[15–17] The mass specific activity towards ORR for samples treated at 1000 °C decreased by 25.5% in comparison to samples treated only at 400 °C.

Figure S2 shows TEM-image of carbon particles coated with IL [P_{2228}][BETI] (tri-ethyl octyl phosphonium bis((perfluoroethyl) sulfonyl)imide).

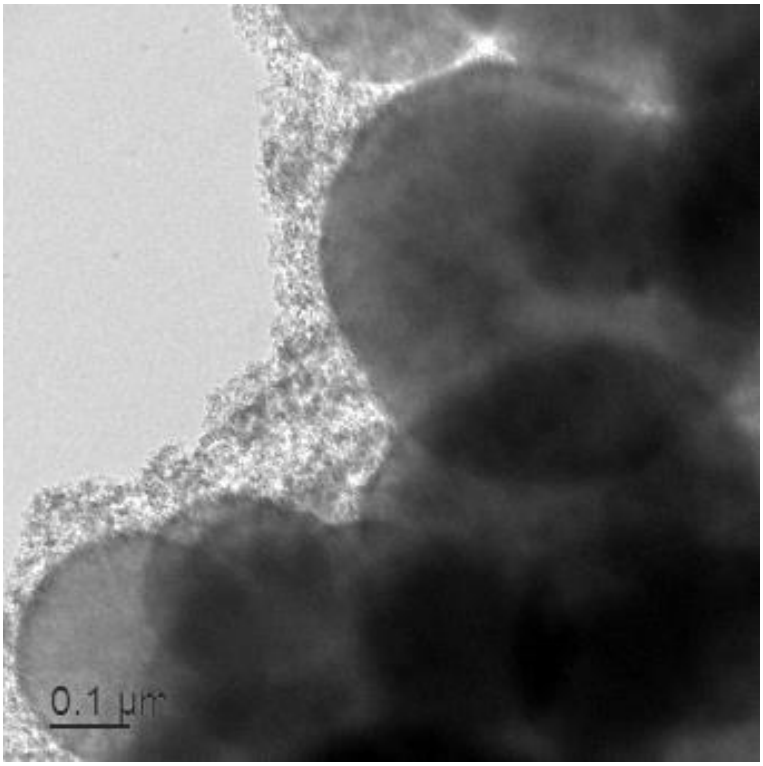

Figure S2. TEM-image of carbon particles coated with $[P_{2228}][BETI]$.

2.3 XPS-measurements

Figure S3 – Figure S6 demonstrate the XPS survey spectra as well as the C1s and O1s spectra for the samples CB/$[P_{4442}]$[DEP], CB/$[P_{4442}]$[HexPe], CNT/$[P_{4442}]$[DEP] and CNT/$[P_{4442}]$[BenzPE], respectively. For the sample CB/$[P_{4442}]$[HexPe], also the Na1s spectrum is shown. For the samples CB/$[P_{4442}]$[DEP], CNT/$[P_{4442}]$[BenzPE] and CNT/$[P_{4442}]$[DEP], the survey spectra display only carbon, oxygen and phosphorous, while for the sample CB/$[P_{4442}]$[HexPe] an additional Na1s peak is observed in Figure S4a.

For all samples, the C1s spectra in Figs. S3.(b) – S6.(b) display the main peak at about 284 eV that represents the C−C bonds of the hexagonal network[53]. The additional shoulder ranging up to approx. 292 eV is caused by carbon oxygen species as well as by the so-called shake-up satellite[54].

The O1s spectra in Figs. S3.(c) – S6.(c) display a peak at about 532 eV which is typical for phosphates. For the sample CB/$[P_{4442}]$[HexPe], the peak in Fig. S4c is slightly shifted to higher binding energies due to the significantly increased amount of PO_3, as shown in Figure 9(b).

Figure S3, Figure S4, Figure S5 and Figure S6 display the survey, C1s, O1s and Na1s XPS spectra of respective samples.

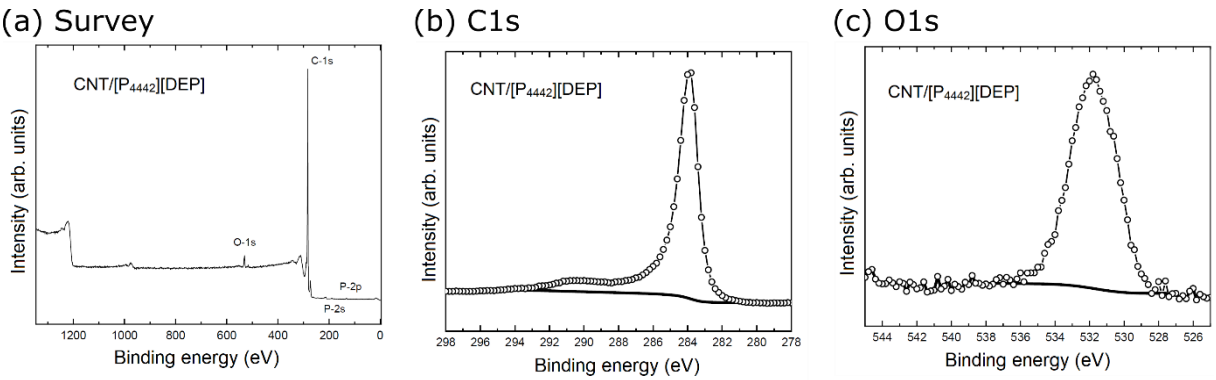

Figure S3. XPS spectra of CB/[P_{4442}][DEP]; survey (a), C1s (b) and O1s (c).

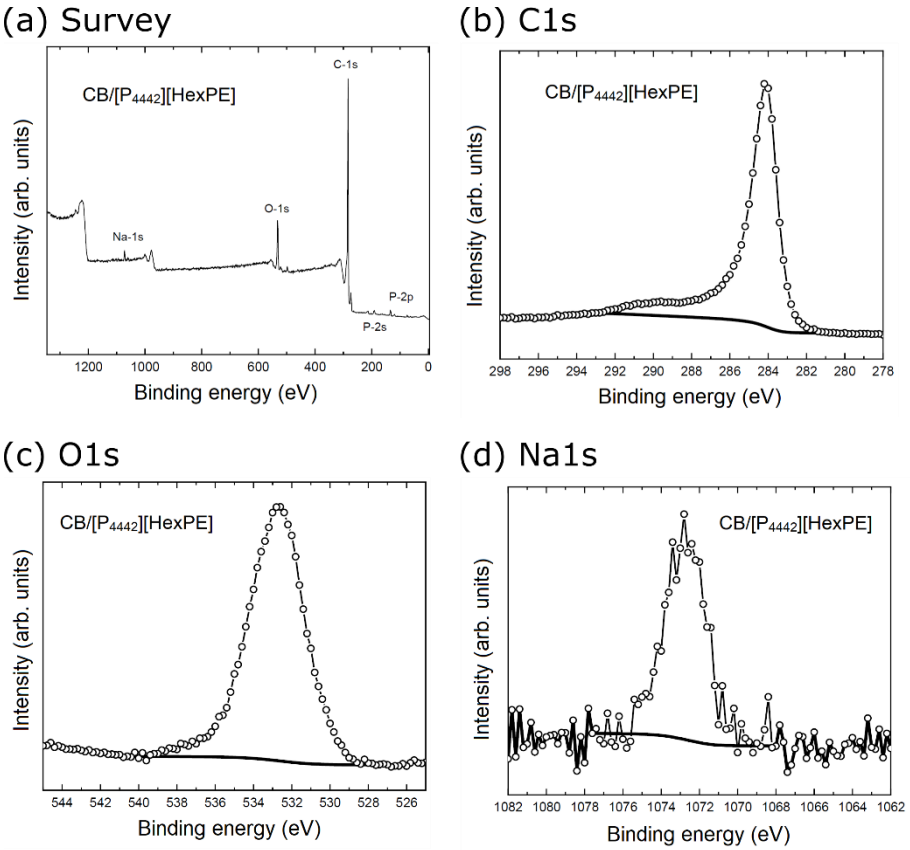

Figure S4. XPS spectra of CB/[P_{4442}][HexPE]: survey (a), C1s (b), O1s (c) and Na1s (d).

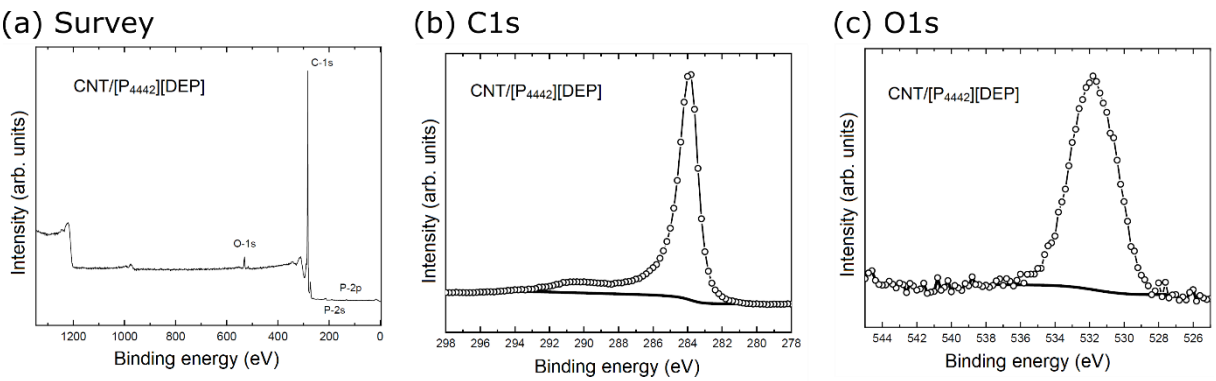

Figure S5. XPS spectra of CNT/[P_{4442}][DEP]: survey (a), C1s (b) and O1s (c).

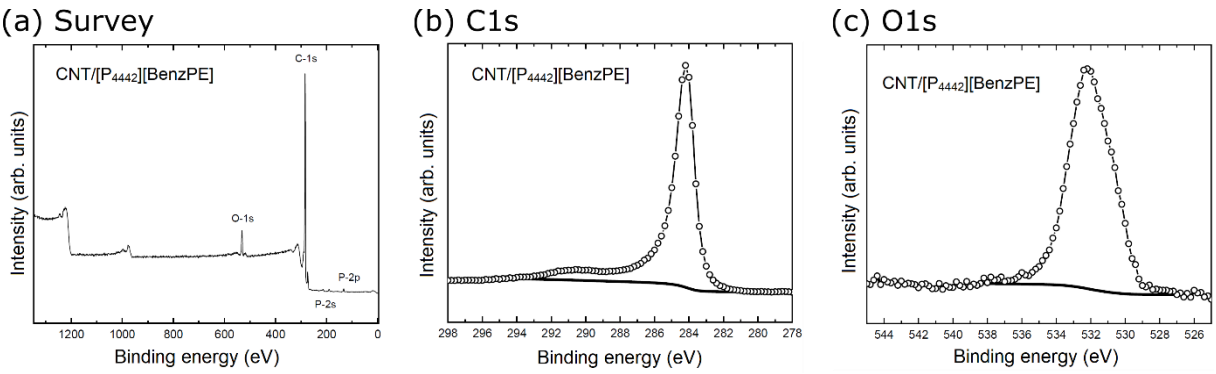

Figure S6. XPS spectra of CNT/[P_{4442}][BenzPE]: survey (a), C1s (b) and O1s (c).

2.4 Half-cell measurements

All measurements were conducted in a three-electrode assembly using a 0.1 M $HClO_4$ solution. The electrochemical active surface area was calculated using equation (1). The actual platinum loading of samples $m_{\mathrm{Pt,TGA}}$ was obtained by thermo gravimetric analysis. The mass specific activity towards ORR a_{mass} was calculated using Equation (2).

$$ECSA = \frac{A_{\mathrm{H}}}{m_{\mathrm{Pt,electrode}}\,\mathrm{C}\,\nu} \tag{1}$$

$$a_{\mathrm{mass}} = \frac{|I_{0.9\mathrm{V}}|}{m_{\mathrm{Pt,electrode}}} \tag{2}$$

In the equation shown above, A_{H} is the integral area of hydrogen desorption region, C the charge induced by mono layer of hydrogen atoms, ν the sweep rate, $|I_{0.9\mathrm{V}}|$ the absolute value of the current measured at 0.9 V in RDE at 1600 rpm, and $m_{\mathrm{Pt,electrode}}$ the amount of platinum on the electrode calculated from $m_{\mathrm{Pt,TGA}}$. The obtained data are listed in Table S1 and Table **S2**.

Table S1. Values of $ECSA$, $|I_{0.9\mathrm{V}}|$ and a_{mass} obtained by half-cell measurements for carbon black based materials with respective platinum loading $m_{\mathrm{Pt,TGA}}$ obtained by TGA.

	$m_{\mathrm{Pt,TGA}}$ (%)	$ECSA$ ($m^2\ g^{-1}$)	$\lvert I_{0.9\mathrm{V}}\rvert$ (mA)	a_{mass} (mA mg^{-1})
HISPEC4000	39.5	73.02	0.666	26.9
Pt@CB/Pure	23.6	85.29	0.542	36.6
Pt@CB/Blank	36.2	59.30	0.516	22.6
Pt@CB/[P_{4441}][DMP]	29.3	74.55	0.609	33.9
Pt@CB/[P_{4442}][DEP]	30.0	69.07	0.691	37.3
Pt@CB/[P_{4442}][EtPE]	27.5	84.80	0.565	33.2
Pt@CB/[P_{4442}][HexPE]	27.4	76.04	0.726	42.3
Pt@CB/[P_{4442}][DecPE]	29.4	77.65	0.564	30.6
Pt@CB/[P_{4442}][BenzPE]	28.5	66.89	0.588	33.7

Table S2. Values of $ECSA$, $|I_{0.9V}|$ and a_{mass} obtained by half-cell measurements for carbon nanotube-based materials with respective $m_{Pt,TGA}$ obtained by TGA.

	$m_{Pt,TGA}$ (%)	$ECSA$ ($m^2\ g^{-1}$)	$\lvert I_{0.9V}\rvert$ (mA)	a_{mass} ($mA\ mg^{-1}$)
HISPEC4000	39.5	73.02	0.666	26.9
Pt@CNT/Pure	37.5	26.98	0.457	19.3
Pt@CNT/Blank	36.2	35.91	0.562	24.8
Pt@CNT/[P_{4441}][DMP]	31.3	33.13	0.531	27.7
Pt@CNT/[P_{4442}][DEP]	32.1	48.12	0.626	31.4
Pt@CNT/[P_{4442}][EtPE]	32.3	27.59	0.495	24.0
Pt@CNT/[P_{4442}][HexPE]	31.7	37.71	0.517	26.3
Pt@CNT/[P_{4442}][DecPE]	31.4	31.75	0.518	26.2
Pt@CNT/[P_{4442}][BenzPE]	31.3	40.32	0.635	32.5

The Koutecky-Levich-Plots were derived by plotting of j^{-1} against $\omega^{-1/2}$ according to equation (3),

$$\frac{1}{j} = \frac{1}{B \cdot \sqrt{\omega}} + \frac{1}{j_k} \tag{3}$$

In equation (3), j is the current density, B the Levich-constant, ω is the rotating speed and j_k the kinetic current. B is the slope of the linear regression. The number of electrons n is calculated from equations (4) and (5).

$$B = 0{,}2 \cdot n \cdot F \cdot c_{O_2} \cdot D^{2/3} \cdot \nu^{-1/6} \tag{4}$$

$$n = \frac{B}{0{,}2 \cdot F \cdot c_{O_2} \cdot D^{2/3} \cdot \nu^{-1/6}} \tag{5}$$

In the equations shown above, F is the Faraday constant, c_{O_2} the concentration of oxygen in bulk liquid ($1.18 \cdot 10^{-6}$ mol cm^{-3})[55], D the diffusion coefficient of oxygen ($1.9 \cdot 10^{-5}$ $cm^2\ s^{-1}$)[55], and ν the viscosity of the electrolyte ($9.87 \cdot 10^{-3}$ $cm^2\ s^{-1}$)[56]. All values from literate relate to a 0.1 M $HClO_4$-solution. The values for the calculations are displayed in Table S3 and Table S4.

Table S3. Values used for Koutecky-Levich-plots obtained from LSV diagrams at 0.2 V at related rotation speeds.

ω (rpm)	j(Pt@CB(pure)) ($mA\ cm^{-2}$)	j(Pt@CB/ [P_{4442}][HexPE]) ($mA\ cm^{-2}$)	j(Pt@CNT(pure)) ($mA\ cm^{-2}$)	j(Pt@CB/ [P_{4442}][BenzPE]) ($mA\ cm^{-2}$)
100	1.342	1.320	1.386	1.347
400	2.600	2.729	2.753	2.725
900	3.564	4.162	4.205	4.120
1600	4.155	5.664	5.643	5.532
2500	4.375	7.272	7.086	6.950

Table S4. Values from linear regression of Koutecky-Levich-plots B^{-1}, B, $\Delta B/B$, ${j_k}^{-1}$, j_k, $\Delta j_k/j_k$, R^2, and n of the platinum decorated samples at 0.2 V.

value	Pt@CB(pure)	Pt@CB/ $[P_{4442}][HexPE]$	Pt@CNT(pure)	Pt@CB/ $[P_{4442}][BenzPE]$
B^{-1} ($rpm^{1/2}$)	6992,8	7746,3	7250,0	7478,4
B (10^3 $rpm^{-1/2}$)	0,143	0,138	0,129	0,134
$\Delta B/B$ (%)	3,10	0,50	0,48	0,25
${j_k}^{-1}$ (cm^2 mA^{-1})	43,572	−17,457	−2,506	−5,665
j_k (mA cm^{-2})	0,023	−0,399	−0,057	−0,177
$\Delta j_k/j_k$ (%)	33,46	−79,02	−11,46	−18,18
R^2	0,9981	0,9999	0,9999	0,9999
n	4,1	3,8	3,8	3,8

Figure S7 shows Koutecky-Levich-Plots at 0.2 V vs NHE of both pure carbon black (a) and carbon nanotubes (c) materials as well as with phosphorus coating (b) and (d). The average number of electrons $\bar{n}$ was calculated from plots at 0.2 V vs NHE and 0.4 V vs NHE.

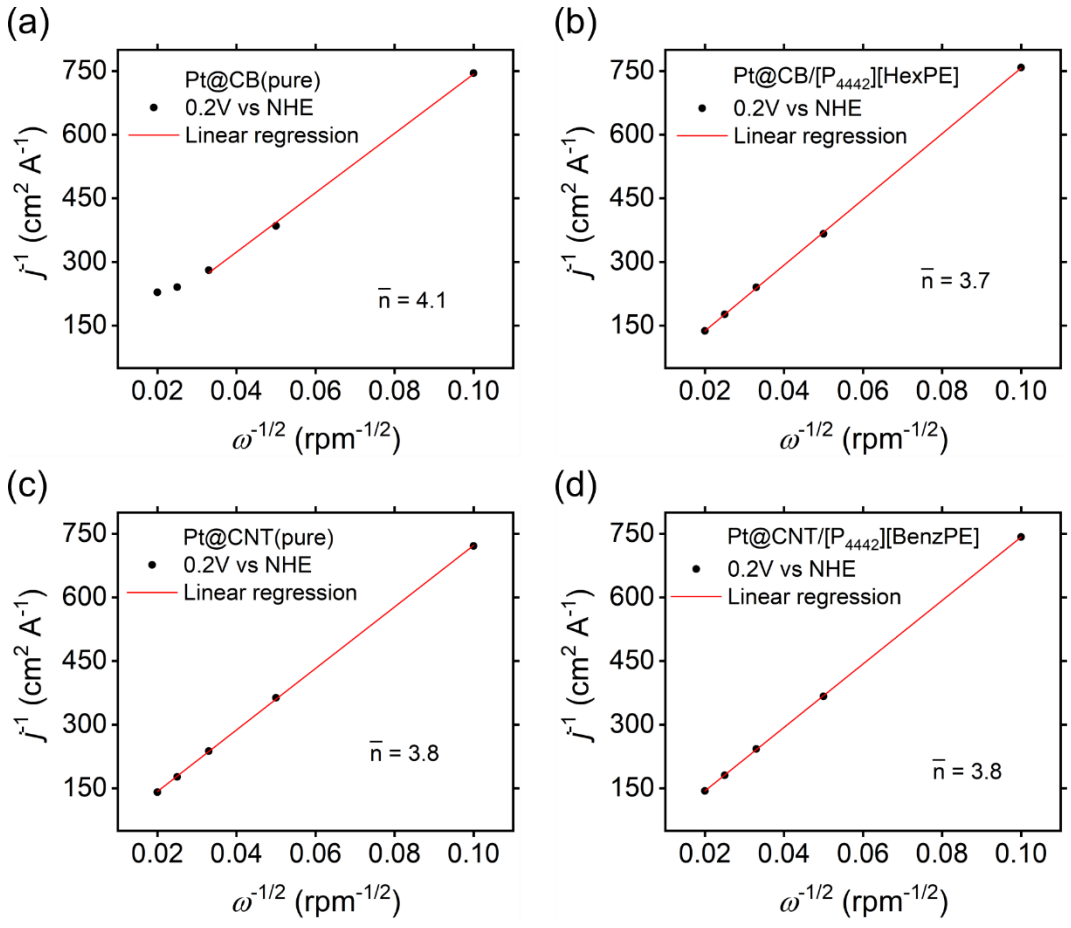

Figure S7. Koutecky-Levich-Plots of CB- and CNT-based materials with linear regression and resulting average number of electrons $\bar{n}$ at 0.2 V vs NHE.

Figure S8 shows a comparison of LSV curves at different rotation speeds for the samples Pt@CB(pure) and Pt@CB/[P_{4442}][HexPE], clearly displaying the difference in LSV curves of both samples.

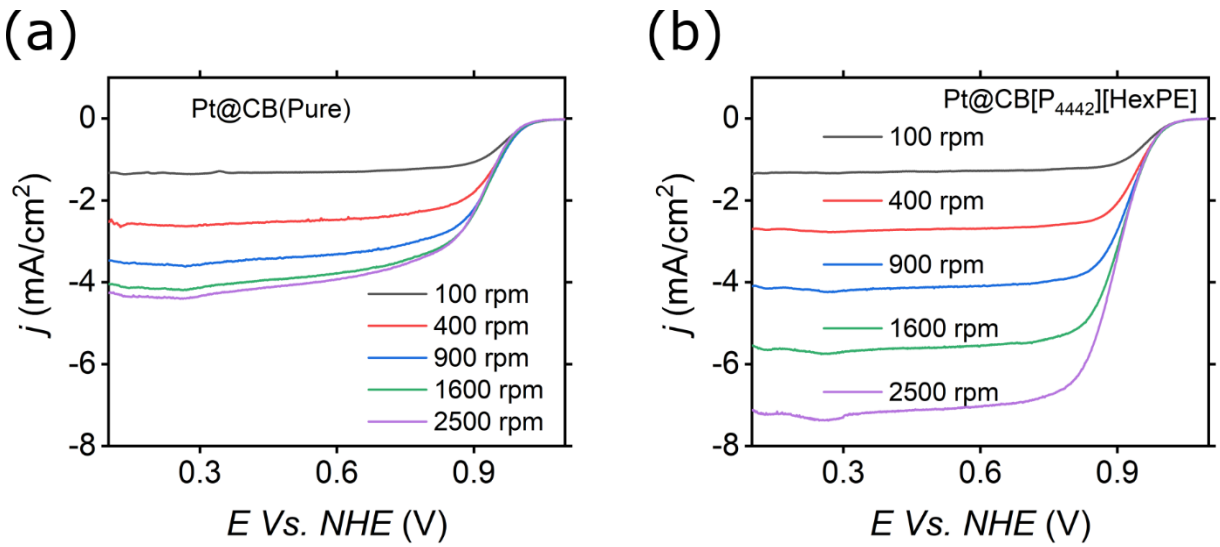

Figure S8. LSV-curves obtained by RDE-measurements at various rotating speeds for (a) Pt@CB(pure) and (b) Pt@CB/[P_{4442}][HExPE].

2.5 Full-cell measurements

The pulse plating technique for platinum phosphorus deposition at FEM was conducted from the aqueous electrolyte of $Pt(NH_3)_2(NO_2)_2$ (c = 8 g L^{-1}), $NaCH_3COOH$ (c = 70 g L^{-1}) and Na_2CO_3 (c = 100 g L^{-1}). H_3PO_3 (c = 0.13 g L^{-1}) was used as the phosphorus source. The procedure was conducted at 30 °C on a 35 x 35 mm gas diffusion layer (the active area was 30 x 30 mm) with the following parameters: I_{max} 5 A; t_{on} 0.005 s; t_{off} 0.195 s. All solutions were prepared using analytical grade chemicals. The plasma treatment at FEM was carried out under following parameters. During operation, the pressure was 0.07 mbar using an Ar/O_2-mixture in a ratio of 3:7 ratio. For the plasma excitation, 1.5 µs pulsed DC-current with a 150 kHz frequency was used for 5 minutes. The company-specific program A02 (company secret) at Plasmatreat GmbH was used for the plasma treatment. The working distance was 4 mm with a 2 m min^{-1} feed rate at a 2700 rpm rotation rate. The track patch was 22 mm and 2 cycles at 340 V and 420 W were conducted in air atmosphere at a gas flow of 2.4 m^3 h^{-1}.

Figure S9 show the results from full-cell measurements without plasma treatment where the cathodes do not possess enough electrochemical active surface area ECSA, evidenced by the high cathode charge transfer resistance R_c, and are very hydrophilic due to the PTFE-free coated layer of the carbon support and the low ionomer loading (I/C volumetric ratio of 0.1). For new cathodes it can be seen in the U/j-curves that GDS coated with P-CB shows superior fuel-cell performance compared to GDS coated with pure CB. The pure carbon black samples demonstrate a curve which terminates at 0.7 A cm^{-2}, possibly due to the strong hydrophilic character of the cathode. According to literature[8,12], the discovered PO_3- and PO_4-species

possess hydrophilic character too, but phosphorus groups are only present at the surface of the carbon material. This may be a hint that the phosphorus species promote an effect similar to plasma treatment prior to catalyst deposition. The beneficial properties of hydrophilic phosphorus species lies in good agreement with the literature where PCC materials served as support for noble metal catalysts.[13,14] After accelerated degradation tests ADT, both cathodes show similar curves and performance, but GDS coated with pure CB possesses lower resistances. The O_2-diffusion R_{diff} and the cathodic transfer resistances R_{c} are the major factors to increase the resistances of fuel cell systems without plasma treatment after ADT. The ohmic resistance R_{ohm} contributes only with around 50 mΩ cm^{-1} to the overall resistance.

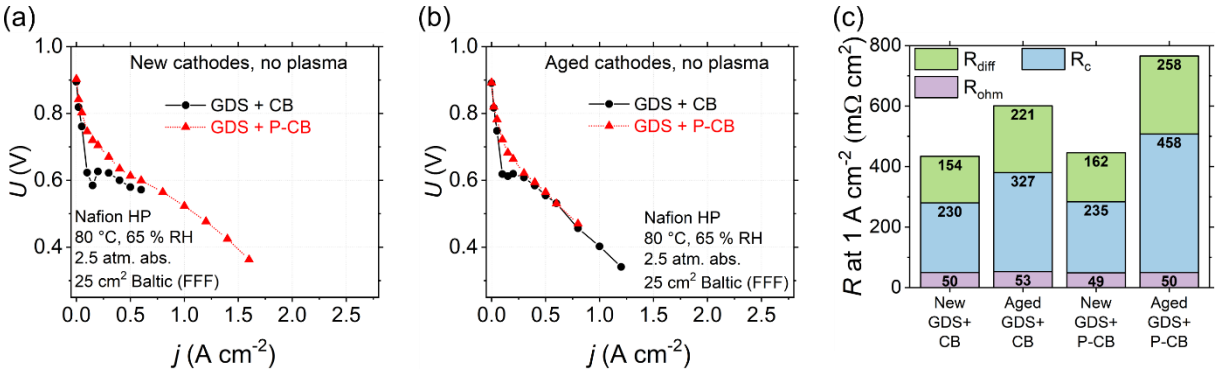

Figure S9. Results from full-cell-experiments without plasma treatment for GDS coated with CB and P-CB: *U*/*j*-diagram of new (a) and aged (b) cathodes with respective resistances (c) of new and aged cathodes in a 25 cm^2 Baltic fuel cell test system. The drawn lines in (a) and (b) are a guide to the eye.

In Figure S10, the results from fuel cell testing with plasma treatment from FEM are displayed. It can clearly be seen that plasma treatment prior to electrodeposition of catalyst improves the performance of cathodes, especially when coated with pure and P-coated CB. This is of no surprise since the plasma treatment ensures a thin hydrophilic layer of PTFE- and ionomer-free carbon surface for an electrodeposition of Pt with high ECSA and at the same time preserves the hydrophobicity of the gas diffusion layer (GDL) which is crucial for the water management. A high quantity of liquid water in the cell results in flooding of the catalyst layer and blocking the access of oxygen to the ORR reactive sites, preventing further reactions, and limiting the fuel cell performance. In the case of plasma treatment by FEM, GDS coated with P-CB improved the performance of the cathode in comparison to GDS coated with pure CB. After ADT, all three systems show similar *U*/*j*-curves. In terms of resistances, uncoated GDS possesses the highest resistances for new and aged cathodes. When coated with CB, the resistance values decrease considerably for cathodic transfer resistance R_{c}. Coating with P-CB leads to even smaller overall resistance where both cathodic transfer and O_2-diffusion resistances decrease. After the aging procedure, all systems show a considerable increase in the overall resistances. For pure GDS, the major increase in overall resistance comes from O_2-diffusion. For cathodes coated with CB and P-CB, both R_{diff} and R_{c} increase remarkably after ADT. Of all systems treated with FEM plasma, GDS coated with P-CB demonstrate the smallest

resistance values despite possessing small anodic charge transfer resistance R_a of 7 mΩ cm^{-1} (new) and 8 mΩ cm^{-1} (aged), respectively.

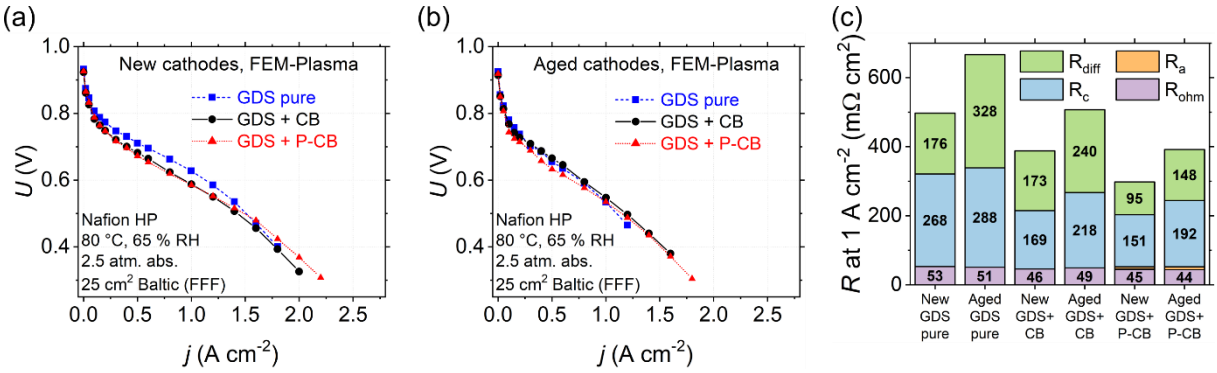

Figure S10. Results from full-cell-experiments with plasma treatment by FEM for GDS and GDS' coated with CB and P-CB: *U*/*j*-diagram of new (a) and aged (b) cathodes with respective resistances (c) of new and aged cathodes in a 25 cm^2 Baltic fuel cell test system. The drawn lines in (a) and (b) are a guide to the eye.

Results of plasma treatment of GDL systems conducted by Plasmatreat GmbH are shown in Figure S11. Plasma treatment increases the hydrophobicity and performance of all gas diffusion systems compared to systems without plasma treatment, as expected. For the new cathodes, GDS coated with P-CB shows the most favourable *U*/*j*-curve of all three investigated systems. After accelerated degradation tests, all three systems show similar curves and performance. The resistances of plasma treated systems decrease drastically compared to untreated systems. The overall resistances are below 350 mΩ cm^2, which are even lower than overall resistances obtained from FEM plasma-treated samples. Pure GDS samples are the only systems to possess small anodic transfer resistance R_a. The described trend for systems treated with FEM plasma applies for these systems as well. GDS without coating show highest overall resistances, but ADT have an exceedingly small effect on R_c of this sample. Coating with CB and P-CB decreases the overall resistances of the test systems by ca. 50 mΩ cm^2. In contrast to uncoated GDS, both of the coated GDS display remarkable cathodic charge transfer and O_2-diffusion resistances after ADT. Untreated GDS samples show anodic charge transfer resistance R_a of 9 mΩ cm² (new) and 9 mΩ cm² (aged), respectively.

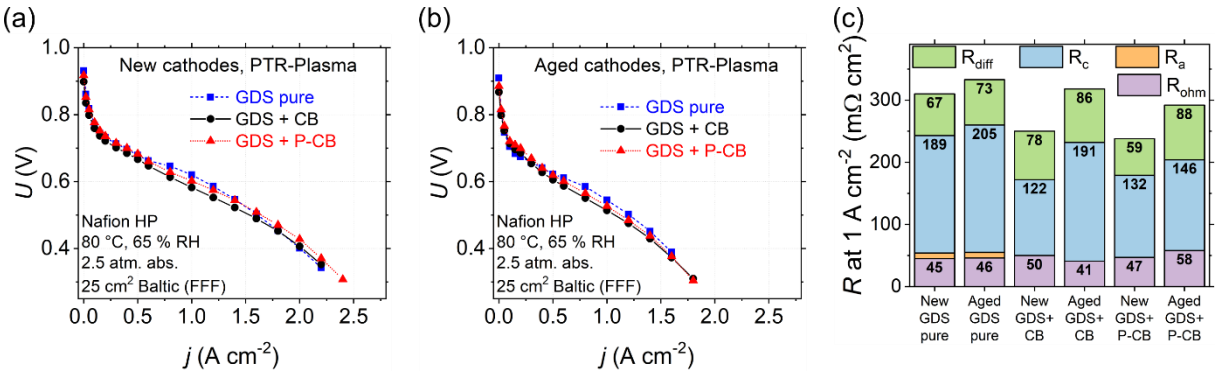

Figure S11. Results from full-cell-experiments with plasma treatment by Plasmatreat GmbH for GDS and GDS' coated with CB and P-CB: *U*/*j*-diagram of new (a) and aged (b) cathodes with respective resistances (c) of new and aged cathodes in a 25 cm^2 Baltic fuel cell test system. The drawn lines in (a) and (b) are a guide to the eye.

3. Physicochemical characterization of ionic liquids

Thermal properties and liquid ranges of ionic liquids are in the determination of their operational range.[29] For the coating method and approach in this work, knowledge of solidification behavior is crucial because crystallization is a major problem for homogeneous adhesion which in turn is required to achieve homogenous coating of the substrate. Similar to the IL [Bmim][PF_6] (1-butyl-3-methylimidazolium hexafluorophosphate) used by Li *et al.*[57], it is of upmost importance that the ionic liquids in this work are liquid at ambient temperature where the adhesion takes place. Li and co-workers relied on an ultrasonic bath to mix carbon substrate and ionic liquid followed by drying at elevated temperature in vacuum. Otherwise, inhomogeneous and bulky phosphorus coatings may reduce the quantity of active sites and increase the heterogeneity of the coated particles. As the glass transitions of ILs are far below ambient temperature, the melting point is the relevant thermal transition for the coating process. Results of thermal investigations from DSC and TGA are presented in Table S5. All ILs have glass transitions in the range of −76 °C to −57 °C and one of the samples crystalized upon cooling. In addition, the ionic liquids [P_{4441}][DMP] and [P_{4442}][BenzPE] are showing cold crystallization T_{cc} (crystallization from the liquid in the heating cycle of the DSC) and melting (m) transition behavior. The DSC results for the ionic liquid [P_{4441}][DMP] lies in agreement with already reported data Yoshii and co-workers.[58] These authors described that some ionic liquids tend to crystallize in 3-dimensional spherical structures or as plastic crystal phases. It can be suggested that both [P_{4441}][DMP] and [P_{4442}][BenzPE] possess such plastic crystal phases in the range between T_{cc} and T_m. For the ionic liquids based on phosphonate anions, there is no reported data in the literature, but nonetheless a trend can be observed. From ethyl- to hexyl-chain, the glass transition temperature slightly decreases and rises again to a decyl-chain. An explanation for this behavior results from the Van-der-Waals-interactions of the alkyl chains, where moderate chain length leads to an increasing asymmetry of the ions while long alkyl groups tend to form nanostructures that lead to higher molecular interactions

and increased glass transition temperatures. These findings are similar to the situation where cations with increasing length of a single hydrocarbon chain are used.[30] The relatively long chain of decyl with nine CH_2-sequences may lead to increasing Van-der-Waals interaction resulting in higher T_g and T_m. The glass transition and melting temperatures of $[P_{4442}]$[BenzPE] are the highest among all investigated ionic liquids. This is presumably because the benzoyl-ring is inflexible and may stack easily with rings from other ionic liquid molecules and thus expanding the intermolecular forces by additional π-interactions. The samples with melting points slightly above ambient temperature, $[P_{4442}]$[DMP] and $[P_{4442}]$[BenzPE], showed pronounced supercooling, i.e., remained in liquid state below their melting points. Thus, all the samples were applicable for the coating procedure.

Table S5. Results of thermal investigation by means of DSC and TGA for the investigated phosphonium ionic liquids.

Ionic liquid	T_g (°C)	T_{cc} (°C)	T_m (°C)	T_d (°C)	$\rho^{25\,°C}$(g mL^{-1})	$V_M^{25\,°C}$ (mL mol^{-1})
$[P_{4441}]$[DMP]	−67	-20	26	383	1.030	332.5
$[P_{4442}]$[DEP]	−71	-/-	-/-	406	1.007	381.9
$[P_{4442}]$[EtPE]	−75	-/-	-/-	400	0.991	371.7
$[P_{4442}]$[HexPE]	−76	-/-	-/-	-/-	0.959	472.9
$[P_{4442}]$[DecPE]	−72	-/-	-/-	-/-	0.948	537.3
$[P_{4442}]$[BenzPE]	−57	4	35	-/-	1.028	417.0

Thermogravimetric analysis was performed for the ionic liquids in order to gain insight into their thermal decomposition behavior. The measurements were carried out under N_2-atmosphere similar to the pyrolysis conditions for the P-coating. The decomposition temperatures T_d and TGA diagrams of $[P_{4441}]$[DMP], $[P_{4442}]$[DEP] and $[P_{4442}]$[EtPE], shown in Table S5 and Figure S12, are presented as an example. TGA values of other phosphonate based ionic liquids were not investigated due to small structural changes with no significant effect on general decomposition behavior. The decomposition behavior of $[P_{4441}]$[DMP] is similar to that reported by Yoshii *et al.*[57], however the authors used a heating rate of 10 °C min^{-1} resulting in T_d to be 310 °C and therefore significantly lower compared to our work. The ionic liquid $[P_{4442}]$[DEP] decomposes above 500 °C without residue, whereas compounds $[P_{4441}]$[DMP] and $[P_{4442}]$[EtPE] show a residual mass of about 5 % after decomposition. All ionic liquids show a three-step decomposition curve where the major decomposition processes come from the second and third step. For the decomposition temperature T_d the second step was used. A trend among these three ionic liquids is clearly visible: increase in the molecule size from $[P_{4441}]$[DMP] to $[P_{4442}]$[DEP] results in an increase of the decomposition temperature. In the same way, upon reduction of the molecule size through O_2-elimination from one ethyl ester group in $[P_{4442}]$[DEP] to give $[P_{4442}]$[EtPE], T_d decreases by several degree Celsius. This trend lies in agreement to the literature[59,60] where it is reported that the thermal stability of ionic liquids is mainly influenced by the anion. In general, thermal degradation is strongly dependent on experimental parameters such as the mass of the sample or the heating rate.[61]

The results also hint towards ionic liquids with phosphonate based anions having slightly improved thermal stability in comparison to ionic liquids with phosphate based anions. To confirm this, further research with a wider range of ionic liquids needs to be conducted. Nonetheless, since the decomposition of the investigated pure ionic liquids takes place at around 400 °C, this temperature was chosen for pyrolysis. It should furthermore be taken into account that ionic liquids adsorbed on the carbon surface may show different decomposition behavior than bulk ionic liquids due to interactions between carbon surface and ionic liquid.[62]

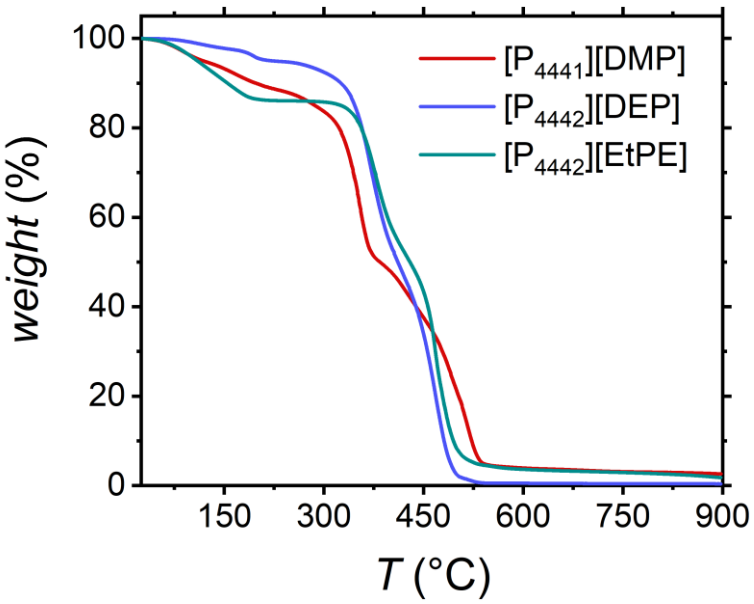

Figure S12. TGA curves of $[P_{4441}][DMP]$, $[P_{4442}][DEP]$ and $[P_{4442}][EtPE]$ using 20 °C min^{-1} heating rate under N_2-flow of 20 mL min^{-1}.

With regards to densities, a clear trend can be observed among all ionic liquids. Densities are decreasing with longer alkyl chains, thus lower amounts of oxygen and phosphorus, in ionic liquids with both phosphate and phosphonate anion. $[P_{4442}][BenzPE]$ is similar to $[P_{4441}][DMP]$ in density which can be justified through the rigid benzene-ring and additional π-interactions.

Investigation of rheological properties of ILs is in general of immense importance because the low temperature molten salts usually have viscosities that are at least a 10-degree higher than those of molecular solvents. However, for the coating process, higher viscosities of the coating species can be advantageous since they prevent draining of fluids from the substrate. Dynamic viscosity at 25 °C and VFT fitting parameters of the phosphonium ILs are given in Table S6 and plotted in Figure S13. All ionic liquids follow the VFT equation and experimental values can be found in the supporting information. Two trends can be observed: the first is that for ionic liquids with phosphate anions, an increasing alkyl chain length leads to lower viscosities. This may be a hint that in this type of ionic liquid longer alkyl chains may benefit from comparable weak, short-range Van-der-Waals-interactions weakening the strong, long-range Coulombic interactions between the ions. For ionic liquids with phosphonate anion, longer alkyl chains or sterically demanding groups like benzoyl increase the viscosity of the ionic liquids.

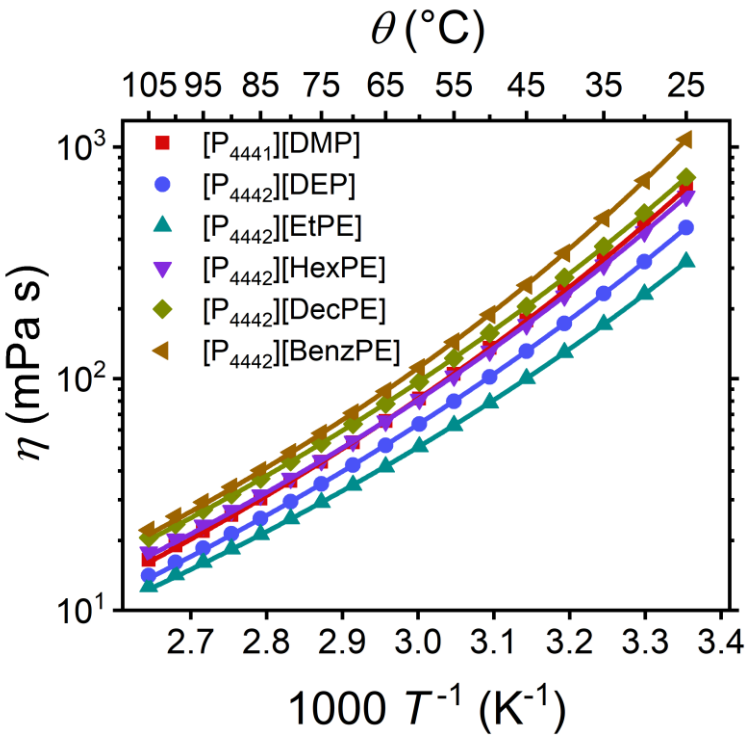

Figure S13. Progression of dynamic viscosity with temperature for phosphonium ionic liquids. The drawn lines are the VFT fits.

Table S6. Zero-shear viscosity η_0 at 25 °C and VFT equation fit parameters (η_0, B and T_0) of the viscosity data of investigated phosphonium ionic liquids.

Ionic liquid	η (mPa s)	η_0 (10^{-1} mPa s)	B (K)	T_0 (K)
[P_{4441}][DMP]	663.4	0.49	1188	173.4
[P_{4442}][DEP]	448.6	0.54	1145	171.2
[P_{4442}][EtPE]	319.2	0.88	994.6	176.8
[P_{4442}][HexPE]	611.6	0.78	1083	177.4
[P_{4442}][DecPE]	738.4	0.80	1121	175.5
[P_{4442}][BenzPE]	1077	1.12	980.9	191.2

Reasons for this behaviour may lie in Van-der-Waals attraction, as smaller ions otherwise tend to have higher viscosities due to stronger Coulomb attractions. With increasing ion size the Van-der-Waals-interactions increase as well, resulting in higher viscosity values. Longer alkyl chains directly attached at the phosphorus in the anion may promote this phenomenon. Glass transition temperature and dynamic viscosity often show similar trends. As discussed earlier, higher dynamic viscosity is the consequence of stronger attractive forces which are influenced by the ion size. Ionic liquids containing large anions like $[BenzPE]^-$ show the highest T_g and highest dynamic viscosity. In addition, small anions like $[DMP]^-$ lead to pronounced Coulombic interactions, resulting in high glass transition temperature and dynamic viscosity values. This phenomenon is not very pronounced for ionic liquids such as [P_{4442}][EtPE] and [P_{4442}][HexPE], but nonetheless observable. The interrelation between glass transitions and absolute values of viscosity for ionic liquids as fragile glass formers is investigated and already reported.[63]

Depending on future and desired application the investigated ionic liquids may be also utilized in the fields of lubrication and extraction in liquid phase.[64–68]

Molar conductivity is another transport property that is important for practical applications, for example when ionic liquids are used as electrolytes in novel batteries.[29,69] Especially for the field of electrochemical devices, favourable molar conductivities are crucial for high end performance. The molar conductivity is temperature dependent with inverse behaviour to the viscosity (Walden relation, Equation (4)). When high temperature windows for operations are desired, high conductivity values are another factor to be considered. Temperature dependent molar conductivity, demonstrated in Figure S14, shows only minor differences of molar conductivity between certain ionic liquids. For example, the difference in molar conductivity between both IL containing phosphate anions, $[DMP]^-$ and $[DEP]^-$, is exceedingly small, only $0.9 \cdot 10^{-2}$ S cm² mol^{-1}. In contrast to that, the ionic liquids with phosphonate anions display more pronounced results. The IL $[P_{4442}][EtPE]$ shows the highest molar conductivity. With increasing alkyl chain length from hexyl to decyl the molar conductivity decreases significantly, with $[P_{4442}][BenzPE]$ showing a conductivity between the latter two. These trends are also observed in the VFT results displayed in Table S7. As stated by the Walden rule and Walden plot, molar conductivity and dynamic viscosity show inverse behaviour to one another. This observation has been confirmed through several investigations for other phosphonium based ionic liquids.[70–72] However, the coupling between viscosity and conductivity varies from different ILs which explains the higher conductivity of $[P_{4442}][BenzPE]$ compared to $[P_{4442}][DecPE]$ despite the viscosity of the latter being lower.[63] Again, the most promising characteristic for many applications, i.e. the highest conductivity, is found for $[P_{4442}][EtPE]$.

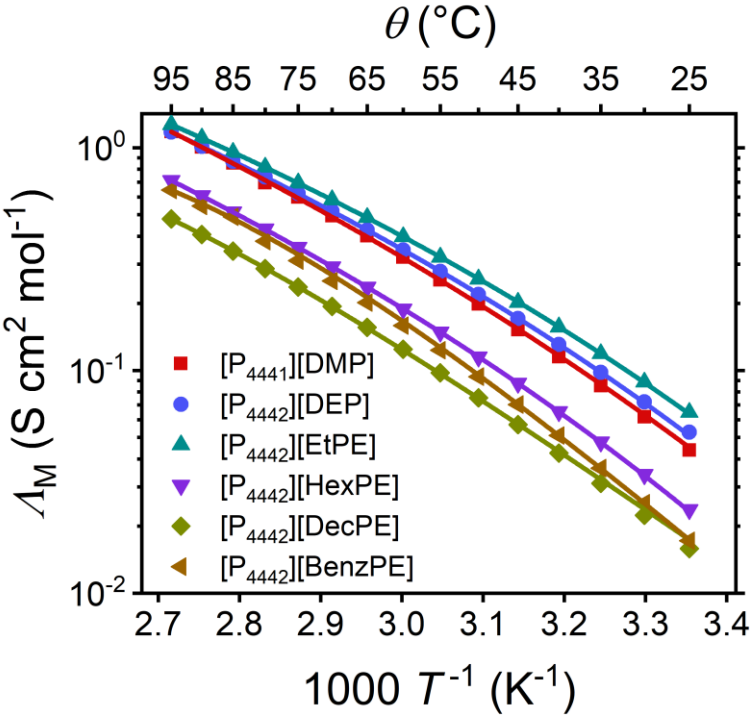

Figure S14. Progression of molar conductivity with temperature for phosphonium ionic liquids. The drawn lines are the corresponding VFT-fits.

Table S7. Molar conductivity at 25 °C and VFT equation fit parameters ($\Lambda_{M,0}$, B and T_0) of the molar conductivity data of investigated phosphonium ionic liquids.

Ionic liquid	$\Lambda_M^{25\,^\circ C}$ (10^{-2} S cm² mol^{-1})	$\Lambda_{M,0}$ (S cm² mol^{-1})	B (K)	T_0 (K)
[P_{4441}][DMP]	4.39	523.0	−1215	168.9
[P_{4442}][DEP]	5.28	280.5	−1054	175.7
[P_{4442}][EtPE]	6.48	225.0	−990.6	176.8
[P_{4442}][HexPE]	1.27	262.8	−1130	177.1
[P_{4442}][DecPE]	1.58	238.7	−1219	171.8
[P_{4442}][BenzPE]	1.72	84.9	−737.0	210.6

Viscosity influences the molar conductivity and these two properties show inverse behaviour to one another, as expressed by the Walden relation, Equation (4) and as displayed in Figure S15. All ionic liquids show straight lines in a close range. The ionic liquid [P_{4441}][DMP] is closest to the bisection in the Walden plot, which is sometimes referred to as "ideal" KCl line, followed by [P_{4442}][DEP] and [P_{4442}][EtPE]. The fitting parameters with respective deviation are given in the ESP†. The log(*C*) value from equation (6) tends to be a good indicator for the overall performance of a specific ionic liquid, making it more favourable compared to other investigated ionic liquids. With regard to Table S8 and Table S11 where the plot parameters are displayed, the log(*C*) value follows the trend of the Walden plot from Figure S15. With no significant structural changes among the examined ionic liquids, the relatively narrow range of the resulting Walden plots is everything else but expected. The reciprocal Haven ratio H_R^{-1}, the Nernst-Einstein deviation parameter Δ_NE and the ionicity I_W according to Walden plot are given in Table S9. The reciprocal Haven ratio is almost independent of temperature, i.e. the values obtained from diffusion coefficients at 75 °C are comparable to values obtained at ambient temperature.[73] The ionicity I_W follows the same trend as log(*C*) and suggests that deviations from the "ideal" KCl line are significant compared to other ionic liquids.[70,74–76] It is assumed that samples near to the "ideal" KCl line possess an insignificant aggregation, but the I_W values should be interpreted with caution.[77] The ionic liquids from this work show low I_W values, thus a high degree of ion aggregation when interpreted by ionicity and compared to other ILs. These ionic liquids may be viewed upon as "poor"[78] or less suitable for applications where high conductivities are needed, but quite advantageous for their use as coating materials. With high amount of aggregation or ion-pairing properties according to reciprocal Haven ratio H_R^{-1} and ionicity I_W, one may argue that the polarity of ionic liquids also declines due to lowered overall charges as a result of the aggregation. As a result, the ILs may cover the nonpolar carbon substrates in a favorable way for coating procedures, thus achieving uniform and homogeneous formation of coating consisting of PCC after pyrolysis. Taking this correlation and context into consideration, the "poor" ionicity of the investigated ionic liquids seems desirable for the utilization in the coating procedures in this work.

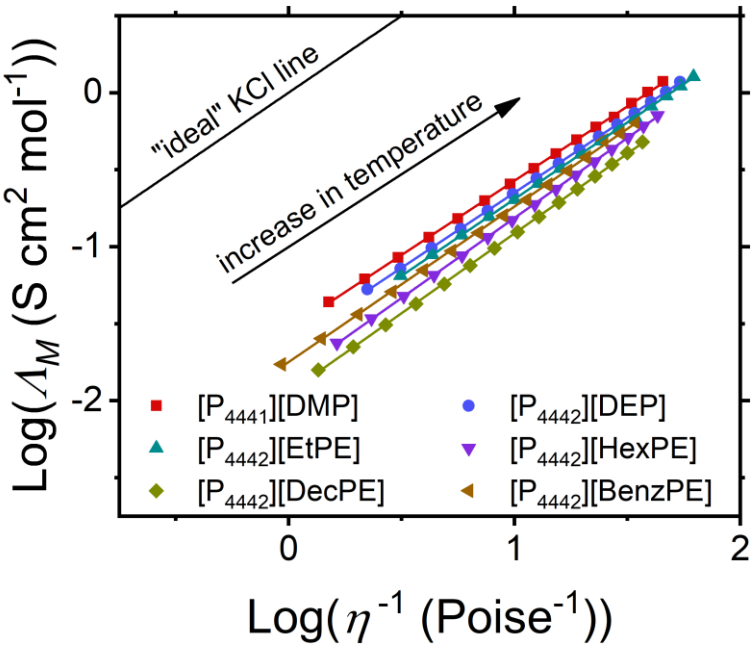

Figure S15. Walden plots of investigated ionic liquids; drawn lines are the linear fits according to Walden Equation (4). The temperature of the data points increases from left to right.

Table S8. Fitting parameters α, log (*C*) and R^2 for Walden plot.

Ionic liquid	α	$\log(C)$ (S cm^2 mol^{-1})	R^2
[P_{4441}][DMP]	0.97	−1.54	0.99987
[P_{4442}][DEP]	0.98	−1.62	0.99996
[P_{4442}][EtPE]	1.00	−1.69	0.99996
[P_{4442}][HexPE]	1.04	−1.85	0.99993
[P_{4442}][DecPE]	1.04	−1.95	0.99985
[P_{4442}][BenzPE]	1.01	−1.75	0.99945

Contrary to the macroscopic properties of viscosity and conductivity, the self-diffusion coefficients give information about the individual ions on microscopic scale. Table S9 shows the self-diffusion coefficients at 75 °C, where D_{S+} is the self-diffusion coefficient of the cation and D_{S-} the self-diffusion coefficient of the anion. Measurements at higher T were carried out to avoid experimental limitations for the samples of higher viscosity. For all the ionic liquids, the self-diffusion coefficients of the cations are smaller than the ones of the anions. The phosphate-anion based ILs [P_{4441}][DMP] and [P_{4442}][DEP] show high self-diffusion coefficients, with the latter showing the higher coefficients as it is to be expected from the viscosity and conductivity results due to the interrelations of the transport properties (Equation (4)). These two ionic liquids suggest that longer alkyl chains could be beneficial for the transport properties of ionic liquids with phosphate-based anions. Clearer trends are observed for ionic liquids with phosphonate-based anions. Shorter alkyl chains directly bonded to phosphorus in the phosphonate anions are leading to an increase of the self-diffusion coefficients. The ionic liquid which possesses the shortest alkyl chain, [P_{4442}][EtPE], shows the highest self-diffusion coefficients for both anion and cation. With extension of the alkyl chain length to hexyl- and

decyl-, the self-diffusion coefficients decrease considerably. Among all investigated ionic liquids [P_{4442}][EtPE] shows the highest self-diffusion coefficients. The trend of the diffusion coefficients is in in exceptionally good accordance with the results from rheological investigation and conductivity measurements. Again, [P_{4442}][EtPE] exhibits the best transport properties among all investigated ILs. The values obtained from the Walden-Plot suggest low ionicity and therefore high ion aggregation resulting in clustering of ions. The presented ionic liquids may not be favourable for applications where fast dynamics are required, such as reaction media or electrolyte in batteries. Nevertheless, they are more suitable for other utilizations, such as lubrication or coating. The investigated ionic liquids may be suitable phosphorus sources for the coating of nonpolar carbon surfaces, thus creating P-containing carbon layers after pyrolysis.

Table S9. Self-diffusion coefficients of the ionic liquids at 75 °C with the reciprocal Haven ratio H_R^{-1}, the Nernst-Einstein deviation parameter Δ_{NE} and the ionicity I_W according to Walden plot.

Ionic liquid	D_{S+} (10^{-7} cm² s^{-1})	D_{S-} (10^{-7} cm² s^{-1})	D_{S+}/D_{S-}	H_R^{-1}	Δ_{NE}	I_W
[P_{4441}][DMP]	2.65	3.17	0.84	0.32	0.68	0.26
[P_{4442}][DEP]	3.04	3.36	0.91	0.30	0.70	0.22
[P_{4442}][EtPE]	3.33	3.71	0.90	0.31	0.69	0.20
[P_{4442}][HexPE]	1.96	2.33	0.84	0.26	0.74	0.16
[P_{4442}][DecPE]	1.54	1.60	0.96	0.24	0.77	0.13
[P_{4442}][BenzPE]	1.47	1.62	0.91	0.40	0.60	0.23

Syntheses of the alkyl phosphonic acid diethyl esters were performed by Arbuzov reaction following the literature protocol using triethyl-phosphite and the corresponding alkyl bromide [79]. In brief, 1.0 eq. tri-ethyl-phosphite and 1.1 eq. of the respective alkyl bromide were placed in a 250 mL flask with column and distillation bridge. The reaction was carried out at a temperature range between 80 °C and 165°C with stirring and under N_2 atmosphere for approximately one day until no further ethyl bromide was distilled off. The products were purified by fractioned distillation under vacuum.

Syntheses of phosphonium ionic liquids were performed by one pot synthesis as already described in the literature.[35] 1.0 eq. of tri-*n*-butyl-phosphine with 1.2 eq. of the respective trialkyl-phosphate or alkyl-phosphonic acid diethyl ester were placed in a flask, stirred and heated to a temperature range between 135 °C and 200 °C under N_2 atmosphere. The phosphine conversion was monitored by ^{31}P-NMR. After completion of the reaction, the products were purified by liquid extraction (pentane, diethylether and dichloromethane) and vacuum distillation.

The identity and the purity of the ionic liquids and Arbuzov intermediates as well as the reaction turnover were confirmed by multinuclear NMR spectroscopy (^{1}H, ^{13}C and ^{31}P) with an AVANCE II 400 NMR spectrometer (Brucker, Billerica, USA). Before each physicochemical measurement, the samples were dried in high vacuum at 50 °C for 24 h and handled using

Schlenk techniques. Temperature dependent values for the molar conductivity and the viscosity were fitted with the Vogel-Fulcher-Tammann (VFT) equation (1).[80,81] It is reported in the literature that this equation is suitable for IL transport properties, since deviations from Arrhenius type behaviours are found for the fragile glass formers.[73,82,83]

$$Y = Y_0 \cdot \exp\left(\frac{B}{T - T_0}\right) \quad (6)$$

In equation (6), Y can either be the dynamic viscosity η or the molar conductivity Λ_M, while Y_0, B and T_0 (Vogel temperature) are material dependent parameters as follows: $B > 0$ for η, $B < 0$ for Λ_M.

4. Supplementary data to ionic liquids

Ionic liquids with different structures were synthesized, as it can be seen in Figure S1. Phosphonium ionic liquids based on $[P_{444X}]^+$ with dialkylphosphate and dialkylphosphonate anions are liquids at ambient temperature in contrast to some $[P_{111X}]^+$ or $[P_{222X}]^+$ based phosphonium ionic liquids. For example, $[P_{2221}]$[DMP] has a melting point of around 89 °C to 90 °C.[84] Moreover, tri-*n*-butyl-alkyl-phosphonium cations paired with dialkylphosphate or dialkylphosphonate anions yield a satisfying amount of phosphorus to produce P-containing carbons by coating methods. All data errors or ionic liquids are relatively small and would not visually appear in the graphs. The data points would overshadow the errors.

4.1 Thermal investigation

The procedure of solidification and liquefaction of the ionic liquids were investigated by differential scanning calorimetry (DSC) on a DSC 1 STARe System (Mettler Toledo, Gießen, Germany) equipped with a liquid nitrogen cooling system. For each measurement, vacuum dried samples of about 10 mg were sealed in aluminium crucibles inside a glove box. In the beginning of each measurement, the samples were heated with a rate of 10 °C min^{-1} to 125 °C to remove thermal history. In the following step, the samples were cooled to −120 °C with a rate of −1 °C min^{-1}, followed by 10 minutes of isothermal treatment. In the last step, the samples were subsequently heated to 100 °C with +1 °C min^{-1}. The thermal decomposition was investigated by thermal gravimetric analysis (TGA) using a NETZSCH TG 209F1 Iris. Measurements were conducted in Al_2O_3 crucibles from 25 to 900 °C with a heating rate of 20 °C min^{-1} under nitrogen flow (20 mL min^{-1}).

4.2 Density

The densities of the synthesized ionic liquids were measured with a Reischauer-type pycnometer (Neubert Glas, Geschwenda, Germany) of 5 mL nominal volume. Octane and purified water were used for volume calibration in the temperature range. For each measurement, the ionic liquid was carefully placed in the pycnometer using a cannula at room

temperature until the liquid was slightly above the mark. In the following step, the pycnometer was sealed and placed in a thermostat bath (Proline RP 1845, thermostat with max. temperature deviation ± 0.01 °C) at 25 °C. The temperature was allowed to equilibrate at the set temperature for at least 20 minutes and the liquid level was adjusted to the mark using cannulas. Afterwards the pycnometer was cooled down to room temperature and weighed. This procedure was repeated in 10 °C steps up to 95 °C.

Experimental values for the temperature-dependent densities of investigated ionic liquids are displayed in Table S10 and the respective plots are demonstrated in Figure S16. The densities of each ionic liquid show highly linear behaviours. Densities were fitted using the linear equation (7). The obtained fitting parameters are given in Table S11.

$$\rho = m\,T + b \text{ (with } T \text{ in °C)} \quad (7)$$

Table S10. Densities ρ in g mL^{-1} of the investigated ionic liquids at respective temperatures.

Temperature (°C)	Ionic liquid					
	[P_{4441}] [DMP]	[P_{4442}] [DEP]	[P_{4442}] [EtPE]	[P_{4442}] [HexPE]	[P_{4442}] [DecPE]	[P_{4442}] [BenzPE]
25	1.023	1.007	0.991	0.959	0.949	1.028
35	1.024	1.000	0.985	0.953	0.942	1.021
45	1.018	0.995	0.979	0.947	0.935	1.015
55	1.013	0.988	0.973	0.941	0.929	1.009
65	1.006	0.982	0.967	0.934	0.923	1.002
75	1.000	0.975	0.961	0.929	0.916	0.996
85	0.995	0.969	0.955	0.922	0.910	0.990
95	0.989	0.962	0.949	0.917	0.903	0.984

Table S11. Fitting parameters m, b and R^2 for the linear regression of ionic liquids densities.

Ionic liquid	m (10^{-4} K^{-1})	$\Delta m/m$ (%)	b / (g mL^{-1})	$\Delta b/b$ (%)	R^2
[P_{4441}][DMP]	−5.87	−0.38	1.05	13.7	0.9999
[P_{4442}][DEP]	−6.34	−0.95	1.02	0.04	0.9995
[P_{4442}][EtPE]	−6.08	−0.44	1.01	0.02	0.9999
[P_{4442}][HexPE]	−6.08	−0.89	0.97	0.04	0.9995
[P_{4442}][DecPE]	−6.47	−0.31	0.97	0.01	0.9999
[P_{4442}][BenzPE]	−6.25	−0.50	1.04	0.02	0.9999

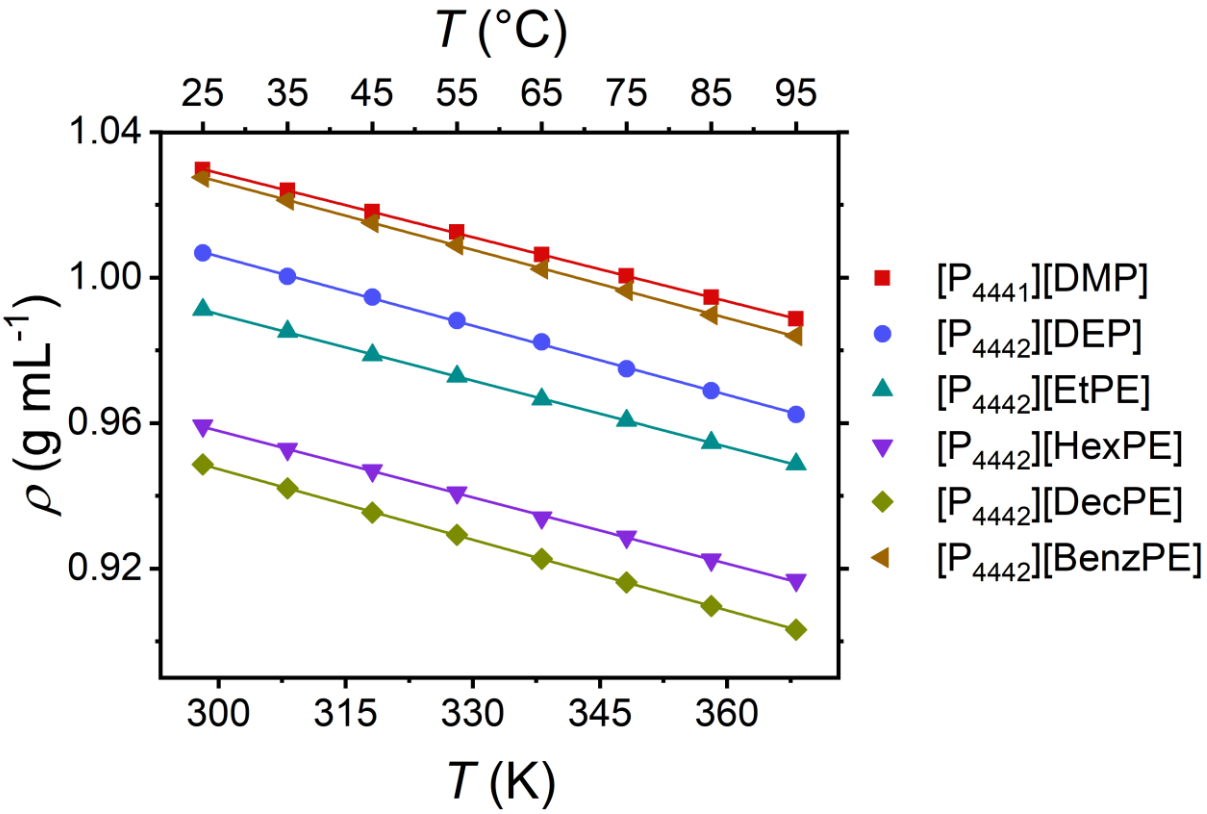

Figure S16. Density progression of the investigated ionic liquids with temperatures in K and °C. The lines are linear regression of density values.

4.3 Dynamic viscosity

The rheological investigations (shear- and temperature dependent flow properties) were conducted on a MCR 501 Rheometer (Anton Paar, Graz, Austria) with cone-plate geometry using a CP50-1 cone (diameter: 50 mm, cone angle 1 °) and Peltier controlled temperature unit. All viscosity measurements were carried out under inert gas to avoid moisture uptake from atmosphere. Before each measurement, the temperature of the sample was equilibrated for at least 10 minutes to ensure thermal stability (maximum derivation of ± 0.001 °C). The rheological data were obtained in the temperature range from 25 to 105 °C in 5 °C steps. Shear rates were varied from 25 s^{-1} to 100 s^{-1} in linear steps collecting overall 30 data points for each temperature. All ionic liquids showed purely Newtonian flow behaviour in the investigated shear rate interval. Therefore, the viscosity values for each temperature were averaged.

The experimental values for dynamic viscosity of investigated ionic liquids at respective temperatures are given in Table S12. The corresponding data were fitted according to equation (8), resulting in the VFT fitting parameters η_0, B and T_0 are displayed in Table S13.

$$\eta = \eta_0 \cdot \exp\left(\frac{B}{T - T_0}\right) \quad (8)$$

Table S12. Viscosity η in mPa s of the investigated ionic liquids at respective temperatures.

Temperature (°C)	Ionic liquid					
	$[P_{4441}]$ [DMP]	$[P_{4442}]$ [DEP]	$[P_{4442}]$ [EtPE]	$[P_{4442}]$ [HexPE]	$[P_{4442}]$ [DecPE]	$[P_{4442}]$ [BenzPE]
25	663.4	448.6	319.2	611.6	738.4	1076.7
30	460.0	319.4	231.3	429.3	517.4	716.4
35	327.8	232.7	171.4	308.8	371.8	492.2
40	238.9	172.9	129.6	227.1	273.1	347.9
45	178.0	131.4	99.97	170.7	204.5	252.9
50	135.4	101.6	78.59	131.3	157.2	189.1
55	104.5	79.78	62.74	102.4	122.5	144.0
60	81.95	63.70	50.77	81.24	96.90	111.6
65	65.54	51.50	41.62	65.46	77.88	88.12
70	53.02	42.27	34.66	53.55	63.60	71.05
75	43.63	35.10	29.19	44.19	52.66	58.02
80	36.17	29.39	24.81	37.05	43.93	47.99
85	30.28	24.88	21.23	31.36	36.96	40.16
90	25.71	21.36	18.42	26.88	31.62	34.03
95	21.97	18.50	16.11	23.27	27.09	29.25
100	19.00	16.11	14.23	20.23	23.47	25.41
105	16.47	14.10	12.65	17.79	20.54	22.16

Table S13. VFT fitting parameters η_0, B, T_0 and R^2 for the viscosity η of the investigated ionic liquids.

Ionic liquid	η_0 (10^{-1}mPa s)	$\Delta\eta_0/\eta_0$ (%)	B (K)	$\Delta B/B$ (%)	T_0 (K)	$\Delta T_0/T_0$ (%)	R^2
$[P_{4441}]$[DMP]	0.49	4.48	1188	1.06	173.4	0.42	>0.99999
$[P_{4442}]$[DEP]	0.54	5.65	1145	1.40	171.2	0.58	>0.99999
$[P_{4442}]$[EtPE]	0.88	5.24	994.6	1.45	176.8	0.56	>0.99999
$[P_{4442}]$[HexPE]	0.78	6.60	1083	1.65	177.4	0.63	>0.99999
$[P_{4442}]$[DecPE]	0.80	5.76	1121	1.41	175.5	0.55	>0.99999
$[P_{4442}]$[BenzPE]	1.12	6.06	980.9	1.48	191.2	0.46	>0.99999

4.4 Specific conductivity

The specific conductivities of the synthesized ionic liquids were measured by means of impedance spectroscopy in a closed electrochemical cell using a SP-150 potentiostat (BioLogic, Seysinnet-Pariset, France) and a conductivity probe (WTW, Weilheim, Germany). The probe consisted of two platinized platinum electrodes of rectangular geometry fixed in glass with a nominal cell constant of 0.5 cm^{-1}. The actual cell constant was determined using commercial standards. The temperature of the heating bath was controlled with a thermostat (maximum deviation of ±0.01 °C). Prior to each measurement, the temperature was allowed to equilibrate for at least 30 minutes. The conductivity values were measured in 10 °C steps from 25 °C to 95 °C. The impedance spectra were recorded at applied voltage amplitudes of 5, 10 and 15 mV and frequencies from 200 kHz to 1 Hz in 50 logarithmic steps. The resistances used for the calculation of the specific conductivity κ were averaged with deviations of max. ± 1.0% from voltage amplitude data. Taking the specific conductivity and the density into account, the molar conductivities can be calculated according to equation (9).

$$\Lambda_M = \frac{\kappa}{c} = \frac{\kappa \cdot M}{\rho} \tag{9}$$

with M the molar mass and ρ the density of the ionic liquids. The uncertainty of the specific conductivity is around ±2 % as estimated by commercial conductivity standards.

The experimental data of the specific conductivity κ obtained from measurements are given in

Table S14 and the plots with VFT fitting are demonstrated in Figure S17. The experimental data were fitted according to equation (10) resulting in the VFT fitting parameters κ_0, B and T_0 that are displayed in Table S15.

$$\kappa = \kappa_0 \cdot \exp\left(\frac{B}{T - T_0}\right) \quad (10)$$

Table S14. Specific conductivity κ in µS cm^{-1} of the investigated ionic liquids at respective temperatures.

Temperature (°C)	Ionic liquid					
	[P_{4441}] [DMP]	[P_{4442}] [DEP]	[P_{4442}] [EtPE]	[P_{4442}] [HexPE]	[P_{4442}] [DecPE]	[P_{4442}] [BenzPE]
25	132	138	174	50	29	41
30	185	188	238	72	42	61
35	255	255	318	100	58	87
40	343	339	417	137	78	121
45	453	442	537	183	105	166
50	588	565	681	239	138	221
55	753	714	851	308	178	290
60	949	888	1047	389	226	373
65	1181	1091	1274	486	283	471
70	1446	1322	1525	599	350	588
75	1750	1579	1809	730	426	724
80	2024	1866	2123	878	513	881
85	2476	2190	2467	1045	613	1129
90	2916	2542	2850	1232	724	1259
95	3408	2937	3268	1437	849	1480

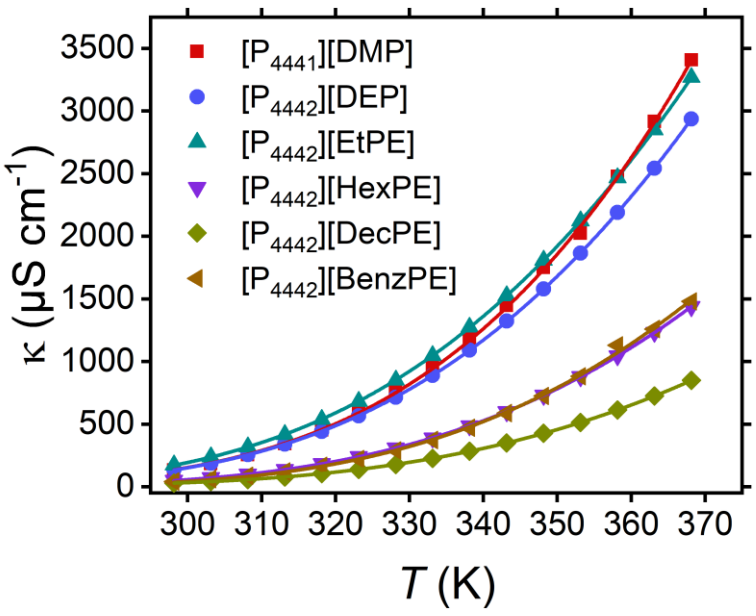

Figure S17. Progression of the specific conductivity κ of the investigated ionic liquids with temperature in K.

Table S15. VFT fitting parameters κ_0, B, T_0 and R^2 for the specific conductivity κ of the investigated ionic liquids.

Ionic liquid	κ_0 (S cm^{-1})	$\Delta\kappa_0/\kappa_0$ (%)	B (K)	$\Delta B/B$ (%)	T_0 (K)	$\Delta T_0/T_0$ (%)	R^2
[P_{4441}][DMP]	1.81	42.31	−1294.7	−12.0	111.2	9.89	0.99971
[P_{4442}][DEP]	0.56	52.43	−988.8	−1.75	93.70	1.49	0.99999
[P_{4442}][EtPE]	0.48	3.62	−937.2	−1.27	93.20	1.11	>0.99999
[P_{4442}][HexPE]	0.45	4.74	−1087.0	−1.46	94.25	1.28	0.99999
[P_{4442}][DecPE]	0.34	4.53	−1158.2	−1.34	98.47	1.17	>0.99999
[P_{4442}][BenzPE]	0.31	73.99	−906.1	−24.0	75.27	23.6	0.99843

4.5 Molar conductivity

The molar conductivity of the investigated ionic liquids was calculated according to equation (11) and presented in

Table S16. The experimental data were fitted according to equation (12), resulting in the VFT fitting parameters κ_0, B and T_0 that are listed in Table S17.

$$\Lambda_{\mathrm{M}} = \frac{\kappa M}{\rho} \tag{11}$$

$$\Lambda = \Lambda_{\mathrm{M}} \cdot \exp\left(\frac{B}{T - T_0}\right) \tag{12}$$

Table S16. Molar conductivity Λ_M in mS cm^2 mol^{-1} of the investigated ionic liquids at respective temperatures.

Temperature (°C)	Ionic liquid					
	[P_{4441}] [DMP]	[P_{4442}] [DEP]	[P_{4442}] [EtPE]	[P_{4442}] [HexPE]	[P_{4442}] [DecPE]	[P_{4442}] [BenzPE]
25	43.86	52.77	64.82	23.71	15.84	17.19
30	61.78	72.16	88.67	34.05	22.39	25.33
35	85.24	98.06	118.96	47.71	31.11	36.41
40	115.1	130.6	156.6	65.26	42.53	50.99
45	152.4	170.8	202.0	87.49	57.10	70.28
50	198.5	219.2	257.0	114.9	75.37	93.70
55	254.6	277.9	322.2	148.6	97.57	123.1
60	322.0	346.6	397.9	188.3	124.4	158.9
65	401.9	426.8	485.7	236.1	156.1	201.6
70	493.6	519.6	583.2	291.6	193.9	252.2
75	598.9	622.6	693.6	356.3	236.9	311.2
80	694.7	738.0	816.8	430.4	286.6	379.9
85	852.4	869.1	952.3	513.9	343.3	489.0
90	1007	1012	1103	607.5	407.2	546.5
95	1180	1173	1269	711.0	478.8	644.7

Table S17. VFT fitting parameters $\Lambda_{M,0}$, B, T_0 and R² for the specific conductivity *κ* of the ionic liquids.

Ionic liquid	$\Lambda_{M,0}$ (S cm^{-1})	$\Delta\Lambda_{M,0}/\Lambda_{M,0}$ (%)	B (K)	$\Delta B/B$ (%)	T_0 (K)	ΔT_0 (%)	R^2
[P_{4441}][DMP]	523.0	12.07	−1215	−3.54	168.9	1.86	0.99999
[P_{4442}][DEP]	280.5	6.71	−1054	−2.17	175.7	1.04	>0.99999
[P_{4442}][EtPE]	225.0	6.59	−990.6	−2.24	176.8	1.06	>0.99999
[P_{4442}][HexPE]	262.8	5.87	−1130	−1.77	177.1	0.85	>0.99999
[P_{4442}][DecPE]	238.7	5.96	−1219	−1.72	171.8	0.88	>0.99999
[P_{4442}][BenzPE]	84.88	112.3	−767.0	−40.3	210.6	13.0	0.99827

4.6 Walden plot

The correlation of the transport properties were conducted using Walden (equation (13)) and Nernst-Einstein (equation (14)) relations. The relation of molar conductivity to fluidity was investigated using fractional Walden approach[71,74], where the additional parameter α is a value close to unity for both ionic and molecular liquids.

$$\Lambda_{\mathrm{M}} \propto \left(\frac{1}{\eta}\right)^{\mathrm{t}}$$

$$\log\left(\frac{\Lambda_M \text{ mol}}{\text{S cm}^2}\right) = \log(C) + \alpha \log\left(\frac{0.1 \text{ Pa s}}{\eta}\right) \tag{13}$$

$$\Lambda_{\mathrm{NE}} = \left(\frac{F^2}{R\,T}\right)\sum_i z_i^2\, D_{Si} \tag{14}$$

In these relations, Λ_{M} is the molar conductivity obtained from the corresponding experiment, η is the viscosity, and Λ_{NE} the molar conductivity calculated by the Nernst-Einstein equation. Additionally, F is the Faraday constant, R the gas constant, T the absolute temperature and z_i the charge number of the particular ion, which is ±1 for all ions in this work. Both relations are established in the literature to quantify deviations from ideally behaving electrolytes.[74,75,78] The ionicity I_{W} was obtained by equation (15) and represents the vertical difference of the measured conductivity data in relation to the "ideal" KCl-line.[75]

$$I_{\mathrm{W}}(T) = \frac{\Lambda_M}{\Lambda_M^0} = \frac{\Lambda_M^{\exp}(T)\ \text{mol}}{\text{S cm}^2} \times \frac{\eta^{\exp}(T)}{0.1\ \text{Pa s}} \tag{15}$$

In addition, the reciprocal Haven ratio I_{HR} can be calculated with equation (16) for the purpose of quantifying assumptions on ion aggregation; it describes the amount of dissociated/unpaired ions similar to Λ_{NE}.[70,85]

$$I_{\mathrm{HR}} = \frac{\Lambda_M}{\Lambda_{\mathrm{NE}}} = {H_{\mathrm{R}}}^{-1}$$

$$\Lambda_{\mathrm{NE}} = 1 - {H_{\mathrm{R}}}^{-1} \tag{16}$$

The Walden plot was determined by plotting the logarithm of the molar conductivity Λ_M against the logarithm of the reciprocal viscosity η^{-1} at respective temperatures. The values for Walden plot are displayed in

Table S18 and

Table S19. Linear fitting of Walden plot was carried out using equation (17), with resulting parameters of linear regression given in Table **S20**.

$$\log\left(\frac{\Lambda_{\mathrm{M}}\ \mathrm{mol}}{\mathrm{S\ cm^2}}\right) = \alpha\ \log\left(\frac{0.1\ \mathrm{Pa\ s}}{\eta}\right) + \log(C) \qquad (17)$$

Table S18. Calculated values of log (η^{-1} / Poise^{-1}) and log (Λ_M / S cm^2 mol^{-1}) for ionic liquids [P_{4441}][DMP], [P_{4442}][DEP] and [P_{4442}][EtPE].

Temperature (°C)	[P_{4441}][DMP]		[P_{4442}][DEP]		[P_{4442}][EtPE]	
	log (η^{-1} / Poise^{-1})	log (Λ_M / S cm^2 mol^{-1})	log (η^{-1} / Poise^{-1})	log (Λ_M / S cm^2 mol^{-1})	log (η^{-1} / Poise^{-1})	log (Λ_M / S cm^2 mol^{-1})
25	0.178	−1.358	0.348	−1.278	0.496	−1.188
30	0.337	−1.209	0.496	−1.142	0.636	−1.052
35	0.484	−1.069	0.633	−1.009	0.766	−0.925
40	0.622	−0.939	0.762	−0.884	0.887	−0.805
45	0.750	−0.817	0.882	−0.768	1.000	−0.695
50	0.868	−0.702	0.993	−0.659	1.105	−0.590
55	0.981	−0.594	1.098	−0.556	1.203	−0.492
60	1.087	−0.492	1.196	−0.460	1.294	−0.400
65	1.184	−0.396	1.288	−0.340	1.381	−0.314
70	1.276	−0.307	1.374	−0.284	1.460	−0.234
75	1.360	−0.223	1.455	−0.206	1.535	−0.159
80	1.442	−0.158	1.532	−0.132	1.605	−0.088
85	1.519	−0.069	1.604	−0.061	1.673	−0.021
90	1.590	0.003	1.670	0.005	1.735	0.043
95	1.658	0.072	1.733	0.069	1.793	0.104

Table S19. Calculated values of log (η^{-1} / Poise^{-1}) and log (Λ_M / S cm^2 mol^{-1}) for ionic liquids [P_{4442}][HexPE], [P_{4442}][DecPE] and [P_{4442}][BenzPE].

Temperature (°C)	[P_{4442}][HexPE]		[P_{4442}][DecPE]		[P_{4442}][BenzPE]	
	log (η^{-1} / Poise^{-1})	log (Λ_M / S cm^2 mol^{-1})	log (η^{-1} / Poise^{-1})	log (Λ_M / S cm^2 mol^{-1})	log (η^{-1} / Poise^{-1})	log (Λ_M / S cm^2 mol^{-1})
25	0.214	−1.625	0.132	−1.800	−0.032	−1.765
30	0.367	−1.468	0.286	−1.650	0.145	−1.596
35	0.510	−1.321	0.430	−1.507	0.308	−1.439
40	0.644	−1.185	0.564	−1.371	0.459	−1.293
45	0.768	−1.058	0.689	−1.243	0.597	−1.153
50	0.882	−0.940	0.804	−1.123	0.723	−1.028
55	0.990	−0.828	0.912	−1.011	0.842	−0.910
60	1.090	−0.725	1.014	−0.905	0.952	−0.799
65	1.184	−0.627	1.109	−0.807	1.055	−0.696
70	1.271	−0.535	1.197	−0.713	1.148	−0.598
75	1.355	−0.449	1.279	−0.626	1.236	−0.507
80	1.431	−0.366	1.357	−0.543	1.319	−0.420
85	1.504	−0.289	1.432	−0.464	1.396	−0.311
90	1.571	−0.217	1.500	−0.390	1.468	−0.262
95	1.633	−0.148	1.567	−0.320	1.534	−0.191

Table S20. Fitting parameters α, log (*C*) and R^2 for Walden plot.

Ionic liquid	α	Δα/α (%)	log(*C*) (S cm^2 mol^{-1})	Δlog(*C*)/ log(*C*) (%)	R^2
[P_{4441}][DMP]	0.965	0.315	−1.537	−0.224	0.99987
[P_{4442}][DEP]	0.975	0.182	−1.625	−0.132	0.99996
[P_{4442}][EtPE]	0.996	0.177	−1.688	−0.136	0.99996
[P_{4442}][HexPE]	1.039	0.238	−1.853	−0.149	0.99993
[P_{4442}][DecPE]	1.036	0.342	−1.950	−0.190	0.99985
[P_{4442}][BenzPE]	1.010	0.649	−1.750	−0.375	0.99945

4.7 Self-diffusion coefficients

The self-diffusion coefficients were determined using a PFGSTE NMR according to the literature.[70] The NMR spectra of the ionic liquids were recorded in flame-sealed inserts of coaxial NMR tubes (to avoid uptake of moisture and minimize convection effects) on an AVANCE II 400 NMR spectrometer (Brucker, Billerica, USA) with 5 mm BBFO probe. The magnetic field gradient was calibrated using purified water. The self-diffusion coefficients were determined using the ^{1}H nucleus for both cation and anion but different peaks which was possible due to the different chemical shifts. In each measurement the temperature was allowed to equilibrate for at least 1 hour. Further details on how measurements and

coefficient determination were performed can be read in an already reported work of Rauber and Philippi[70]. Plotting $ln(I/I_0)$ versus Q following the Stejskal-Tanner equation[86–88] (equation (18)) results in the self-diffusion coefficient D_{Si} as the slope of the resulting straight line.

$$ln\left(\frac{I}{I_0}\right) = D_{Si}\,\gamma^2\,\delta^2\,g^2\left(\Delta - \frac{\delta}{3} - \frac{\tau}{2}\right) = D_{Si}\,Q \qquad (18)$$

In equation (3), I is the signal intensity with applied gradient, I_0 the initial signal intensity, γ the gyromagnetic ratio of the investigated nucleus, δ the overall gradient duration, g the applied gradient strength, Δ the diffusion time, and τ the gradient interspacing. The estimated uncertainty for the self-diffusion coefficients is ±5 %.

Additional experimental details on how PFGSTE measurements were calibrated and conducted can be found in a previous work of Rauber and Philippi.[70] The parameters of the PFGSTE-measurements for the investigated ionic liquids are exhibited in Table S21. All measurements were carried out at 75 °C and the corresponding parameters varied for each ionic liquid and their respective ion.

Table S21. Parameters used for PFGSTE measurements on the ionic liquids at 75 °C from ^{1}H NMR; a) values for cation, b) values for anion.

Ionic liquid	^{1}H			
	p30 (ms)	d20 (ms)	p1 (µs)	d1 (s)
[P_{4441}][DMP]	5.40	120	11.18	7.052
[P_{4442}][DEP]	5.06	120	11.63	7.752
[P_{4442}][EtPE]	4.82[a] / 4.53[b]	120	11.81	7.752
[P_{4442}][HexPE]	6.06	130	11.79	7.052
[P_{4442}][DecPE]	6.50	140	11.62	7.752
[P_{4442}][BenzPE]	6.73[a] / 6.43[b]	140	11.42	7.752

5. Synthesis and identification of phosphonates and ionic liquids

Table S22. List of used chemicals and their purity grade and respective supplier.

Chemical	Purity grade	Supplier
1-Bromodecane	98 %	Sigma-Aldrich, USA
1-Bromohexane	99 %	Alfa Aesar, Germany
Benzyl bromide	98 %	Alfa Aesar, Germany
Carbon black Vulcan-XC72R	-/-	FuelCellStore
Carbon nano tubes (multi walled)	-/-	Graphene Supermarket
Ethyl iodide	98 %	Fisher scientific
Ethylene glycol	99 %, technical grade	Grüssing, Germany
Hexachloroplatinic acid	40 wt.-% platinum	Umicore, Germany
Isopropyl alcohol	97 %	Biesterfeld Spezialchemie GmbH, Germany
Nafion 117 solution	~ 5 %	Sigma-Aldrich, USA
Tri-ethyl phosphate	99.8 %	Sigma-Aldrich, USA
Tri-ethyl phosphite	98 %	Alfa Aesar, Germany
Tri-methyl phosphate	97 %	Sigma-Aldrich, USA
Tri-n-butyl phosphine	99 %	Strem Chemicals, Germany
Water	HPLC grade	Fisher Scientific

5.1 Ethyl phosphonic acid diethyl ester

700 mmol (116.31 g / 112.71 mL) tri-ethyl phosphite and 140 mmol ethyl iodide (21.84 g / 42.36 mL) were stirred and heated to 85 °C under reflux. After 48 hours no change in phosphite turnover was measured. The product was obtained by fractional distillation at 90 °C and pressure of 5-15 mbar as a clear liquid with a yield of 90.00 g (86.8 % of theory).

^{1}H NMR ($CDCl_3$, 400 MHz, δ in ppm) 3.96 – 3.79 (m, 4H, P-O-***CH_2***-CH_3), 1.51 (dq, J = 18.2 Hz, J = 7.7 Hz, 2H, P-***CH_2***-CH_3), 1.10 (t, J = 7.1 Hz, 6H, P-O-CH_2-***CH_3***), 0.93 (dt, J = 19.9, J = 7.7 Hz, 3H, P-CH_2-***CH_3***).

^{13}C{^{1}H} NMR (DMSO-*d_6*, 101 MHz, δ in ppm) 61.13 (d, J = 6.3 Hz, P-O-***CH_2***-CH_3), 18.76 (d, J = 142.6 Hz, P-***CH_2***-CH_3) 16.36 (d, J = 5.7 Hz, P-O-CH_2-***CH_3***), 6.46 (d, J = 6.8 Hz, P-CH_2-***CH_3***).

^{31}P{^{1}H} NMR ($CDCl_3$, 162 MHz, δ in ppm) 33.24 (s).

5.2 Hexyl phosphonic acid diethyl ester

300 mmol (49.85 g / 48.30 mL) tri-ethyl phosphite and 315 mmol hexyl bromide (52.00 g / 61.36 mL) were stirred and heated to 165 °C under reflux. After 48 hours no change in phosphite turnover was measured. The product was obtained by fractional distillation at 130 °C and a pressure of 6 mbar as a clear liquid with a yield of 23.00 g (34.5 % of theory).

^{1}H NMR ($CDCl_3$, 400 MHz, δ in ppm) 4.18 – 3.86 (m, 4H, P-O-***CH₂***-CH_3), 1.73 – 1.58 (m, 2H, P-***CH₂***-$(CH_2)_4$-CH_3), 1.59 – 1.42 (m, P-CH_2-***CH₂***-$(CH_2)_3$-CH_3), 1.35 – 1.17 (m, 12H, P-$(CH_2)_2$-***CH₂-CH₂-CH₂***-CH_3, P-O-CH_2-***CH₃***), 0.82 (t, J = 6.8 Hz, P-$(CH_2)_5$-***CH₃***).

^{13}C{^{1}H} NMR (DMSO-*d₆*, 101 MHz, δ in ppm) 61.09 (d, J = 6.3 Hz, P-O-***CH₂***-CH_3), 31.64 (s, P-***CH₂***-$(CH_2)_4$-CH_3), 30.43 (d, J = 16.1 Hz, P-$(CH_2)_3$-***CH₂***-CH_2-CH_3), 25.67 (d, J = 140.3 Hz, P-$(CH_2)_2$-***CH₂***-$(CH_2)_2$-CH_3), 22.81 (d, J = 5.1 Hz, P-CH_2-***CH₂***-$(CH_2)_3$-CH_3), 22.68 (s, P-$(CH_2)_4$-***CH₂***-CH_3), 16.36 (d, J = 5.8 Hz, P-O-CH_2-***CH₃***), 13.84 (s, P-$(CH_2)_5$-***CH₃***).

^{31}P{^{1}H} NMR ($CDCl_3$, 162 MHz, δ in ppm) 32.52 (tt, J = 17.1 Hz, J = 8.5 Hz).

5.3 Decyl phosphonic acid diethyl ester

300 mmol (49.85 g / 48.30 mL) tri-ethyl phosphite and 315 mmol decyl bromide (69.68 g / 74.28 mL) were stirred and heated to 165 °C under reflux. After 48 hours no change in phosphite turnover was measured. The product was obtained by fractional distillation at 93-113 °C and a pressure of 0.15-0.3 mbar as a clear liquid with a yield of 41.35 g (49.5 % of theory).

^{1}H NMR ($CDCl_3$, 400 MHz, δ in ppm) 4.20 – 3.93 (m, 4H, P-O-***CH₂***-CH_3), 1.76 – 1.62 (m, 2H, P-***CH₂***-$(CH_2)_8$-CH_3), 1.56 (ttd, J = 15.5 Hz, J = 7.7 Hz, J = 7.2 Hz, J = 5.0 Hz, 2H, P-$(CH_2)_2$-***CH₂***-$(CH_2)_6$-CH_3), 1.40 – 1.17 (m, 18H, P-CH_2-***CH₂***-CH_2-(***CH₂***)$_6$-CH_3, P-O-CH_2-***CH₃***), 0.84 (t, J = 6.7 Hz, 1H, P-$(CH_2)_9$-***CH₃***).

^{31}P{^{1}H} NMR ($CDCl_3$, 162 MHz, δ in ppm) 32.59 (s).

5.4 Benzyl phosphonic acid diethyl ester

300 mmol (49.85 g / 48.30 mL) tri-ethyl phosphite and 315 mmol benzoyl bromide (53.88 g / 77.58 mL) were stirred and heated to 130 °C under reflux. After 48 hours no change in phosphite turnover was measured. The product was obtained by fractional distillation at 92 °C and a pressure of 0.15 mbar as a clear liquid with a yield of 32.31 g (38.7 % of theory).

^{1}H NMR ($CDCl_3$, 400 MHz, δ in ppm) 7.33 – 7.19 (m, 5H, P-CH_2-***Ph***), 4.12 – 3.94 (m, 4H, P-O-***CH₂***-CH_3), 3.15 (d, J = 21.6 Hz, 2H, P-***CH₂***-Ph), 1.23 (t, J = 7.1 Hz, 6H, P-O-CH_2-***CH₃***).

^{13}C{^{1}H} NMR (DMSO-*d₆*, 101 MHz, δ in ppm) 133.03 (d, J = 8.9 Hz, P-CH_2-***C***-$(CH)_{5,cyclo}$), 130.31 (d, J = 6.6 Hz, P-CH_2-C-***CH***-CH-CH-), 128.61 (d, J = 3.0 Hz, P-CH_2-C-CH-***CH***-CH-), 126.90 (d, J = 3.6 Hz, P-CH_2-C-CH-CH-***CH***-), 61.79 (d, J = 137 Hz, P-***CH₂***-CH_3)), 33.47, 16.27 (d, J = 5.8 Hz, P-O-CH_2-***CH₃***).

^{31}P{^{1}H} NMR ($CDCl_3$, 162 MHz, δ in ppm) 26.41 (dt, J = 21.2 Hz, J = 11.6 Hz).

5.5 Tri-*n*-butyl methyl phosphonium dimethylphosphate [P_{4441}][DMP]

58.41 mmol (11.82 g / 14.47 mL) tri-*n*-butyl phosphine were mixed with 70.10 mmol (9.82 g / 8.20 mL) trimethyl phosphate at 135 °C. Phosphine turnover remained unchanged after 42 hours. 200 mL water were added to the mixture and liquid extraction performed with three

times with 5 mL pentane, diethyl ether and dichloromethane each, respectively. The product was a colorless oil with a yield of 19.38 g (96.6 % of theory).

^{1}H NMR ($CDCl_3$, 400 MHz, δ in ppm) 3.49 (d, J = 10.4 Hz, 6H, P-O-***CH₃***), 2.41 – 2.24 (m, 6H, $^{+}$P-***CH₂***-$(CH_2)_2$-CH_3), 1.97 (d, J = 13.7 Hz, 3H, $^{+}$P-***CH₃***), 1.45 (dt, J = 7.4 Hz, J = 3.6 Hz, 12H, $^{+}$P-CH_2-***CH₂-CH₂***-CH_3), 0.91 (t, 9H, $^{+}$P-$(CH_2)_3$-***CH₃***).

^{13}C{^{1}H} NMR ($CDCl_3$, 101 MHz, δ in ppm) 52.13 (d, J = 6.0 Hz, P-O-***CH₃***), 23.73 (d, J = 15.6 Hz, $^{+}$P-CH_2-CH_2-***CH₂***-CH_3), 23.54 (d, J = 4.7 Hz, $^{+}$P-CH_2-***CH₂***-CH_2-CH_3), 19.68 (d, J = 48.9 Hz, $^{+}$P-***CH₂***-$(CH_2)_2$-CH_3), 13.36 (s, $^{+}$P-$(CH_2)_3$-***CH₃***), 4.13 (d, J = 52.2 Hz, $^{+}$P-***CH₃***).

^{31}P{^{1}H} NMR ($CDCl_3$, 162 MHz, δ in ppm) 31.97 (s, $^{+}$P), 2.07 (p, J = 11.1 Hz).

5.6 Tri-*n*-butyl ethyl phosphonium diethylphosphate [P_{4442}][DEP]

52.02 mmol (10.53 g / 12.88 mL) tri-*n*-butyl phosphine were mixed with 62.42 mmol (11.37 g / 10.61 mL) triethyl phosphate at 160 °C. Phosphine turnover remained unchanged after 48 hours. 200 mL water were added to the mixture and liquid extraction performed with three times with 5 mL pentane, diethyl ether and dichloromethane each, respectively. The product was a colorless oil with a yield of 16.76 g (83.8 % of theory).

^{1}H NMR ($CDCl_3$, 400 MHz, δ in ppm) 3.73 (p, J = 7.0 Hz, 2H, P-O-***CH₂***-CH_3), 2.34 (dq, J = 13.2, J = 7.7 Hz, 2H, $^{+}$P-***CH₂***-CH_3), 2.27 – 2.14 (m, 6H, $^{+}$P-***CH₂***-$(CH_2)_2$-CH_3), 1.34 (dq, J = 7.8 Hz, J = 4.0 Hz, 12H, $^{+}$P-CH_2-***CH₂-CH₂***-CH_3), 1.11 (t, J = 7.7 Hz, 6H, P-O-CH_2-***CH₃***), 1.05 (dt, 3H, $^{+}$P-CH_2-***CH₃***), 0.83 – 0.74 (m, 1H, $^{+}$P-$(CH_2)_3$-***CH₃***).

^{13}C{^{1}H} NMR ($CDCl_3$, 101 MHz, δ in ppm) 60.29 (d, J = 5.7 Hz, P-O-***CH₂***-CH_3), 23.81 (d, J = 15.3 Hz, $^{+}$P-CH_2-CH_2-***CH₂***-CH_3), 23.61 (d, J = 4.8 Hz, $^{+}$P-CH_2-***CH₂***-CH_2-CH_3), 18.12 (d, J = 48.4 Hz, $^{+}$P-***CH₂***-$(CH_2)_2$-CH_3), 16.55 (d, J = 7.6 Hz, P-O-CH_2-***CH₃***), 13.31 (s, $^{+}$P-$(CH_2)_3$-***CH₃***), 12.43 (d, J = 48.8 Hz, $^{+}$P-***CH₂***-CH_3), 5.97 (d, J = 5.6 Hz, $^{+}$P-CH_2-***CH₃***).

^{31}P{^{1}H} NMR ($CDCl_3$, 162 MHz, δ in ppm) 34.64 (s, $^{+}$P), -0.22 (s).

5.7 Tri-*n*-butyl ethyl phosphonium ethyl phosphonic acid ethyl ester [P_{4442}][EtPE]

54.28 mmol (10.98 g / 13.44 mL) tri-*n*-butyl phosphine were mixed with 65.13 mmol (10.82 g) ethyl phosphonic acid diethyl ester. Phosphine turnover remained unchanged after 42 hours at 160 °C and 24 hours at 170 °C. 200 mL water were added to the mixture and liquid extraction performed with three times with 5 mL pentane, diethyl ether and dichloromethane each, respectively. The product was a colorless oil with a yield of 15.40 g (77.0 % of theory).

^{1}H NMR ($CDCl_3$, 400 MHz, δ in ppm) 3.68 (p, J = 7.0 Hz, 2H, P-O-***CH₂***-CH_3), 2.34 (dq, J = 13.2 Hz, J = 7.7 Hz, 2H, $^{+}$P-***CH₂***-CH_3), 2.28 – 2.10 (m, 6H, $^{+}$P-***CH₂***-$(CH_2)_2$-CH_3), 1.43 – 1.24 (m, 14H, $^{+}$P-CH_2-***CH₂-CH₂***-CH_3, P-***CH₂***-CH_3), 1.12 – 0.98 (m, 6H, $^{+}$P-CH_2-***CH₃,*** P-O-CH_2-***CH₃***), 0.89 (dt, J = 17.5 Hz, J = 7.7 Hz, 3H, P-CH_2-***CH₃***), 0.79 – 0.72 (m, 9H, $^{+}$P-$(CH_2)_3$-***CH₃***).

^{13}C{^{1}H} NMR ($CDCl_3$, 101 MHz, δ in ppm) 59.13 (d, J = 5.4 Hz, P-O-***CH₂***-CH_3), 23.79 (d, J = 15.3 Hz, $^{+}$P-CH_2-CH_2-***CH₂***-CH_3), 23.59 (d, J = 4.8 Hz, $^{+}$P-CH_2-***CH₂***-CH_2-CH_3), 20.05 (d, J = 134.2 Hz, P-

CH₂-CH_3), 18.11 (d, J = 47.3 Hz, $^+$P-***CH₂***-$(CH_2)_2$-CH_3), 16.83 (d, J = 6.5 Hz, P-O-CH_2-***CH₃***), 13.28 (s, $^+$P-$(CH_2)_3$-***CH₃***), 12.43 (d, J = 48.7 Hz, $^+$P-***CH₂***-CH_3), 8.16 (d, J = 6.0 Hz, P-CH_2-***CH₃***), 5.95 (d, J = 5.6 Hz, $^+$P-CH_2-***CH₃***).

$^{31}P\{^1H\}$ NMR ($CDCl_3$, 162 MHz, δ in ppm) 34.61 (s, $^+$P), 24.70 (s).

5.8 Tri-*n*-butyl ethyl phosphonium hexyl phosphonic acid ethyl ester [P_{4442}][HexPE]

47.10 mmol (9.53 g / 11.67 mL) tri-*n*-butyl phosphine were mixed with 56.52 mmol (12.56 g) hexyl phosphonic acid diethyl ester at 180 °C. Phosphine turnover remained unchanged after 116 hours. 200 mL water were added to the mixture and liquid extraction performed with three times with 5 mL pentane, diethyl ether and dichloromethane each, respectively. The product was a colorless oil with a yield of 13.03 g (65.2 % of theory).

^1H NMR ($CDCl_3$, 400 MHz, δ in ppm) 3.76 (p, J = 6.9 Hz, 2H, P-O-***CH₂***-CH_3), 2.51 (dq, J = 13.3 Hz, J = 7.7 Hz, 2H, $^+$P-***CH₂***-CH_3), 2.40 – 2.28 (m, 6H, $^+$P-***CH₂***-$(CH_2)_2$-CH_3), 1.54 – 1.32 (m, 14H, $^+$P-CH_2-***CH₂***-***CH₂***-CH_3, P-***CH₂***-***CH₂***-$(CH_2)_3$-CH_3), 1.27 – 1.05 (m, 12H, $^+$P-CH_2-***CH₃***, P-O-CH_2-***CH₃***, P-$CH_2)_2$-***CH₂***-***CH₂***-***CH₂***-CH_3), 0.87 (t, 9H, $^+$P-$(CH_2)_3$-***CH₃***), 0.75 (t, J = 6.7 Hz, 3H, P-$(CH_2)_5$-***CH₃***).

$^{13}C\{^1H\}$ NMR ($CDCl_3$, 101 MHz, δ in ppm) 59.01 (d, J = 5.2 Hz, P-O-***CH₂***-CH_3), 31.70 (d, J = 1.2 Hz, P-$(CH_2)_3$-***CH₂***-CH_2-CH_3), 31.26 (d, J = 16.8 Hz, P-$(CH_2)_2$-***CH₂***-$(CH_2)_2$-CH_3), 28.16 (d, J = 131.2 Hz, P-***CH₂***-$(CH_2)_4$-CH_3), 24.60 (d, J = 4.4 Hz, P-$(CH_2)_4$-***CH₂***-CH_3), 23.93 (d, J = 15.2 Hz, $^+$P-CH_2-CH_2-***CH₂***-CH_3), 23.77 (d, J = 4.8 Hz, $^+$P-CH_2-***CH₂***-CH_2-CH_3), 22.52 (s, P-CH_2-***CH₂***-$(CH_2)_4$-CH_3), 18.25 (d, J = 47.3 Hz, $^+$P-***CH₂***-$(CH_2)_2$-CH_3), 17.09 (d, J = 6.6 Hz, P-O-CH_2-***CH₃***), 14.04 (s, P-$(CH_2)_5$-***CH₃***), 13.42 (s, $^+$P-$(CH_2)_3$-***CH₃***), 12.59 (d, J = 48.7 Hz, $^+$P-***CH₂***-CH_3), 6.11 (d, J = 5.7 Hz, $^+$P-CH_2-***CH₃***).

$^{31}P\{^1H\}$ NMR ($CDCl_3$, 162 MHz, δ in ppm) 34.65 (s, $^+$P), 23.19 – 22.70 (m).

5.9 Tri-*n*-butyl ethyl phosphonium decyl phosphonic acid ethyl ester [P_{4442}][DecPE]

41.61 mmol (8.42 g / 10.30 mL) tri-*n*-butyl phosphine were mixed with 49.93 mmol (13.90 g) decyl phosphonic acid diethyl ester at 180 °C. Phosphine turnover remained unchanged after 200 hours. 200 mL water were added to the mixture and liquid extraction performed with three times with 5 mL pentane, diethyl ether and dichloromethane each, respectively. The product was a colorless oil with a yield of 12.80 g (64.0 % of theory).

^1H NMR ($CDCl_3$, 400 MHz, δ in ppm) 3.74 (p, J = 6.9 Hz, 2H, P-O-***CH₂***-CH_3), 2.47 (dq, J = 13.2 Hz, J = 7.7 Hz, 2H, $^+$P-***CH₂***-CH_3), 2.39 – 2.21 (m, 6H, $^+$P-***CH₂***-$(CH_2)_2$-CH_3), 1.52 – 1.33 (m, 16H, $^+$P-CH_2-***CH₂***-***CH₂***-CH_3, P-***CH₂***-***CH₂***-***CH₂***-$(CH_2)_6$-CH_3), 1.21 – 1.05 (m, 20H, $^+$P-CH_2-***CH₃***, P-O-CH_2-***CH₃***, P-$(CH_2)_3$-***CH₂***-***CH₂***-***CH₂***-***CH₂***-***CH₂***-***CH₂***-CH_3), 0.85 (t, 9H, $^+$P-$(CH_2)_3$-***CH₃***), 0.74 (t, J = 6.8 Hz, 3H, P-$(CH_2)_9$-***CH₃***).

$^{13}C\{^1H\}$ NMR ($CDCl_3$, 101 MHz, δ in ppm) 59.01 (d, J = 5.4 Hz, P-O-***CH₂***-CH_3), 31.78 (s, P-$(CH_2)_7$-***CH₂***-CH_2-CH_3), 31.54 (d, J = 16.9 Hz, P-$(CH_2)_2$-***CH₂***-$(CH_2)_6$-CH_3), 29.51 (d, J = 3.3 Hz, P-$(CH_2)_3$-***CH₂***-***CH₂***-***CH₂***-***CH₂***-$(CH_2)_2$-CH_3), 29.21 (s, P-***CH₂***-$(CH_2)_8$-CH_3), 23.90 (d, J = 15.2 Hz, $^+$P-CH_2-CH_2-***CH₂***-CH_3), 23.74 (d, J = 4.8 Hz, $^+$P-CH_2-***CH₂***-CH_2-CH_3), 22.54 (s, P-CH_2-***CH₂***-$(CH_2)_6$-***CH₂***-CH_3), 18.22 (d,

J = 47.3 Hz, $^{+}$P-***CH₂***-$(CH_2)_2$-CH_3), 17.04 (d, J = 6.4 Hz, P-O-CH_2-***CH₃***), 13.98 (s, P-$(CH_2)_9$-***CH₃***), 13.39 (s, $^{+}$P-$(CH_2)_3$-***CH₃***), 12.56 (d, J = 48.7 Hz, $^{+}$P-***CH₂***-CH_3), 6.08 (d, J = 5.6 Hz, $^{+}$P-CH_2-***CH₃***).

$^{31}P\{^{1}H\}$ NMR ($CDCl_3$, 162 MHz, δ in ppm) 34.64 (s, $^{+}$P), 23.03 (s).

5.10 Tri-*n*-butyl ethyl phosphonium benzyl phosphonic acid ethyl ester [P_{4442}][BenzPE]

48.24 mmol (9.76 g / 11.95 mL) tri-*n*-butyl phosphine were mixed with 57.89 mmol (12.29 g) benzyl phosphonic acid diethyl ester at 180 °C. Phosphine turnover remained unchanged after 42 hours. 200 mL water were added to the mixture and liquid extraction performed with three times with 5 mL pentane, diethyl ether and dichloromethane each, respectively. The product was a colorless oil with a yield of 16.73 g (83.7 % of theory).

^{1}H NMR ($CDCl_3$, 400 MHz, δ in ppm) 7.25 (dd, J = 7.9 Hz, J = 1.8 Hz, 2H, P-CH_2-C-CH-***CH***-CH), 7.04 (t, J = 7.5 Hz, 2H, P-CH_2-C-***CH***-CH-CH), 6.97 – 6.88 (m, 1H, P-CH_2-C-CH-CH-***CH***), 3.69 (p, J = 7.0 Hz, 2H, P-O-***CH₂***-CH_3), 2.85 (d, J = 19.9 Hz, 2H, P-***CH₂***-Ph), 2.28 – 1.94 (m, 8H, $^{+}$P-***CH₂***-$(CH_2)_2$-CH_3, $^{+}$P-***CH₂***-CH_3), 1.43 – 1.24 (m, 12H, $^{+}$P-CH_2-***CH₂***-***CH₂***-CH_3), 1.05 – 0.92 (m, 6H, $^{+}$P-CH_2-***CH₃***, P-O-CH_2-***CH₃***), 0.80 (t, J = 7.0 Hz, 9H, $^{+}$P-$(CH_2)_3$-***CH₃***).

$^{13}C\{^{1}H\}$ NMR ($CDCl_3$, 101 MHz, δ in ppm) 129.79 (d, J = 5.7 Hz, P-CH_2-***C***-CH-CH-CH), 127.44 (d, J = 2.5 Hz, P-CH_2-C-***CH***-CH-CH, P-CH_2-C-CH-***CH***-CH), 124.38 (d, J = 3.2 Hz, P-CH_2-C-CH-CH-***CH***), 59.58 (d, J = 5.8 Hz, P-O-***CH₂***-CH_3), 36.19 (d, J = 124.3 Hz, P-***CH₂***-Ph), 23.83 (d, J = 15.2 Hz, P-$(CH_2)_2$-***CH₂***-CH_3), 23.60 (d, J = 4.8 Hz, P-CH_2-***CH₂***-CH_2-CH_3), 18.01 (d, J = 47.3 Hz, $^{+}$P-***CH₂***-$(CH_2)_2$-CH_3), 16.97 (d, J = 6.4 Hz, P-O-CH_2-***CH₃***), 13.40 (s, $^{+}$P-$(CH_2)_2$-***CH₃***), 12.29 (d, J = 48.7 Hz, $^{+}$P-***CH₂***-CH_3), 5.97 (d, J = 5.7 Hz, $^{+}$P-CH_2-***CH₃***).

$^{31}P\{^{1}H\}$ NMR ($CDCl_3$, 162 MHz, δ in ppm) 37.20 – 29.51 (m, $^{+}$P), 16.55 (d, J = 20.7 Hz).

6. NMR spectra

6.1 Ethyl phosphonic acid diethyl ester

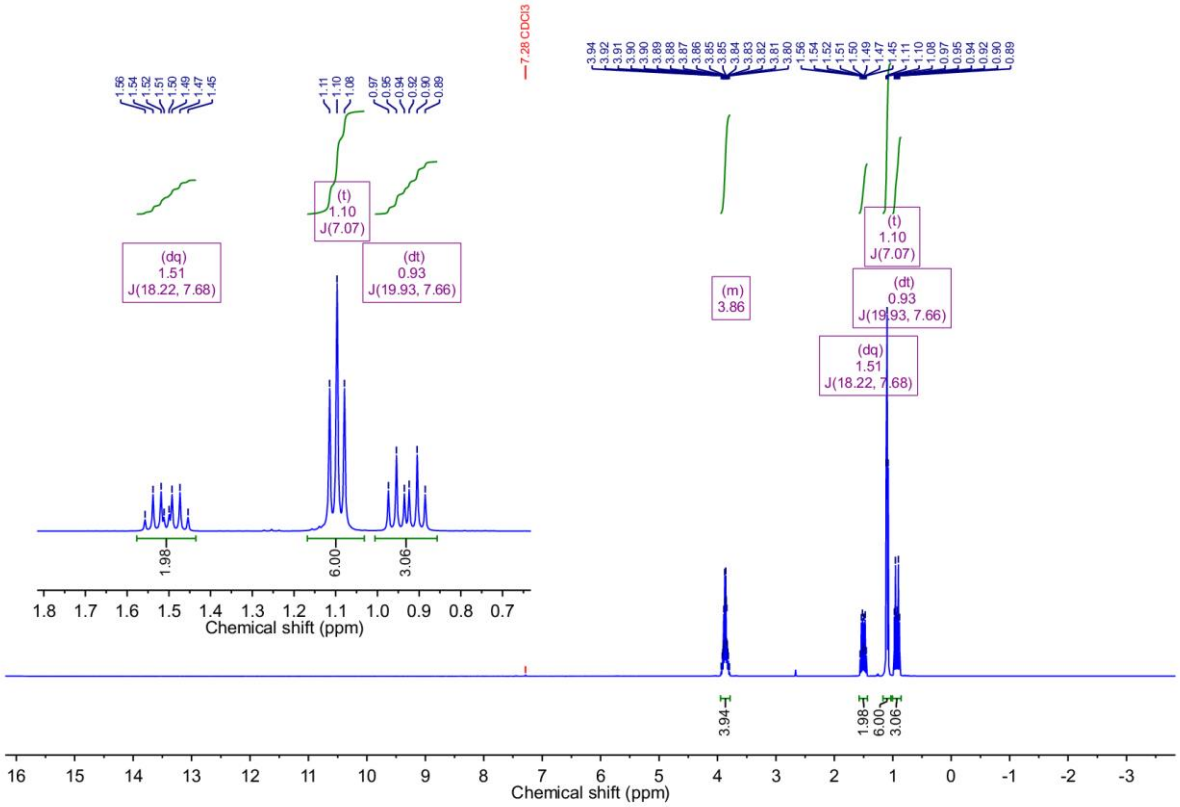

Figure S18. ^{1}H-NMR spectrum of ethyl phosphonic acid diethyl ester.

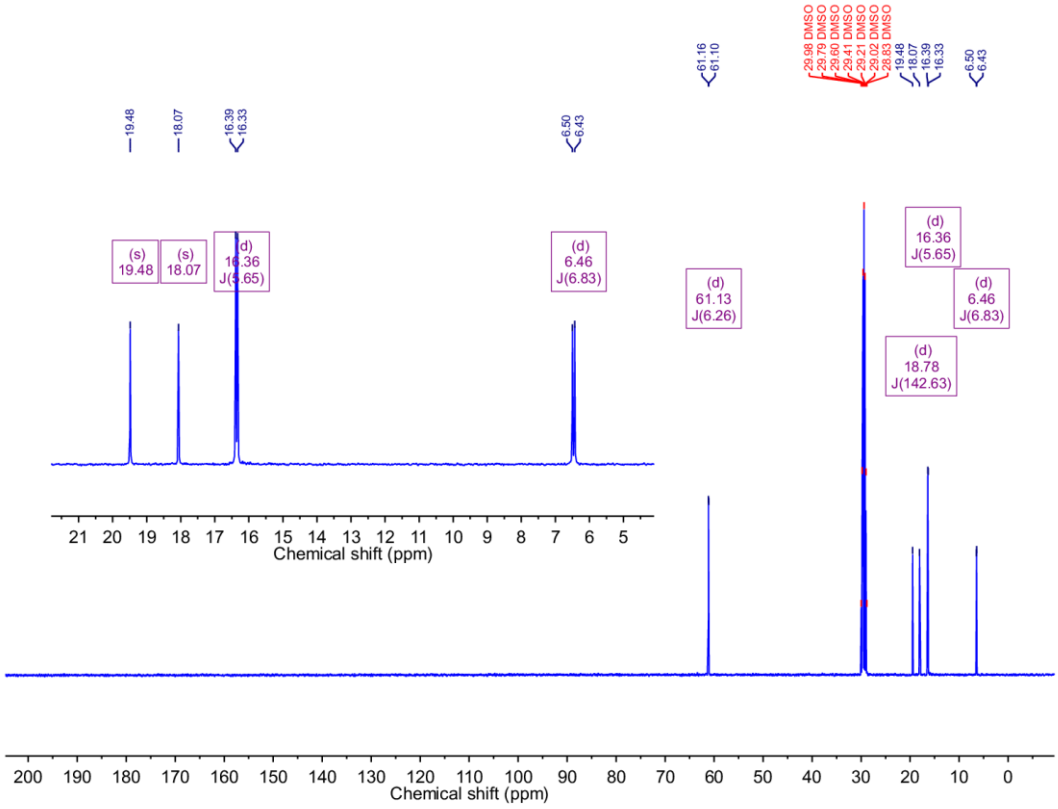

Figure S19. $^{13}C\{^{1}H\}$ NMR spectrum of ethyl phosphonic acid diethyl ester.

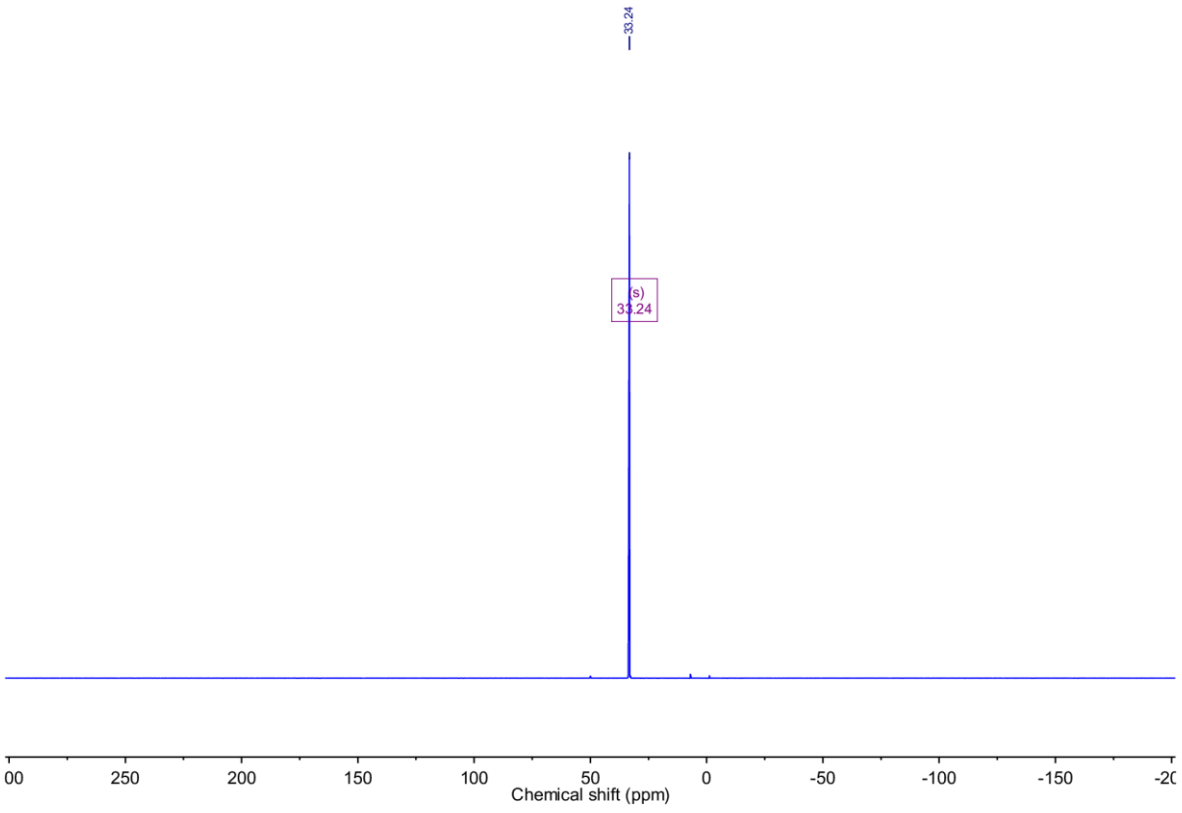

Figure S20. $^{31}P\{^{1}H\}$ NMR spectrum of ethyl phosphonic acid diethyl ester.

6.2 Hexyl phosphonic acid diethyl ester

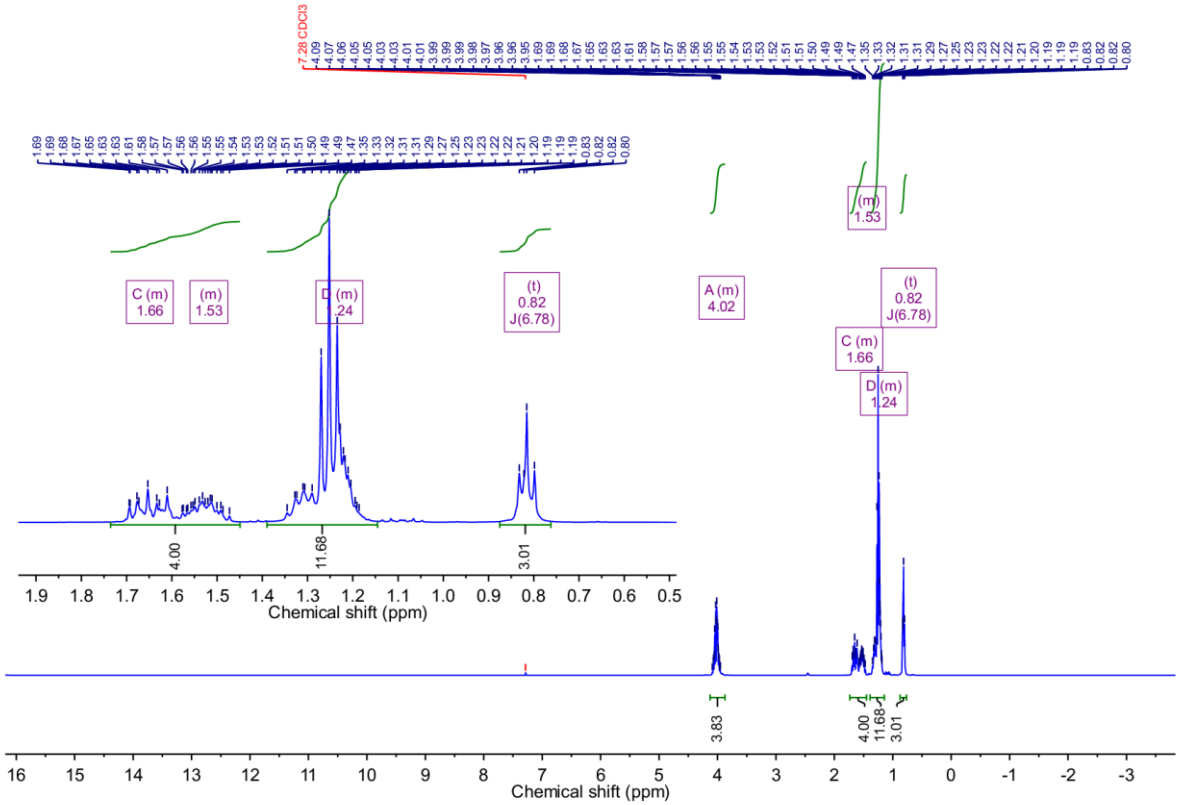

Figure S21. ^{1}H-NMR spectrum of hexyl phosphonic acid diethyl ester.

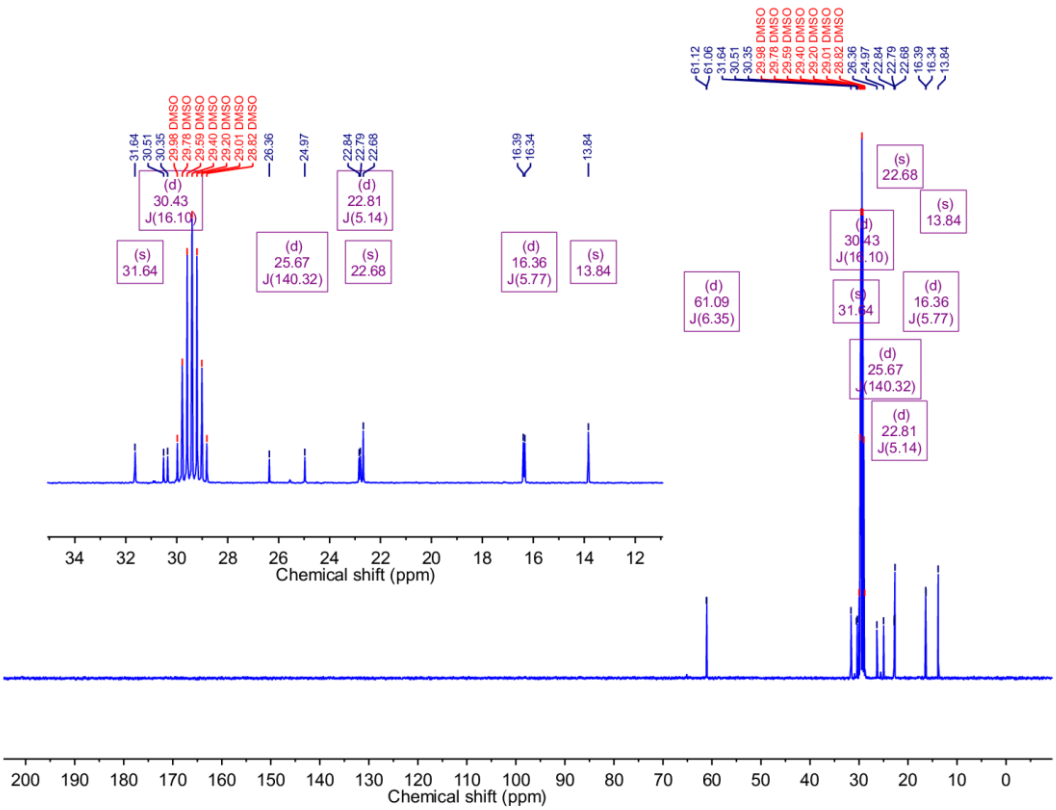

Figure S22. ^{13}C{^{1}H} NMR spectrum of hexyl phosphonic acid diethyl ester.

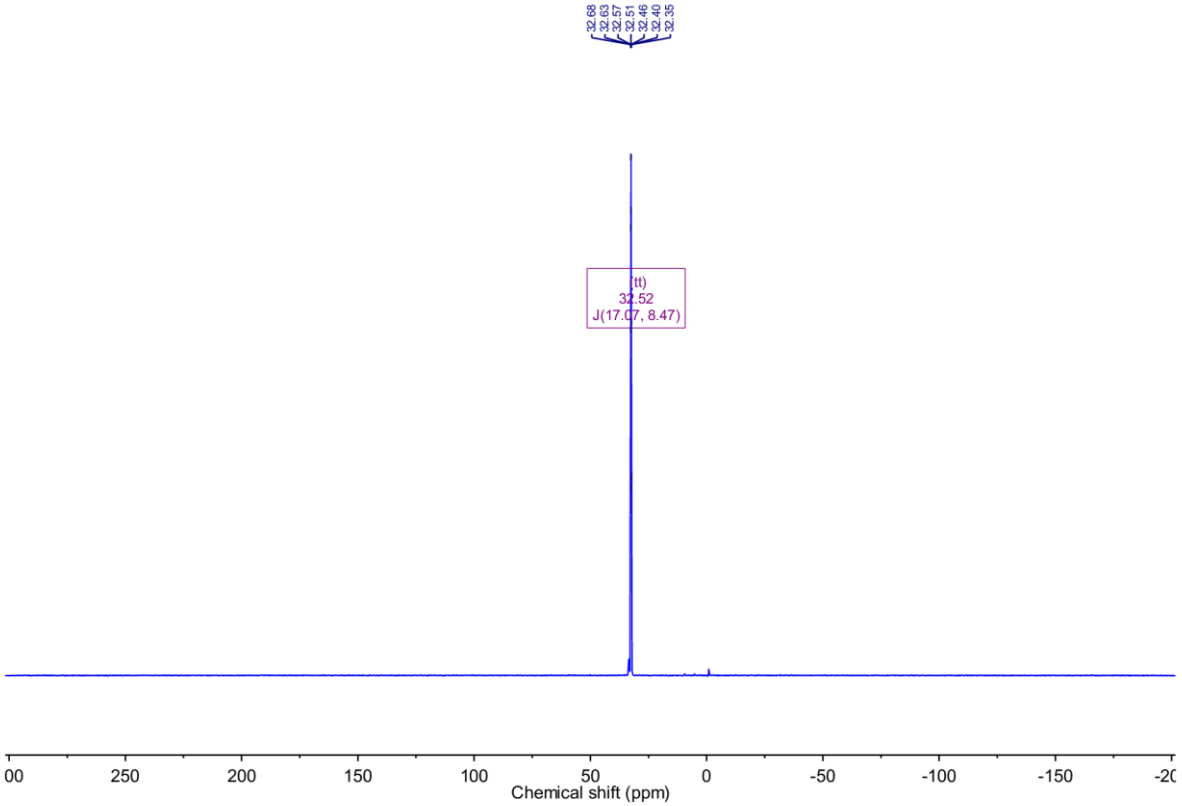

Figure S23. $^{31}P\{^{1}H\}$ NMR spectrum of hexyl phosphonic acid diethyl ester.

6.3 Decyl phosphonic acid diethyl ester

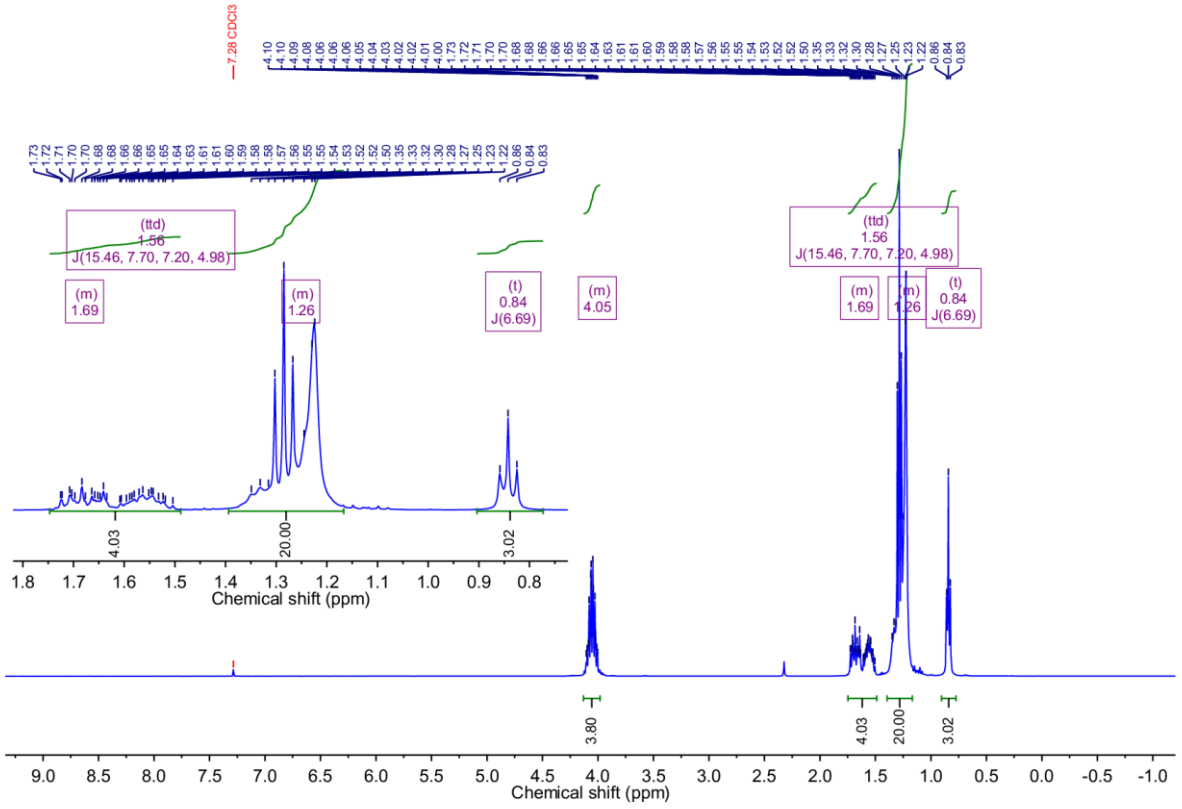

Figure S24. ^{1}H NMR spectrum of decyl phosphonic acid diethyl ester.

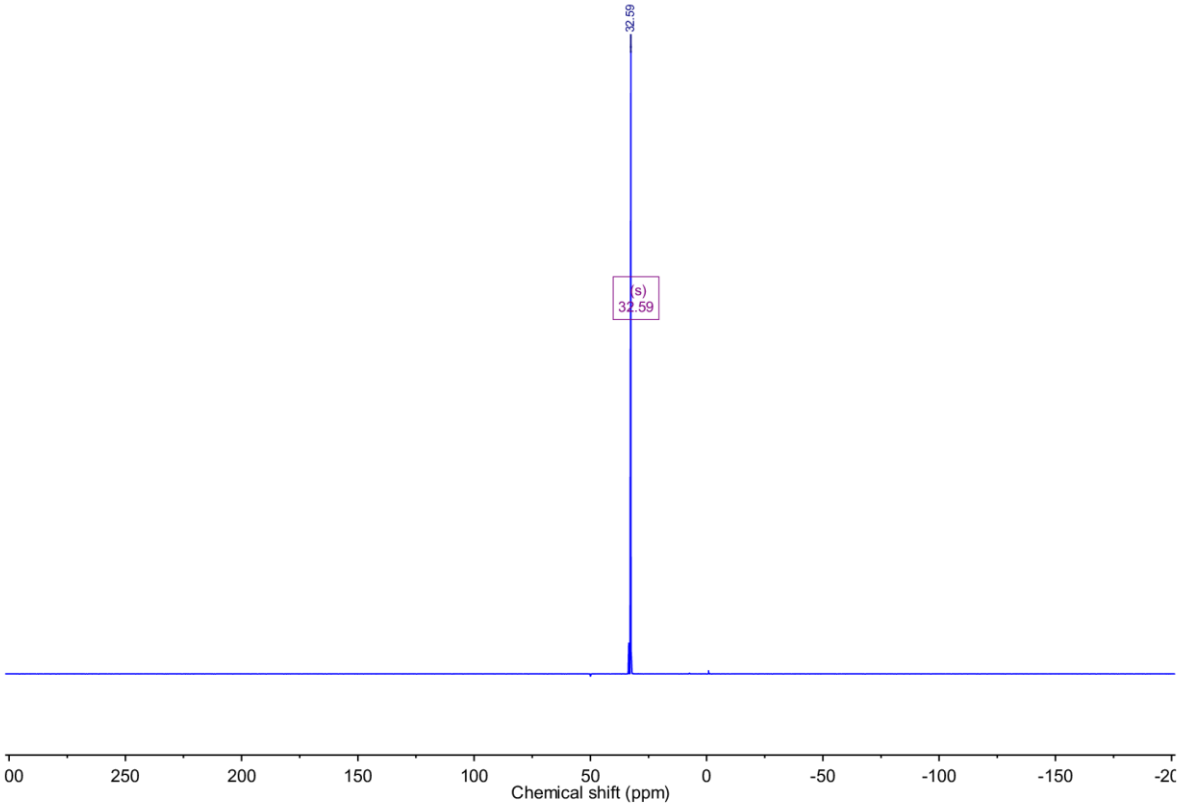

Figure S25. $^{31}P\{^{1}H\}$ NMR spectrum of decyl phosphonic acid diethyl ester.

6.4 Benzyl phosphonic acid diethyl ester

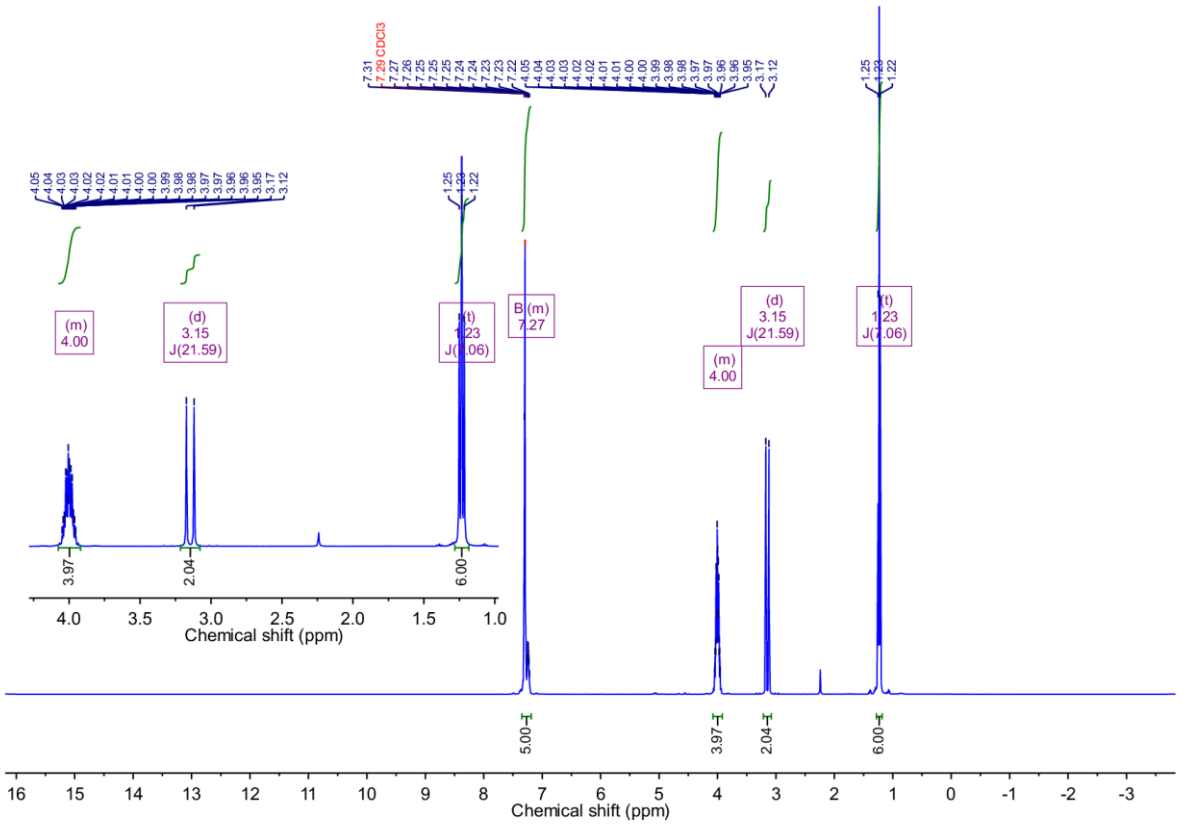

Figure S26. ^{1}H NMR spectrum of benzyl phosphonic acid diethyl ester.

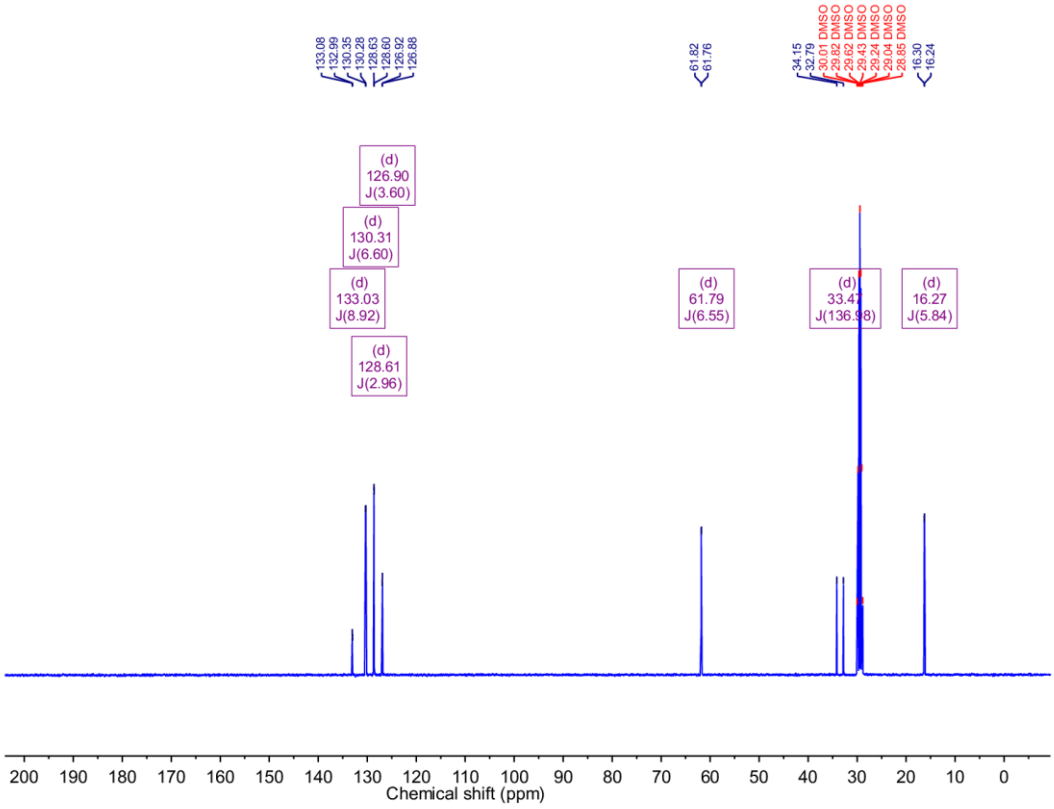

Figure S27. $^{13}C\{^{1}H\}$ NMR spectrum of benzyl phosphonic acid diethyl ester.

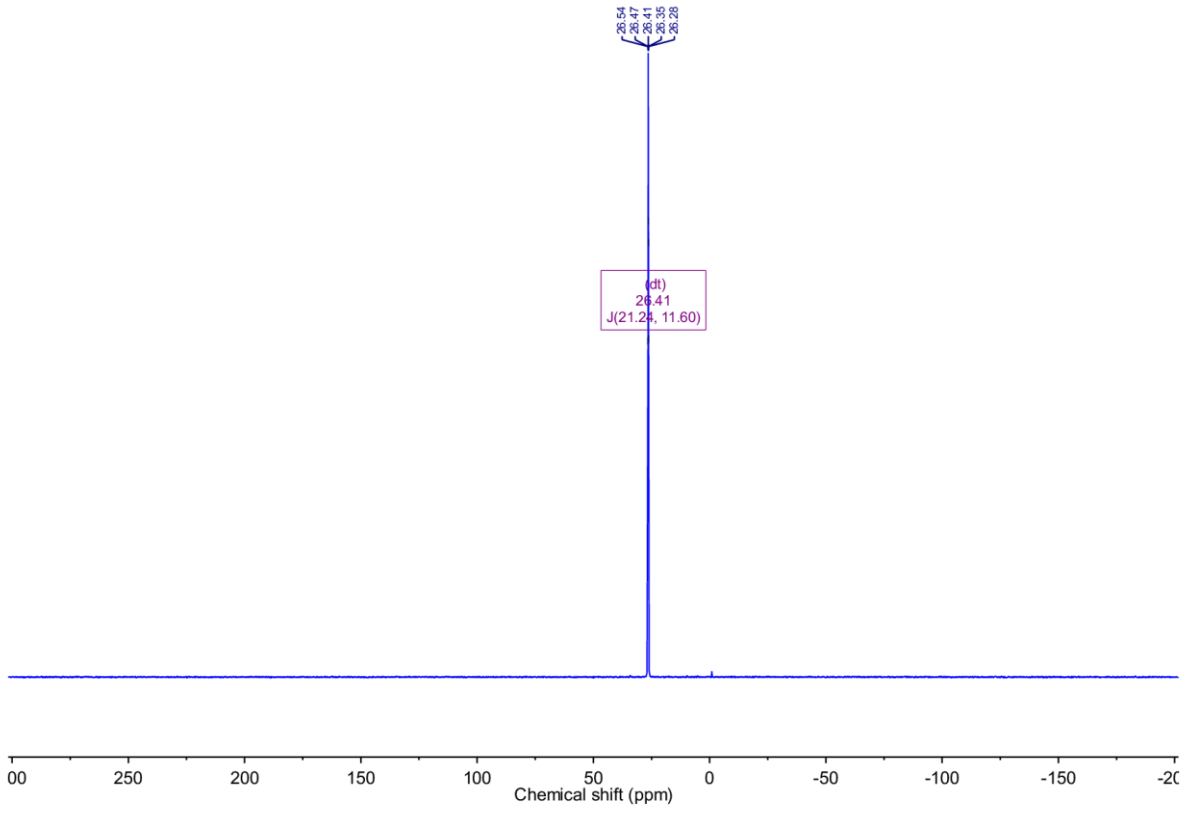

Figure S28. $^{31}P\{^{1}H\}$ NMR spectrum of benzyl phosphonic acid diethyl ester.

6.5 Tri-*n*-butyl methyl phosphonium dimethylphosphate [P_{4441}][DMP]

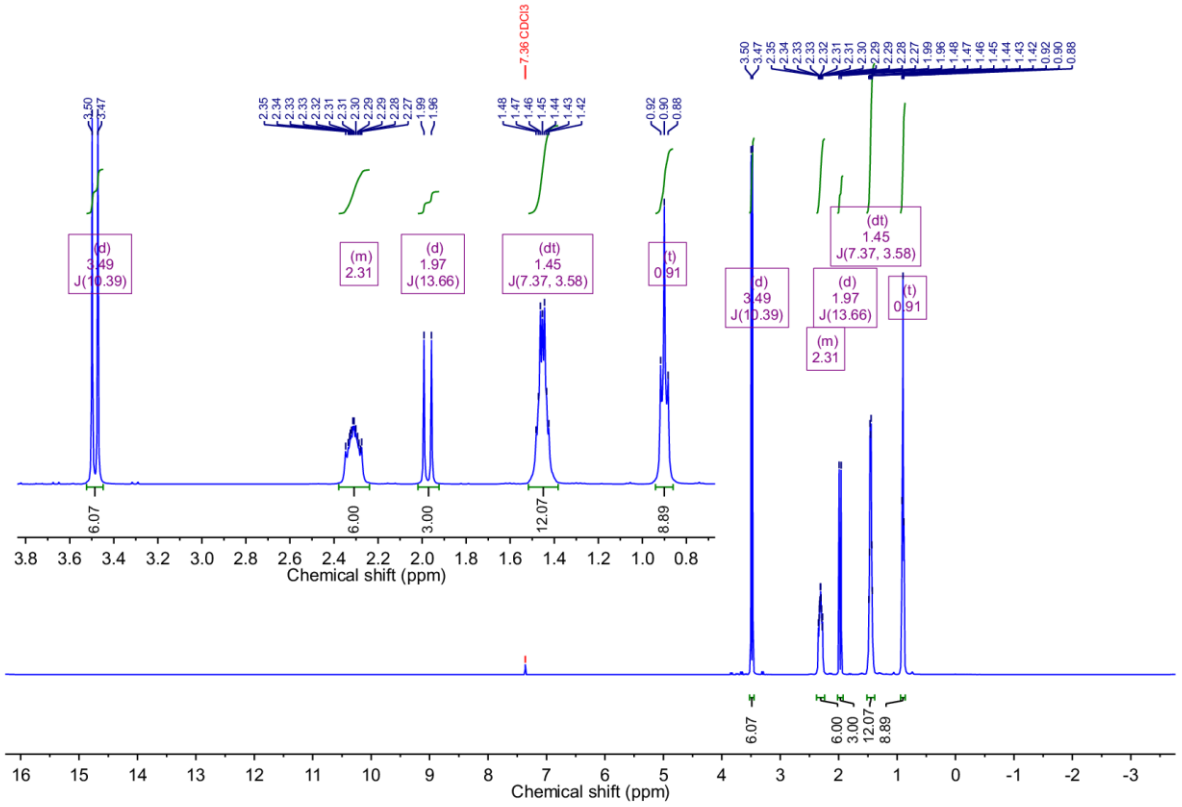

Figure S29. ^{1}H NMR spectrum of [P_{4441}][DMP].

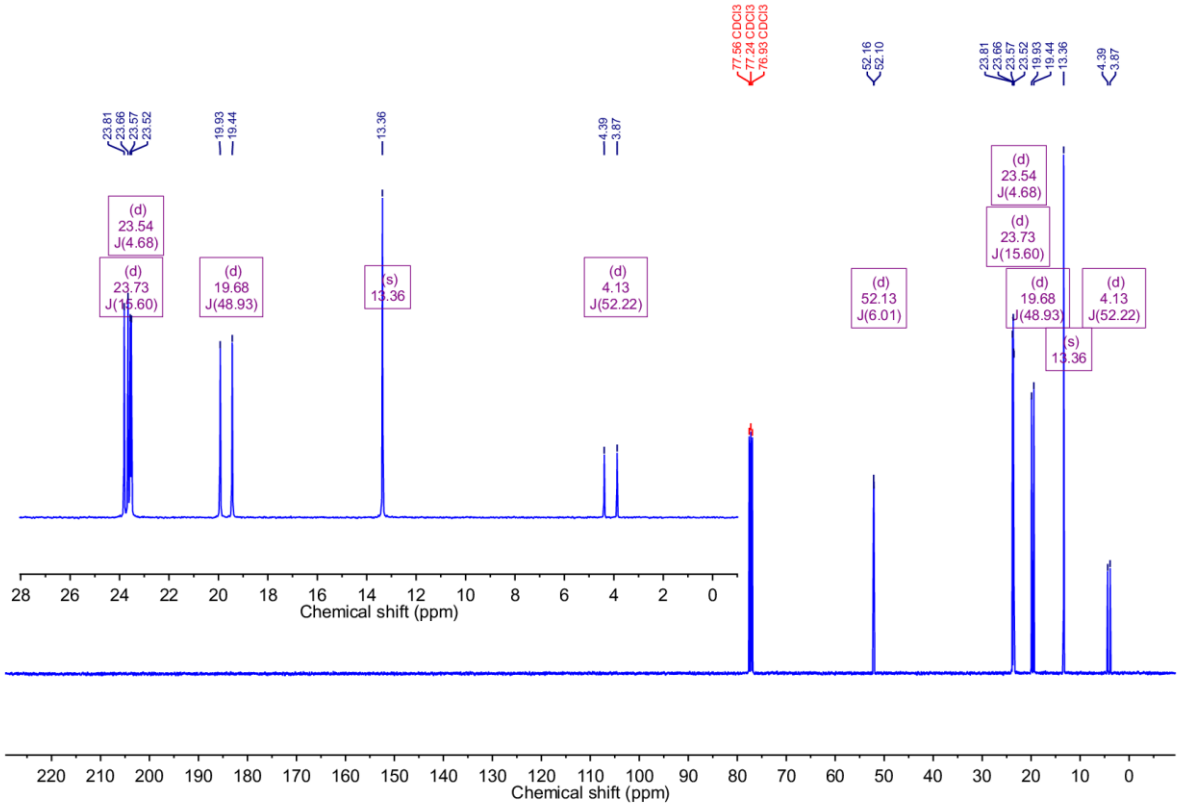

Figure S30. ^{13}C{^{1}H} NMR spectrum of [P_{4441}][DMP].

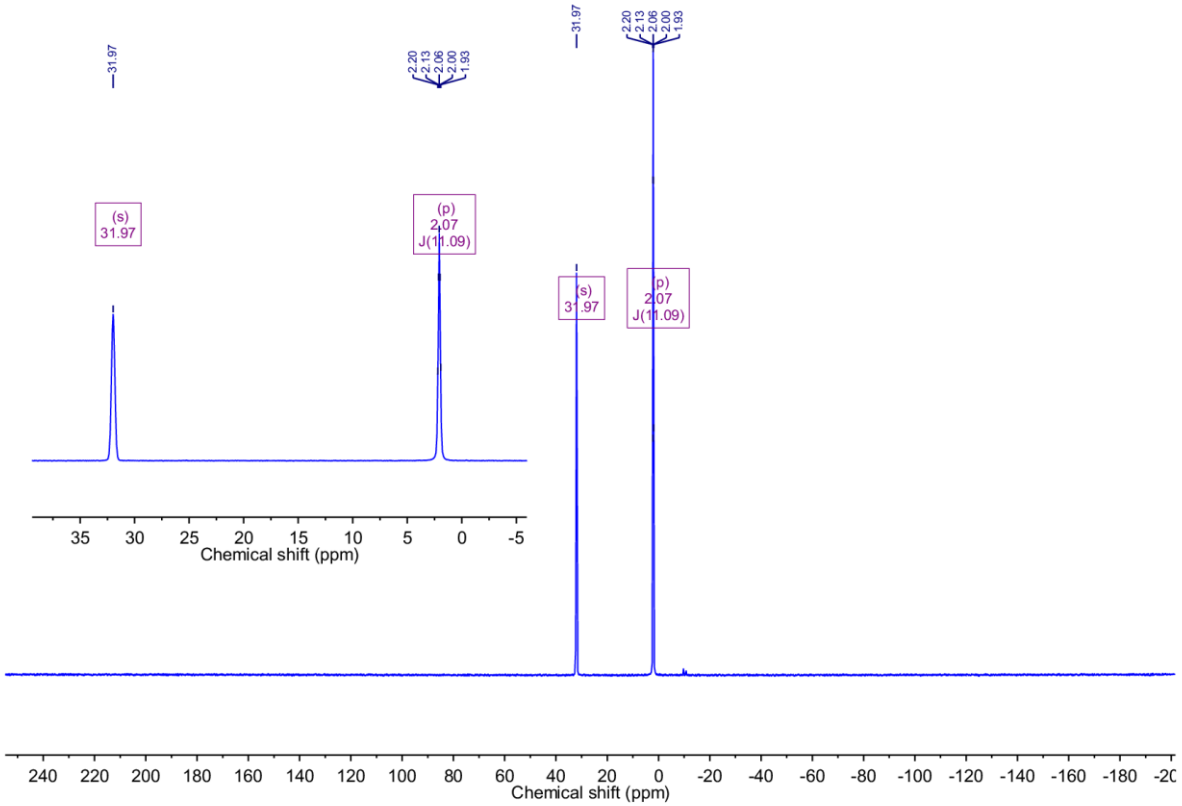

Figure S31. $^{31}P\{^{1}H\}$ NMR spectrum of $[P_{4441}][DMP]$.

6.6 Tri-*n*-butyl ethyl phosphonium diethylphosphate $[P_{4442}][DEP]$

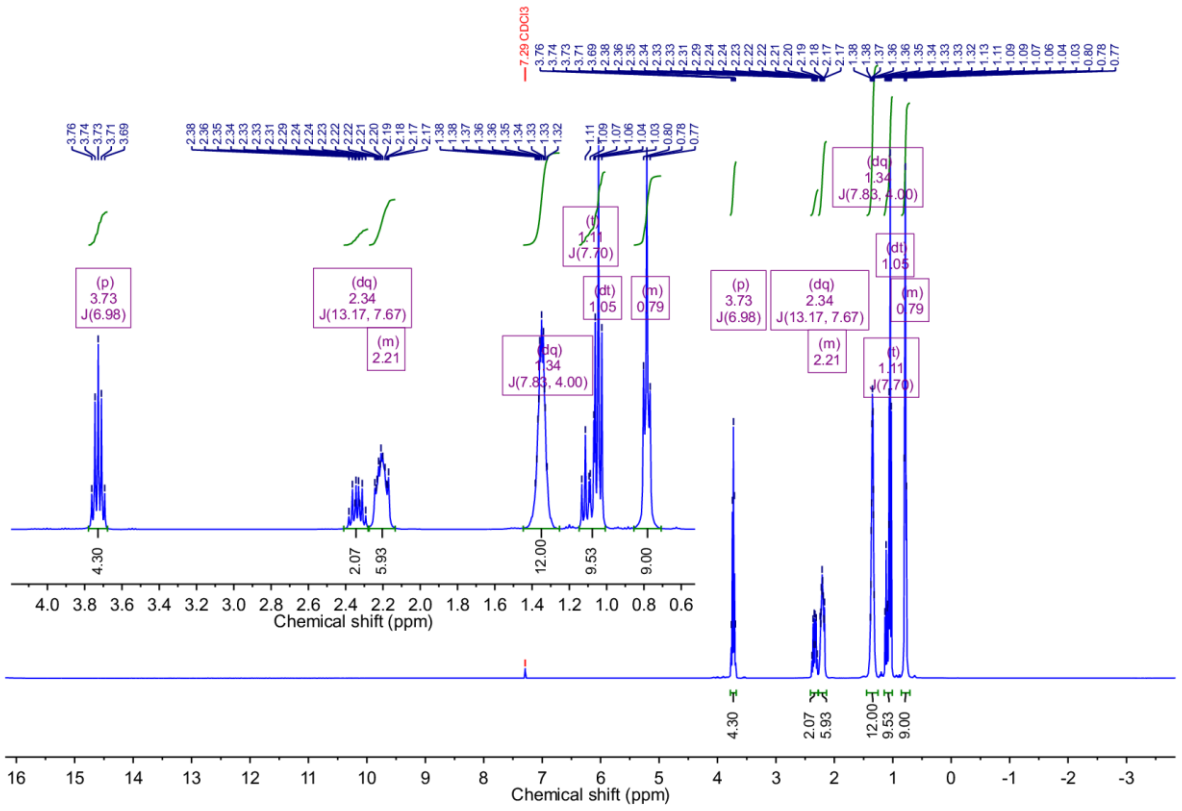

Figure S32. ^{1}H NMR spectrum of $[P_{4442}][DEP]$.

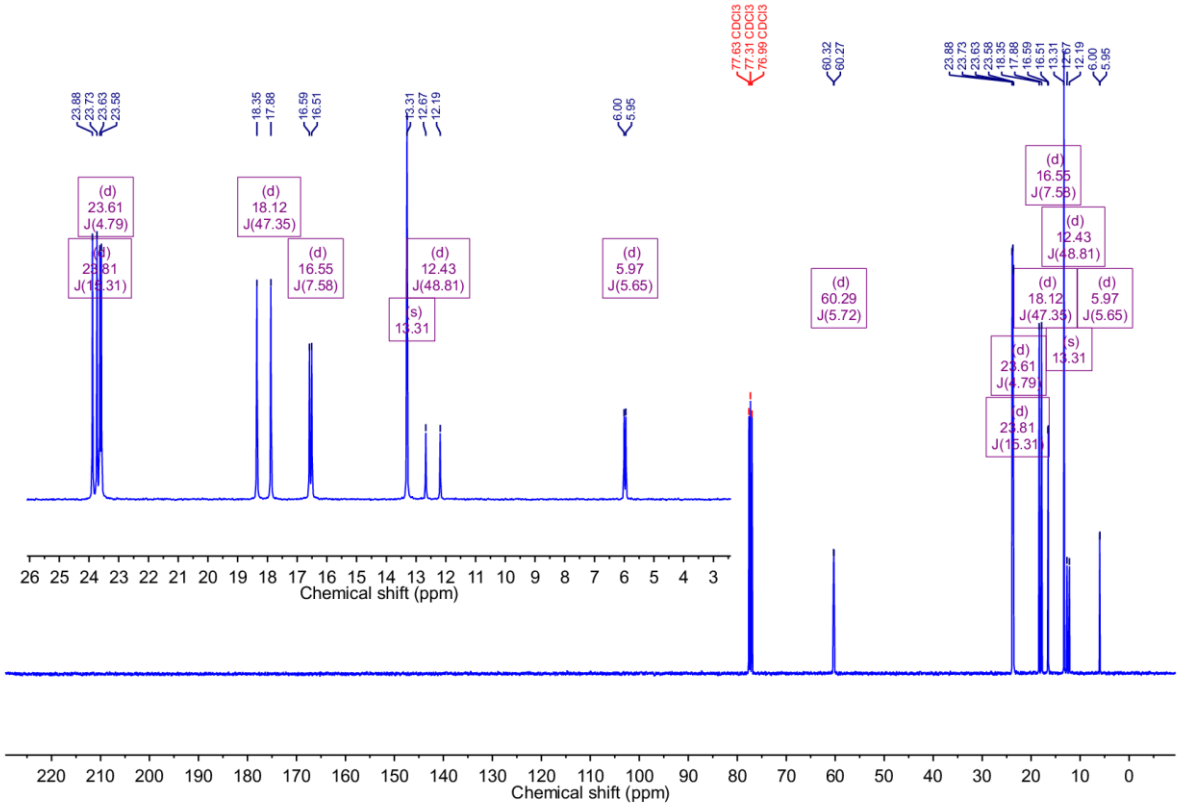

Figure S33. $^{13}C\{^{1}H\}$ NMR spectrum of $[P_{4442}][DEP]$.

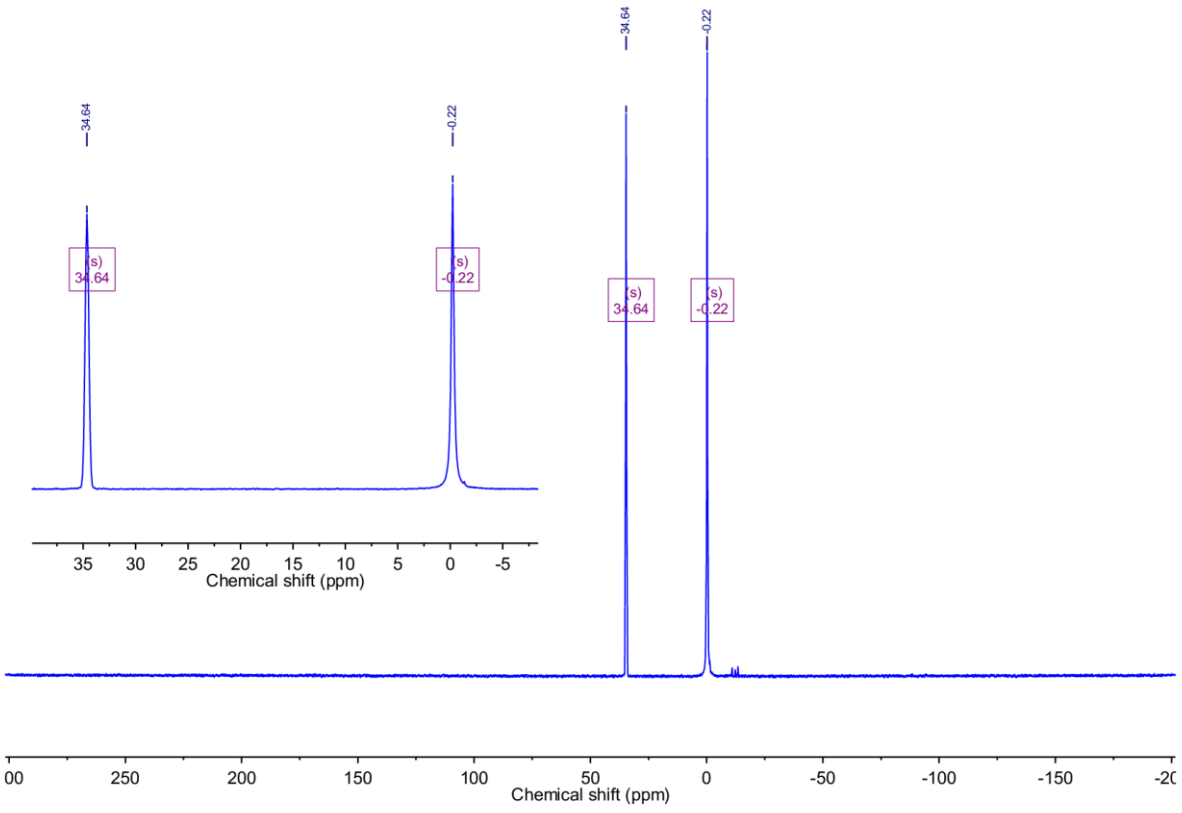

Figure S34. $^{31}P\{^{1}H\}$ NMR spectrum of $[P_{4442}][DEP]$.

6.7 Tri-*n*-butyl ethyl phosphonium ethyl phosphonic acid ethyl ester [P_{4442}][EtPE]

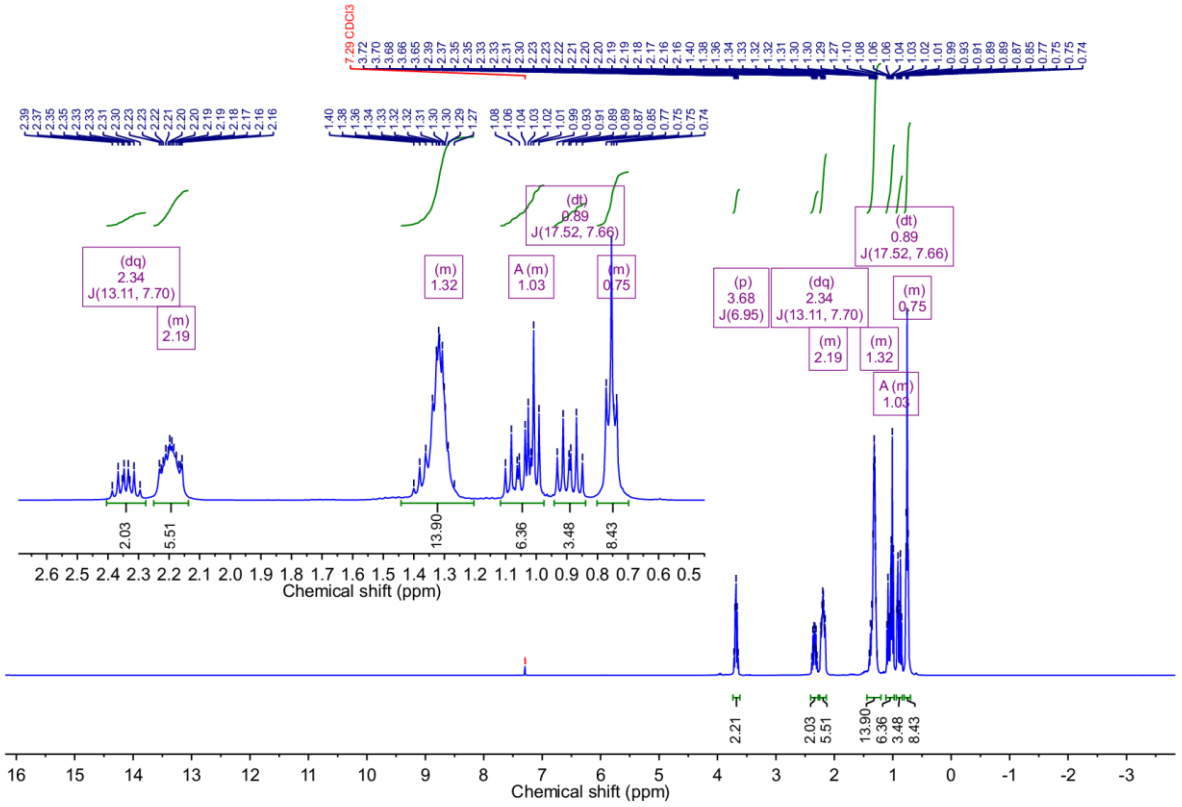

Figure S35. ^{1}H NMR spectrum of [P_{4442}][EtPE].

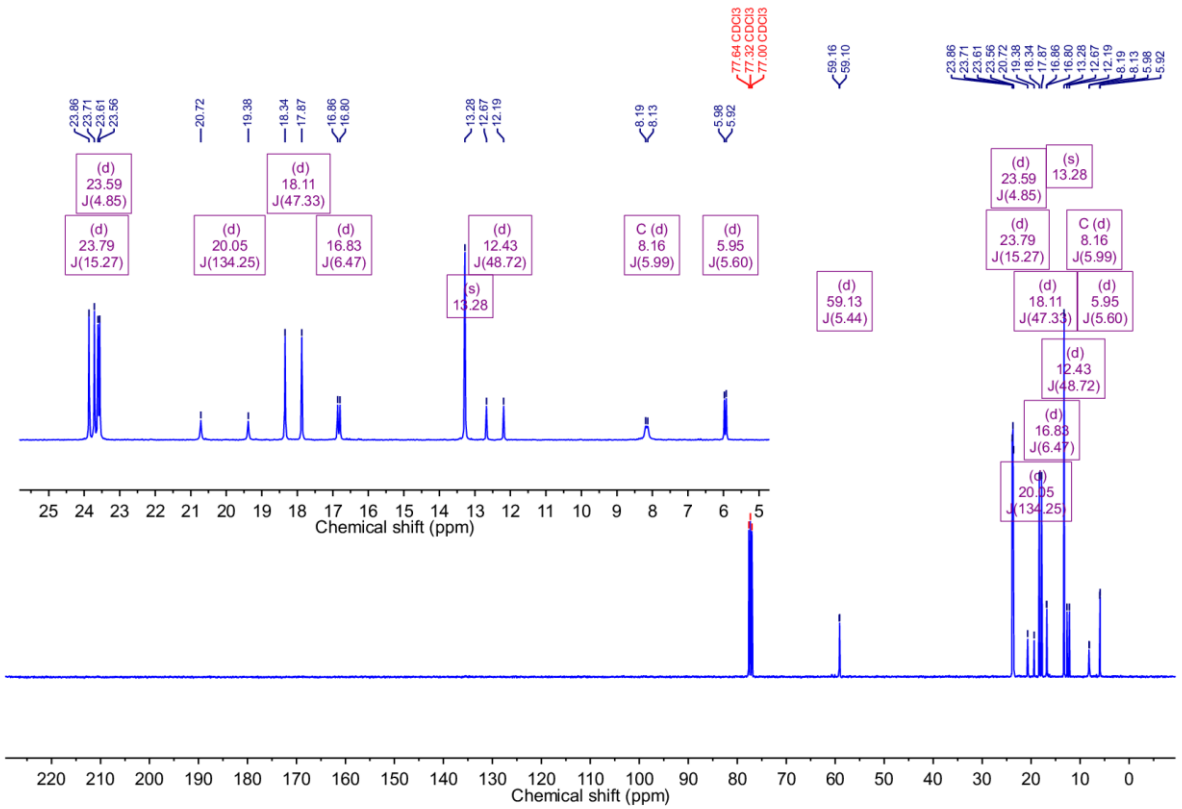

Figure S36. ^{13}C{^{1}H} NMR spectrum of [P_{4442}][EtPE].

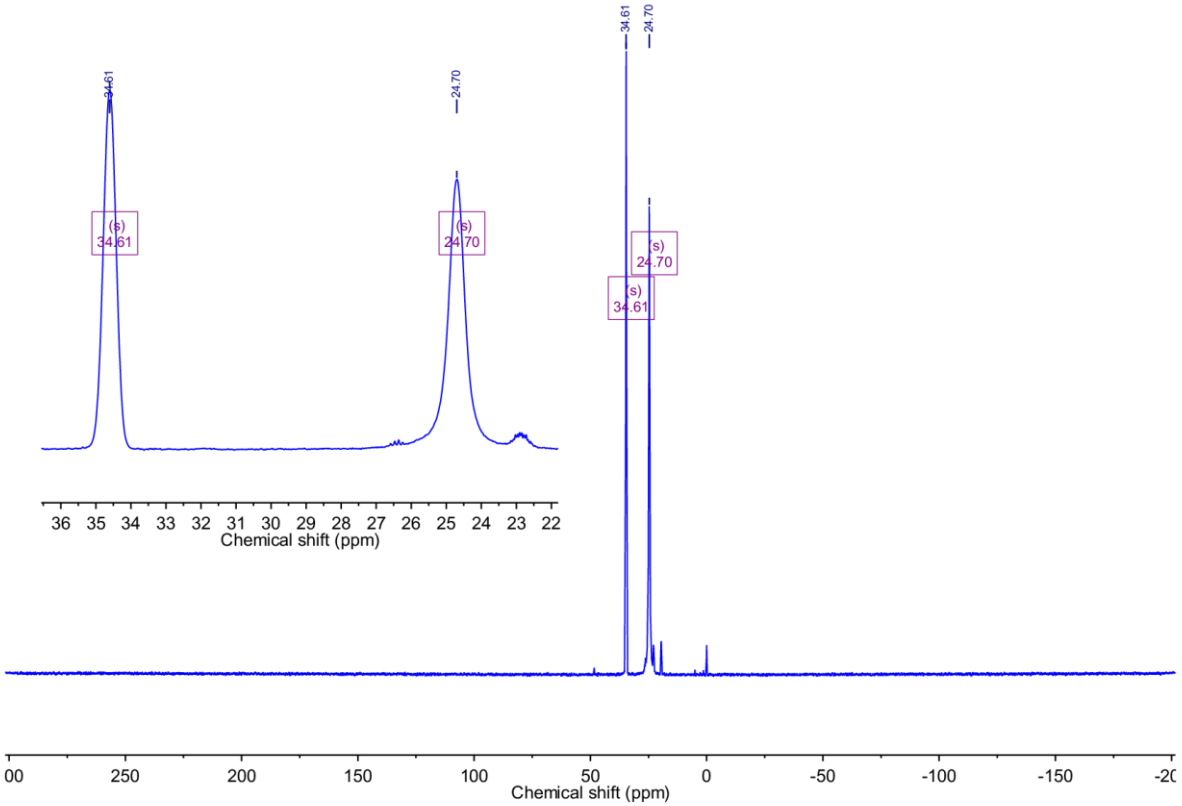

Figure S37. $^{31}P\{^{1}H\}$ NMR spectrum of [P_{4442}][EtPE].

6.8 Tri-*n*-butyl ethyl phosphonium hexyl phosphonic acid ethyl ester [P_{4442}][HexPE]

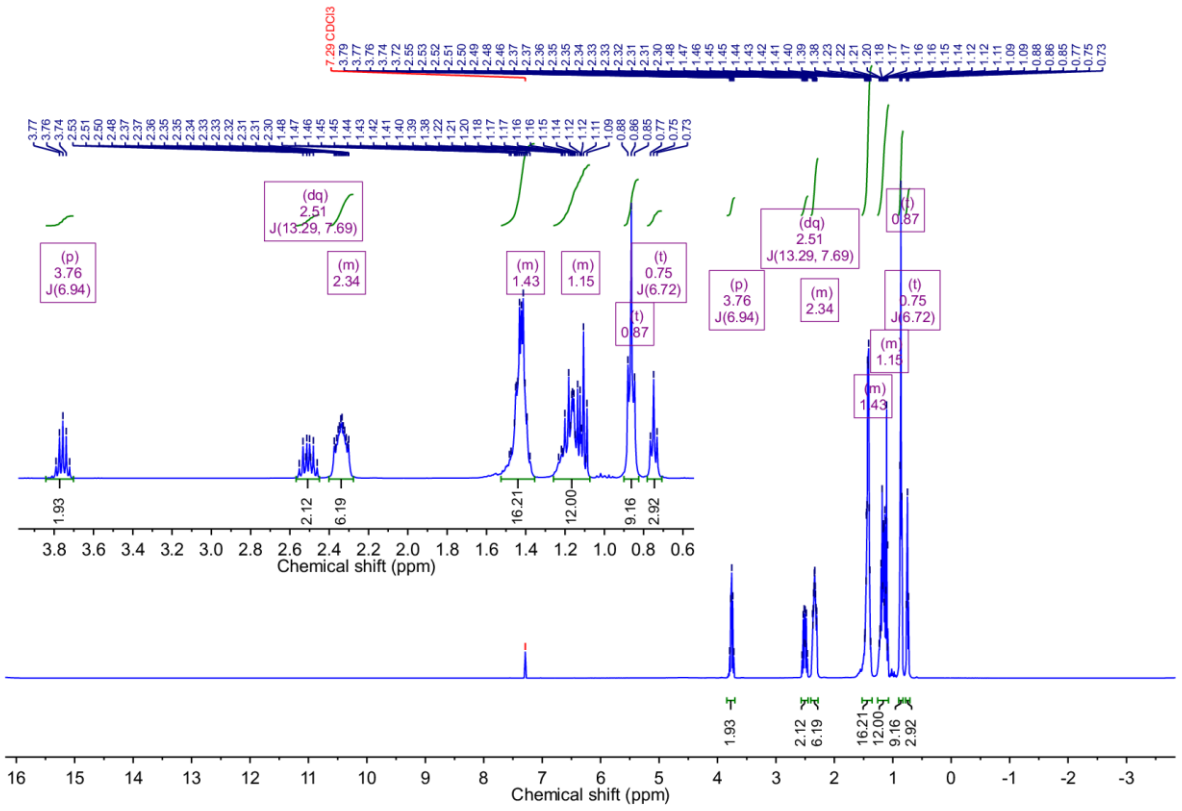

Figure S38. ^{1}H NMR spectrum of [P_{4442}][HexPE].

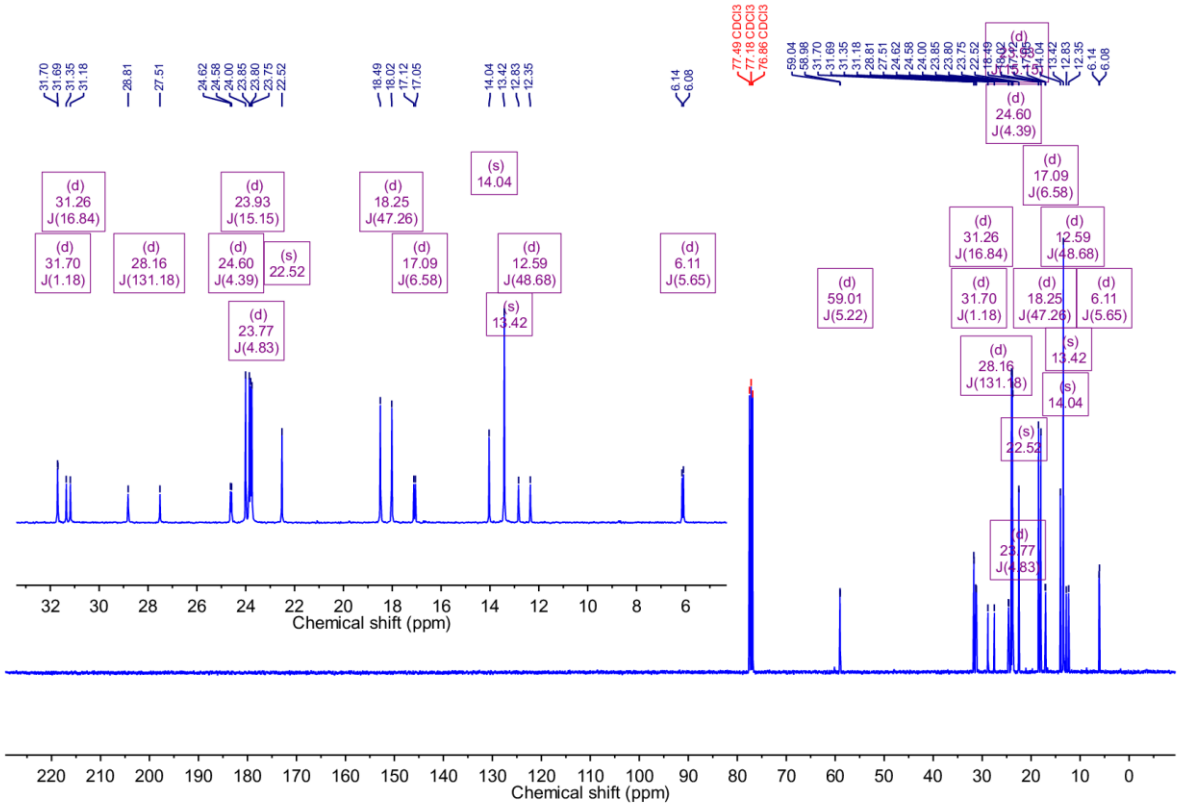

Figure S39. $^{13}C\{^{1}H\}$ NMR spectrum of $[P_{4442}][HexPE]$.

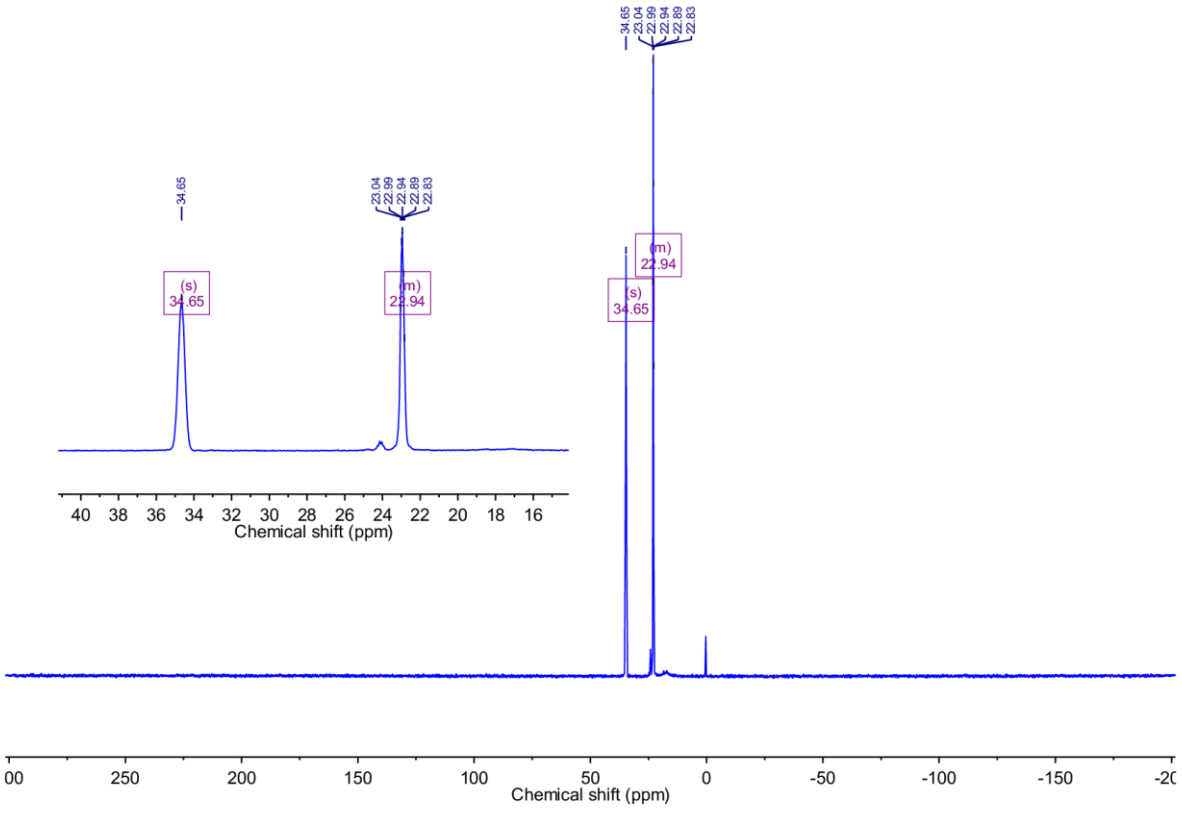

Figure S40. $^{31}P\{^{1}H\}$ NMR spectrum of $[P_{4442}][HexPE]$.

6.9 Tri-*n*-butyl ethyl phosphonium decyl phosphonic acid ethyl ester [P_{4442}][DecPE]

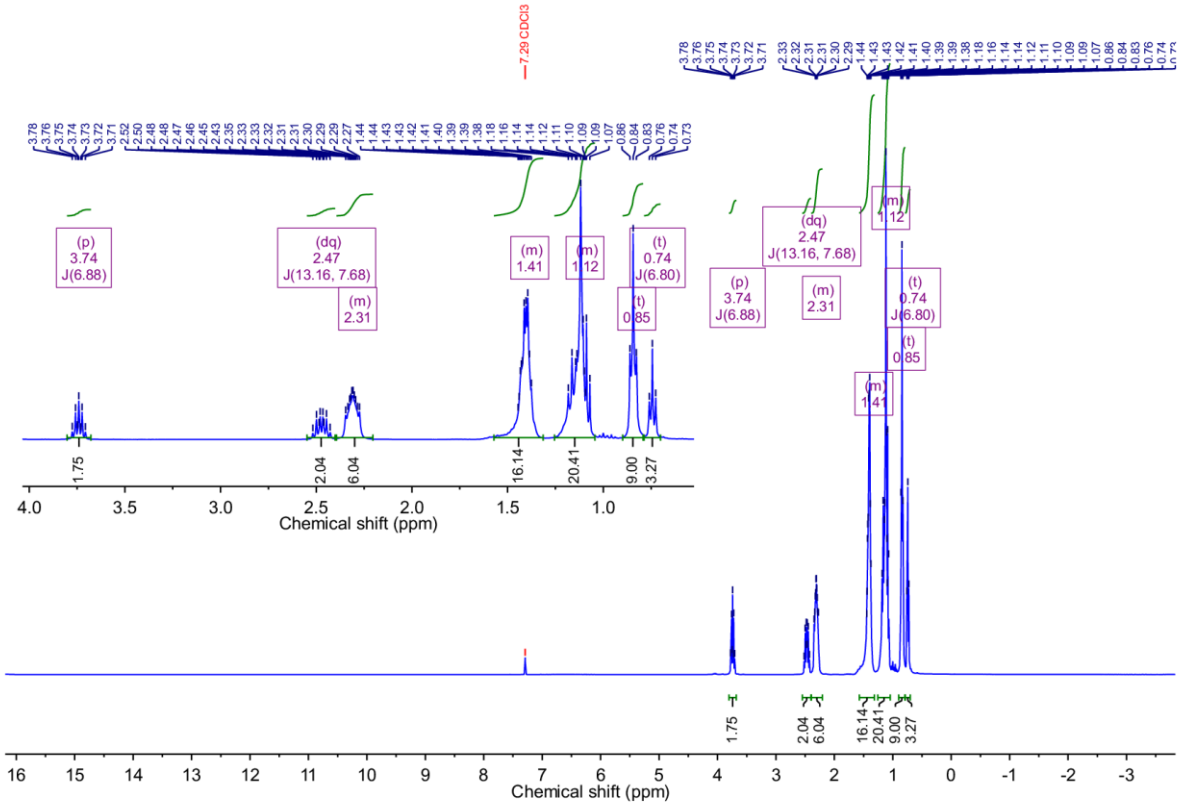

Figure S41. ^{1}H NMR spectrum of [P_{4442}][DecPE].

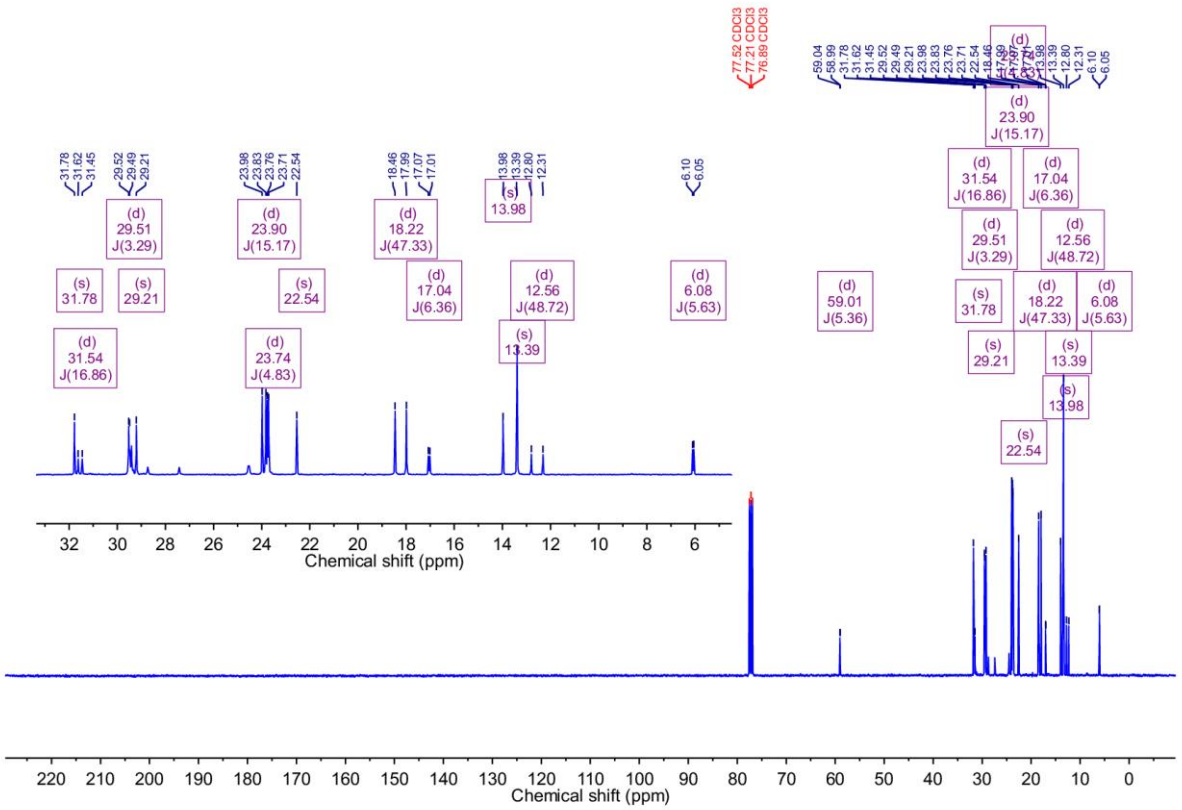

Figure S42. ^{13}C{^{1}H} NMR spectrum of [P_{4442}][DecPE].

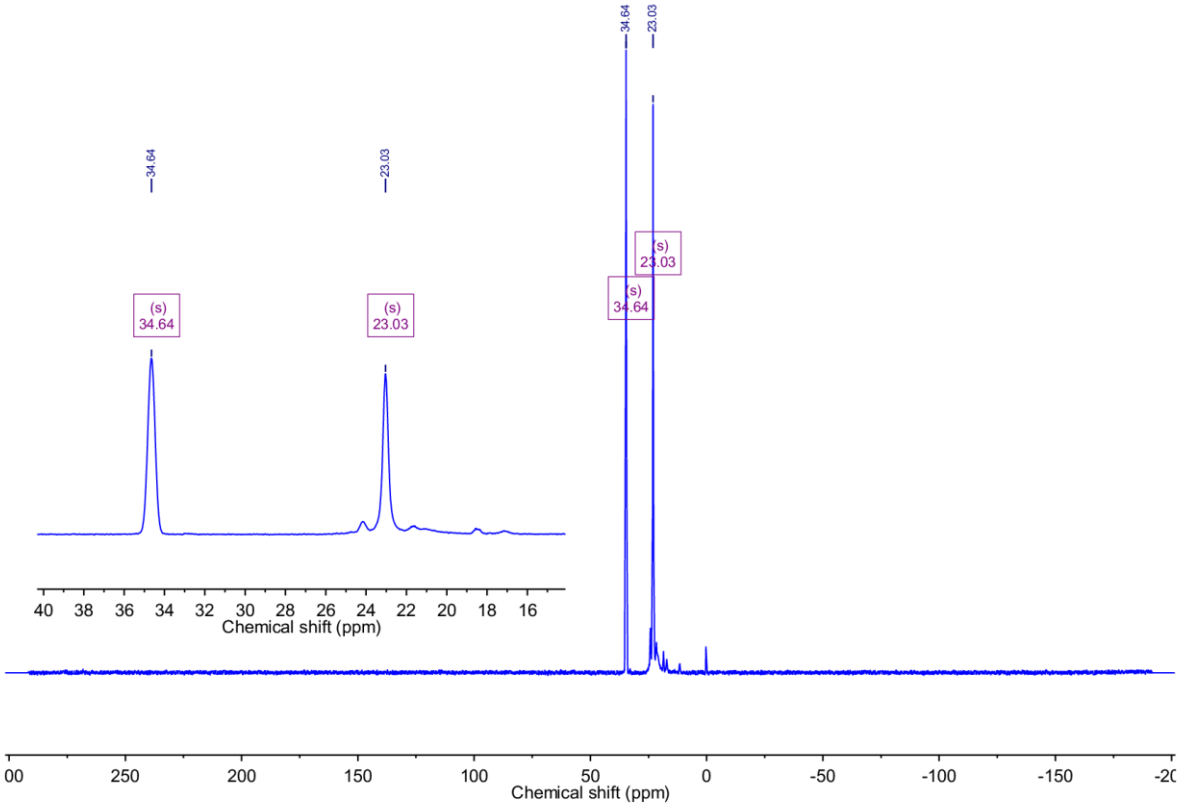

Figure S43. $^{31}P\{^{1}H\}$ NMR spectrum of $[P_{4442}][DecPE]$.

6.10 Tri-*n*-butyl ethyl phosphonium benzyl phosphonic acid ethyl ester $[P_{4442}][BenzPE]$

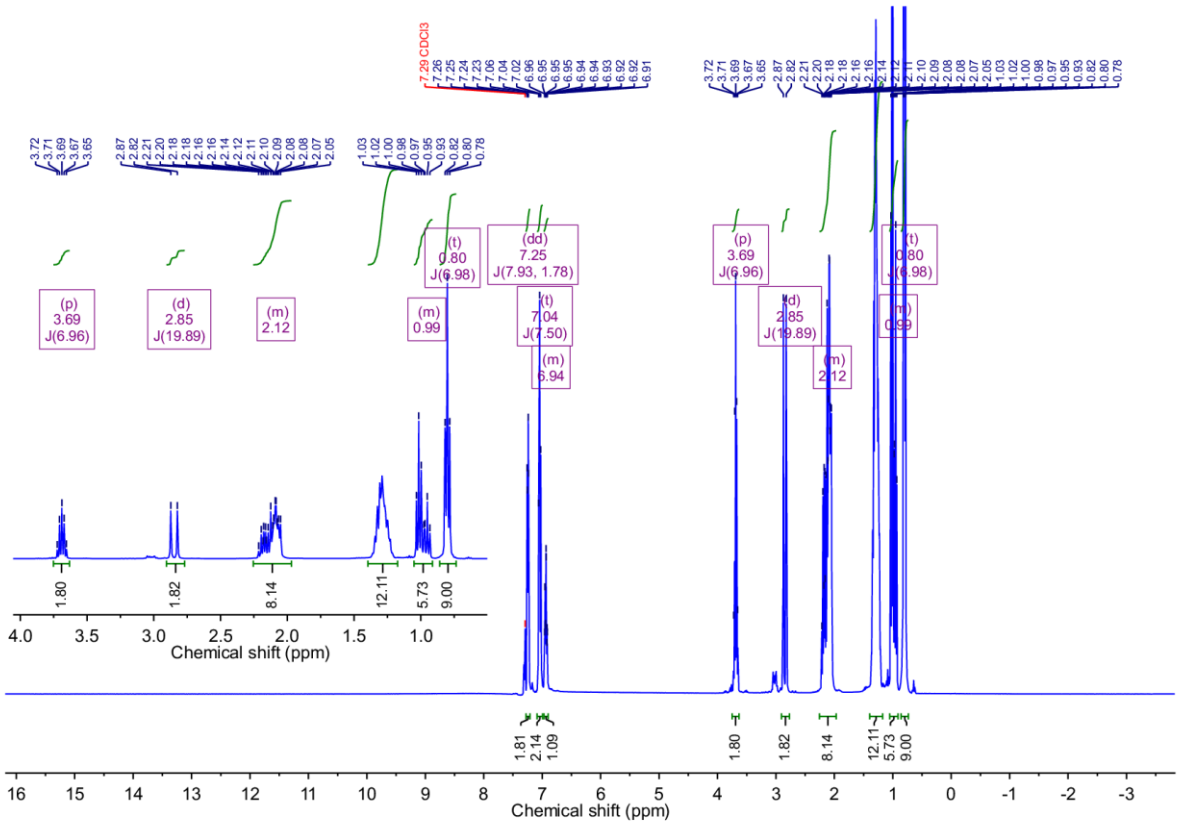

Figure S44. ^{1}H NMR spectrum of $[P_{4442}][BenzPE]$.

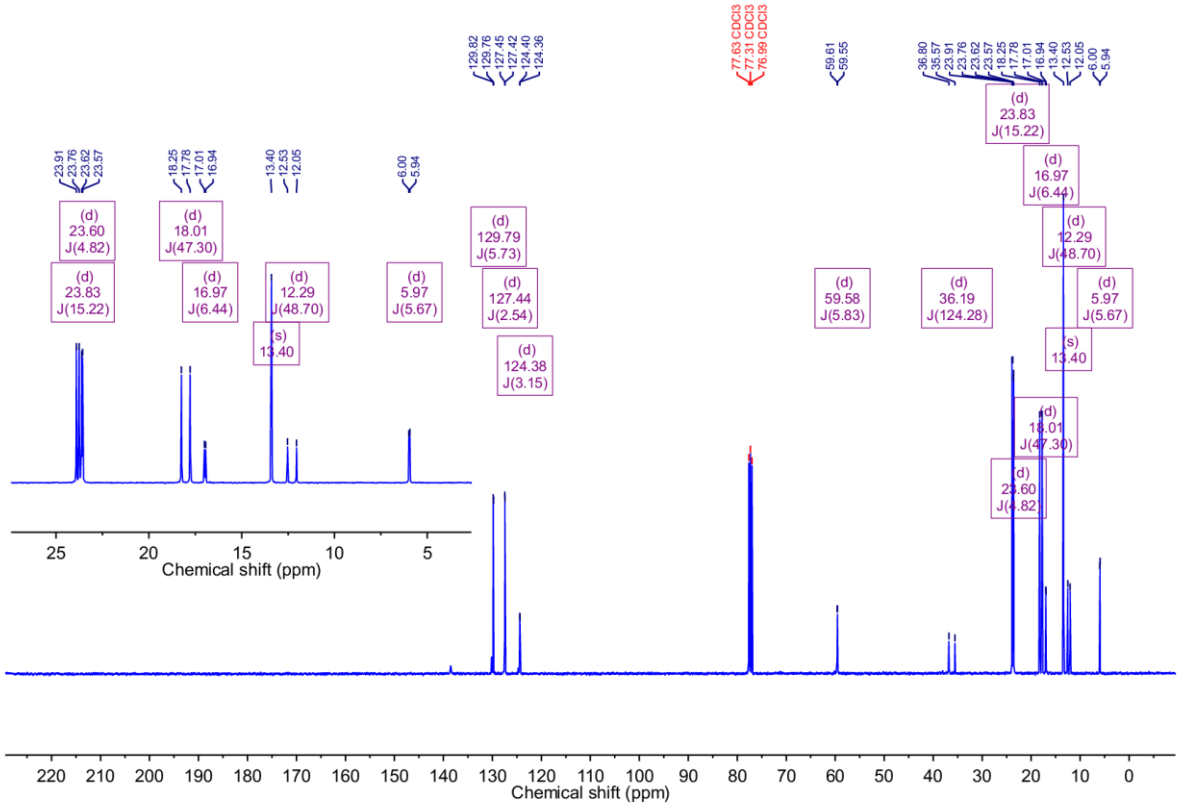

Figure S45. $^{13}C\{^{1}H\}$ NMR spectrum of $[P_{4442}][BenzPE]$.

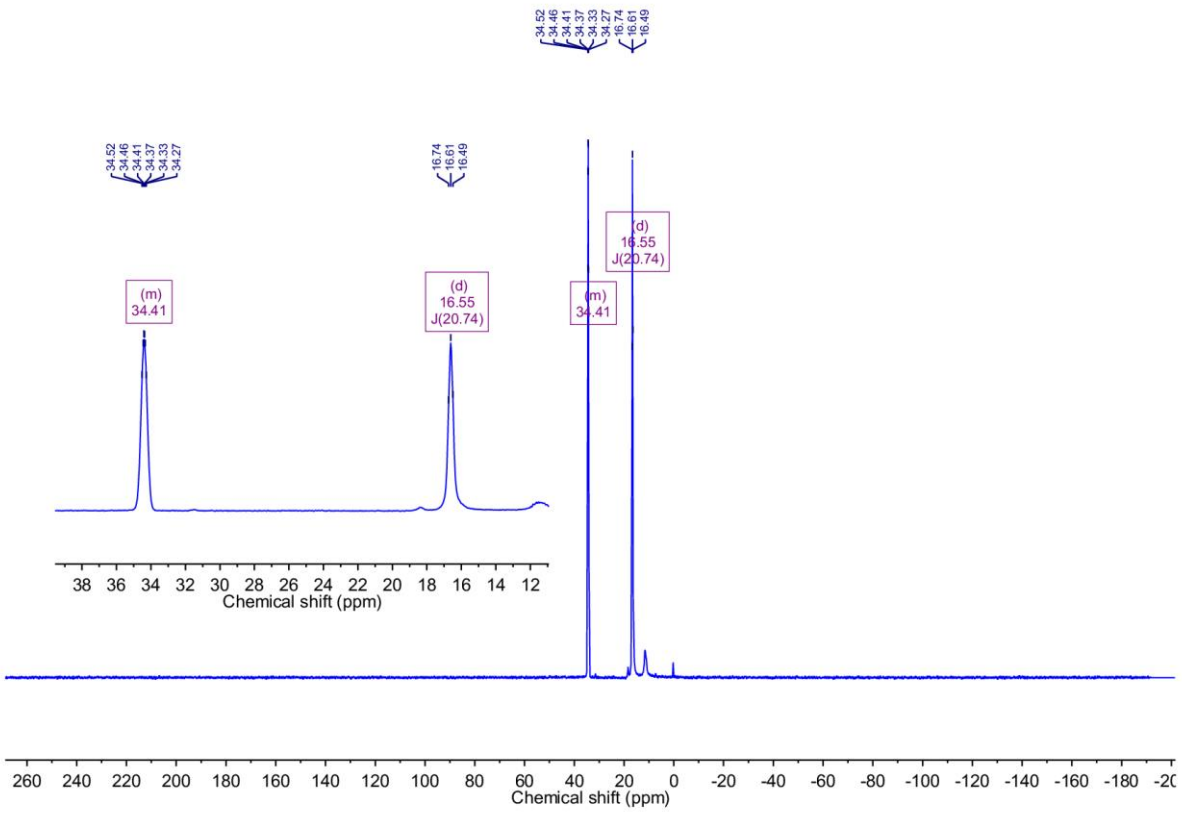

Figure S46. $^{31}P\{^{1}H\}$ NMR spectrum of $[P_{4442}][BenzPE]$.

References

1 A. M. Puziy, O. I. Poddubnaya, B. Gawdzik and J. M. D. Tascón, *Carbon*, 2020, **157**, 796–846.
2 H. Benaddi, D. Legras, J. N. Rouzaud and F. Beguin, *Carbon*, 1998, **36**, 306–309.
3 M. S. Solum, R. J. Pugmire, M. Jagtoyen and F. Derbyshire, *Carbon*, 1995, **33**, 1247–1254.
4 C. Cheng, J. Zhang, Y. Mu, J. Gao, Y. Feng, H. Liu, Z. Guo and C. Zhang, *Journal of Analytical and Applied Pyrolysis*, 2014, **108**, 41–46.
5 M. Latorre-Sánchez, A. Primo and H. García, *Angewandte Chemie International Edition*, 2013, **52**, 11813–11816.
6 D.-S. Yang, D. Bhattacharjya, S. Inamdar, J. Park and J.-S. Yu, *J. Am. Chem. Soc.*, 2012, **134**, 16127–16130.
7 Y. Zhang, T. Mori, J. Ye and M. Antonietti, *J. Am. Chem. Soc.*, 2010, **132**, 6294–6295.
8 R. Imamura, K. Matsui, J. Ozaki and A. Oya, *Carbon*, 1998, **36**, 1243–1245.
9 V. Strelko Jr, M. Streat and O. Kozynchenko, *Reactive and Functional Polymers*, 1999, **41**, 245–253.
10 S. Ronka, *Journal of Analytical and Applied Pyrolysis*, 2014, **110**, 390–400.
11 Z. Liu, F. Peng, H. Wang, H. Yu, J. Tan and L. Zhu, *Catalysis Communications*, 2011, **16**, 35–38.
12 S. Marinkovic, C. Suznjevic, A. Tukovic, I. Dezarov and C. d, *Carbon*, 1973, **11**, 217–220.
13 D. W. McKee, C. L. Spiro and E. J. Lamby, *Carbon*, 1984, **22**, 285–290.
14 R. Li, Z. Wei, X. Gou and W. Xu, *RSC Adv.*, 2013, **3**, 9978.
15 C. Huang, A. M. Puziy, T. Sun, O. I. Poddubnaya, F. Suárez-García, J. M. D. Tascón and D. Hulicova-Jurcakova, *Electrochimica Acta*, 2014, **137**, 219–227.
16 C. Huang, A. M. Puziy, O. I. Poddubnaya, D. Hulicova-Jurcakova, M. Sobiesiak and B. Gawdzik, *Electrochimica Acta*, 2018, **270**, 339–351.
17 D. Hulicova-Jurcakova, A. M. Puziy, O. I. Poddubnaya, F. Suárez-García, J. M. D. Tascón and G. Q. Lu, *J. Am. Chem. Soc.*, 2009, **131**, 5026–5027.
18 M.-J. Kim, J.-T. Yeon, K. Hong, S.-I. Lee, N.-S. Choi and S.-S. Kim, *Bulletin of the Korean Chemical Society*, 2013, **34**, 2029–2035.
19 T. D. Tran, J. H. Feikert, X. Song and K. Kinoshita, *J. Electrochem. Soc.*, 1995, **142**, 3297.
20 X. Cao, J. Wu, C. Jin, J. Tian, P. Strasser and R. Yang, *ACS Catal.*, 2015, **5**, 4890–4896.
21 Z.-W. Liu, F. Peng, H.-J. Wang, H. Yu, W.-X. Zheng and J. Yang, *Angewandte Chemie International Edition*, 2011, **50**, 3257–3261.
22 Z.-W. Liu, F. Peng, H.-J. Wang, H. Yu, W.-X. Zheng and J. Yang, *Angewandte Chemie International Edition*, 2011, **50**, 3257–3261.
23 S. Zhang, X.-Z. Yuan, J. N. C. Hin, H. Wang, K. A. Friedrich and M. Schulze, *Journal of Power Sources*, 2009, **194**, 588–600.
24 T. R. Ralph, S. Hudson and D. P. Wilkinson, *ECS Trans.*, 2006, **1**, 67.
25 L. M. Roen, C. H. Paik and T. D. Jarvi, *Electrochem. Solid-State Lett.*, 2003, **7**, A19.
26 J. Wu, X. Z. Yuan, J. J. Martin, H. Wang, J. Zhang, J. Shen, S. Wu and W. Merida, *Journal of Power Sources*, 2008, **184**, 104–119.
27 S. Cherevko, N. Kulyk and K. J. J. Mayrhofer, *Nano Energy*, 2016, **29**, 275–298.
28 R. M. Darling and J. P. Meyers, *J. Electrochem. Soc.*, 2003, **150**, A1523.
29 A. Basile, M. Hilder, F. Makhlooghiazad, C. Pozo-Gonzalo, D. R. MacFarlane, P. C. Howlett and M. Forsyth, *Advanced Energy Materials*, 2018, **8**, 1703491.
30 N. V. Plechkova and K. R. Seddon, *Chemical Society Reviews*, 2008, **37**, 123–150.
31 M. Watanabe, M. L. Thomas, S. Zhang, K. Ueno, T. Yasuda and K. Dokko, *Chem. Rev.*, 2017, **117**, 7190–7239.
32 J. Lemus, J. Palomar, F. Heras, M. A. Gilarranz and J. J. Rodriguez, *Separation and Purification Technology*, 2012, **97**, 11–19.
33 J. Lemus, C. M. S. S. Neves, C. F. C. Marques, M. G. Freire, J. A. P. Coutinho and J. Palomar, *Environmental Science: Processes & Impacts*, 2013, **15**, 1752–1759.
34 S. Aparicio, M. Atilhan and F. Karadas, *Ind. Eng. Chem. Res.*, 2010, **49**, 9580–9595.

35 C. J. Bradaric, A. Downard, C. Kennedy, A. J. Robertson and Y. Zhou, *Green Chemistry*, 2003, **5**, 143–152.
36 K. Fraser and D. MacFarlane, *Australian Journal of Chemistry*, 2009, **62**, 309–321.
37 L. Zhang, X. Chen, J. Guan, Y. Jiang, T. Hou and X. Mu, *Materials Research Bulletin*, 2013, **48**, 3485–3491.
38 J. Wu, C. Jin, Z. Yang, J. Tian and R. Yang, *Carbon*, 2015, **82**, 562–571.
39 N. Ranjbar Sahraie, J. P. Paraknowitsch, C. Göbel, A. Thomas and P. Strasser, *J. Am. Chem. Soc.*, 2014, **136**, 14486–14497.
40 R. Ma, B. Y. Xia, Y. Zhou, P. Li, Y. Chen, Q. Liu and J. Wang, *Carbon*, 2016, **102**, 58–65.
41 W. Ni, S. Liu, C. Du, Y. Fei, Y. He, X. Ma, L. Lu and Y. Deng, *International Journal of Hydrogen Energy*, 2017, **42**, 19019–19027.
42 J. Gao, C. He, J. Liu, P. Ren, H. Lu, J. Feng, Z. Zou, Z. Yin, X. Wen and X. Tan, *Catalysis Science & Technology*, 2018, **8**, 1142–1150.
43 J. J. Yeh and I. Lindau, *Atomic Data and Nuclear Data Tables*, 1985, **32**, 1–155.
44 D. A. Shirley, *Phys. Rev. B*, 1972, **5**, 4709–4714.
45 T. Kanagawa, R. Hobara, I. Matsuda, T. Tanikawa, A. Natori and S. Hasegawa, *Physical review letters*, 2003, **91**, 036805.
46 H. Chandra, S. Allen, S. Oberloier, N. Bihari, J. Gwamuri and J. Pearce, *Materials*, **10**, 110.
47 F. J. Perez-Alonso, D. N. McCarthy, A. Nierhoff, P. Hernandez-Fernandez, C. Strebel, I. E. L. Stephens, J. H. Nielsen and I. Chorkendorff, *Angewandte Chemie International Edition*, 2012, **51**, 4641–4643.
48 M. Li, Z. Zhao, T. Cheng, A. Fortunelli, C.-Y. Chen, R. Yu, Q. Zhang, L. Gu, B. V. Merinov, Z. Lin, E. Zhu, T. Yu, Q. Jia, J. Guo, L. Zhang, W. A. Goddard, Y. Huang and X. Duan, *Science*, 2016, **354**, 1414–1419.
49 M. E. Baumgärtner and D. R. Gabe, *Transactions of the IMF*, 2000, **78**, 11–16.
50 M. E. Baumgärtner and D. R. Gabe, *Transactions of the IMF*, 2000, **78**, 79–85.
51 A. Egetenmeyer, I. Radev, D. Durneata, M. Baumgärtner, V. Peinecke, H. Natter and R. Hempelmann, *International Journal of Hydrogen Energy*, 2017, **42**, 13649–13660.
52 A. Egetenmeyer, M. Baumgärtner, T. Linckh, D. Durneata, H. Natter, R. Hempelmann, I. Radev and V. Peinecke, *Transactions of the IMF*, 2017, **95**, 9–19.
53 F. Müller, S. Grandthyll, C. Zeitz, K. Jacobs, S. Hüfner, S. Gsell and M. Schreck, *Phys. Rev. B*, 2011, **84**, 075472.
54 J. F. Moulder, W. F. Stickle, P. E. Sobol and K. D. Bomben, *Handbook of X-Ray Photoelectron Spectroscopy*, Perkin-Elmer Corporation, Eden Prairie, Minnisota, 1993.
55 S. K. Zecevic, J. S. Wainright, M. H. Litt, S. L. Gojkovic and R. F. Savinell, *J. Electrochem. Soc.*, 1997, **144**, 2973.
56 R. M. Q. Mello and E. A. Ticianelli, *Electrochimica Acta*, 1997, **42**, 1031–1039.
57 R. Li, Z. Wei, X. Gou and W. Xu, *RSC Adv.*, 2013, **3**, 9978–9984.
58 K. Yoshii, K. Yamaji, T. Tsuda, K. Tsunashima, H. Yoshida, M. Ozaki and S. Kuwabata, *J. Phys. Chem. B*, 2013, **117**, 15051–15059.
59 Y. Cao and T. Mu, *Ind. Eng. Chem. Res.*, 2014, **53**, 8651–8664.
60 A. F. Ferreira, P. N. Simões and A. G. M. Ferreira, *The Journal of Chemical Thermodynamics*, 2012, **45**, 16–27.
61 M. Kosmulski, J. Gustafsson and J. B. Rosenholm, *Thermochimica Acta*, 2004, **412**, 47–53.
62 S. Zhang, J. Zhang, Y. Zhang and Y. Deng, *Chem. Rev.*, 2017, **117**, 6755–6833.
63 P. Sippel, P. Lunkenheimer, S. Krohns, E. Thoms and A. Loidl, *Scientific Reports*, 2015, **5**, 13922.
64 H. Wang, Q. Lu, C. Ye, W. Liu and Z. Cui, *Wear*, 2004, **256**, 44–48.
65 A. E. Jiménez and M.-D. Bermúdez, *Tribol Lett*, 2009, **33**, 111–126.
66 Z. Li, A. Dolocan, O. Morales-Collazo, J. T. Sadowski, H. Celio, R. Chrostowski, J. F. Brennecke and F. Mangolini, *Advanced Materials Interfaces*, 2020, **7**, 2000426.
67 R. Sheldon, *Chemical Communications*, 2001, **0**, 2399–2407.
68 X. Sun, H. Luo and S. Dai, *Chem. Rev.*, 2012, **112**, 2100–2128.

69 M. Forsyth, L. Porcarelli, X. Wang, N. Goujon and D. Mecerreyes, *Acc. Chem. Res.*, 2019, **52**, 686–694.
70 F. Philippi, D. Rauber, J. Zapp and R. Hempelmann, *Phys. Chem. Chem. Phys.*, 2017, **19**, 23015–23023.
71 C. Schreiner, S. Zugmann, R. Hartl and H. J. Gores, *J. Chem. Eng. Data*, 2010, **55**, 1784–1788.
72 M. D. Green, C. Schreiner and T. E. Long, *J. Phys. Chem. A*, 2011, **115**, 13829–13835.
73 K. R. Harris and M. Kanakubo, *J. Chem. Eng. Data*, 2016, **61**, 2399–2411.
74 K. Ueno, H. Tokuda and M. Watanabe, *Physical Chemistry Chemical Physics*, 2010, **12**, 1649–1658.
75 D. R. MacFarlane, M. Forsyth, E. I. Izgorodina, A. P. Abbott, G. Annat and K. Fraser, *Physical Chemistry Chemical Physics*, 2009, **11**, 4962–4967.
76 S. Mondal, T. Mandal, M. Sharma, R. Kumar, A. K. Arora, V. Bansal, J. Christopher and G. S. Kapur, *Tetrahedron Letters*, 2017, **58**, 2460–2464.
77 K. R. Harris, *J. Phys. Chem. B*, 2019, **123**, 7014–7023.
78 M. Yoshizawa, W. Xu and C. A. Angell, *J. Am. Chem. Soc.*, 2003, **125**, 15411–15419.
79 H. G. Becker, W. Berger and G. Domschke, *Organikum - Organisch-chemisches Grundpraktikum*, Wiley-VCH, Weinheim, 22. Auflage., 2004.
80 G. Tammann and W. Hesse, *Zeitschrift für anorganische und allgemeine Chemie*, 1926, **156**, 245–257.
81 H. VOGEL, *Phys. Z.*, 1921, **22**, 645–646.
82 K. R. Harris, M. Kanakubo, D. Kodama, T. Makino, Y. Mizuguchi, M. Watanabe and T. Watanabe, *J. Chem. Eng. Data*, 2018, **63**, 2015–2027.
83 K. R. Harris and M. Kanakubo, *J. Phys. Chem. B*, 2016, **120**, 12937–12949.
84 B. A. Khaskin, N. N. Tuturina and N. N. Mel'nikov, *Zhurnal Obshchei Khimii*, 1967, **37**, 2757–2760.
85 H. Tokuda, K. Hayamizu, K. Ishii, Md. A. B. H. Susan and M. Watanabe, *J. Phys. Chem. B*, 2004, **108**, 16593–16600.
86 G. H. Sørland, *Dynamic Pulsed-Field-Gradient NMR*, Springer Berlin Heidelberg, Berlin, Heidelberg, 2014, vol. 110.
87 C. S. Johnson, *Progress in Nuclear Magnetic Resonance Spectroscopy*, 1999, **34**, 203–256.
88 E. O. Stejskal and J. E. Tanner, *J. Chem. Phys.*, 1965, **42**, 288–292.